ABSTRACT

PLANE WAVE INCIDENCE TO A CYLINDRICAL FREQUENCY SELECTIVE SURFACE COMPRISING OF METAL STRIPS

UZER, Ali

PhD. in Electrical and Electronics Engineering Department

Supervisor: Prof. Dr. Tuncay EGE

May 2005, 128 pages

Scatterings from circular cylindrical structures comprising of free-standing or dielectric shell backed metal strips are considered. When formulating the problem, the scattered waves are written as infinite sums of cylindrical Floquet modes with unknown weighting coefficients. The weighting coefficients are then determined by using boundary conditions appropriate for the problem. Numerical results are obtained by applying the Moment method (MM) techniques whereby entire domain sinusoidal basis functions are used. The infinite sums appearing in MM solutions are found to be slowly convergent. When solving the problem by a MM technique, the infinite sums should be handled properly in order to circumvent slow convergence difficulties. One approach in such a case is to use sub-domain basis functions in conjunction with a conjugate gradient fast Fourier transform method. Another approach is to use entire-domain basis functions together with a convergence acceleration method. Here, we follow the second approach and give an appropriate convergence acceleration method. It is shown that the resulting infinite sums of the MM solutions can be very efficiently computed by employing a new convergence acceleration technique based on Kummer's method.

Results reveal that the thickness of the dielectric shell strongly affects the scattering properties of conducting strips. Moreover, resonances are detected at some specific frequencies where the structure becomes almost invisible to an observer. Such properties of cylindrical structures may be very useful in radar applications or antenna applications.

Keywords: Cylindrical Frequency Selective Surface, Cylindrical Structures, Cylindrical Floquet Modes, Convergence Acceleration, Kummer’s Method, Scattering, Radar Cross Section.

ÖZ

DÜZLEMSEL DALGANIN METAL ŞERİTLERDEN OLUŞMUŞ BİR SİLİNDİRİK FREKANS SEÇİCİ YÜZEYDEN SAÇILIMI

UZER, Ali

Doktora Tezi,.Elektrik Elektronik Mühendisliği Bölümü

Tez Yöneticisi: Prof. Dr. Tuncay EGE

Mayıs 2005, 128 sayfa

Boşlukta duran yada dielektrik bir madde üzerine dizilmiş metal şeritlerden saçılan elektromanyetik dalgalar incelendi. Formüllerde saçılan dalgalar Floquet modlarının bilinmeyen katsayılı sonsuz toplamları cinsinden yazıldı. Daha sonra bu bilinmeyen katsayılar sınır şartları uygulanarak bulundu. Moment metot çözümlerinde baz fonksiyonları olarak tüm bölge sinüs fonksiyonları kullanıldı ve sayısal çözümler elde edildi. Moment metot matrislerinin hesaplamaları yapılırken sonsuz toplamların yavaş yakınsadığı görüldü ve yakınsama hızlarının arttırılması gerektiği anlaşıldı. Bu tür durumlarda sorunu gidermenin bir yolu baz fonksiyonları olarak alt bölge fonksiyonları kullanmaktır. Diğer bir yol ise baz fonksiyonları olarak tüm bölge fonksiyonları kullandıktan sonra sonsuz toplamların yakınsama hızlarını arttıracak bir hız arttırıcı metot kullanmaktır. Çalışmada ikinci yol seçilerek uygun bir yakınsama hızlandırıcı metot geliştirildi. Kummer metoduna dayalı olan yeni hızlandırıcı metot sayesinde Moment metot çözümlerinde ortaya çıkan sonsuz toplamlar rahatça hesaplanabilmektedir.

Elde ettiğimiz sonuçlarda dielektrik katman kalınlığının metal şeritlerden elektromanyetik dala saçılma özelliklerini çok etkilediği görüldü. Ayrıca katman kalınlıklarının sebep olduğu bazı rezonans frekansları tespit edildi ki bu frekanslarda silindirik yapı neredeyse hiç saçılma yapmamaktadır. Böyle bir özellik radar yada anten uygulamalarında çok kullanışlı olabilir.

Anahtar kelimeler: Silindirik Frekans Seçici Yüzey, Silindirik Yapı, Silindirik Floquet Modları, Sonsuz Toplam Yakınsama Hızlandırıcı, Kummer Metodu, Saçılma, Radar Genişliği.

ACKNOWLEDGEMENTS

I would like to thank to my supervisor Prof. Dr. Tuncay Ege for his guidance, patience, and encouragement during my study period. His constructive criticism and comments from the initial conception to the end of this work is highly appreciated.

Also I would like to express my deepest gratitude to my family for their love, patience and forbearance.

TABLE OF CONTENTS

LIST OF FIGURES

NOMENCLATURE

List of Abbreviations

MM : Moment method
RCS : radar Cross Section
TM : transverse magnetic field mode
TE : transverse electric field mode

List of Symbols

A_{TM} : vector potential for a transverse magnetic field mode
A_{TE} : vector potential for a transverse electric field mode
B_n : Bernoulli number
$B_n(x)$: Bernoulli polynomial of the argument x
b : width of a unit cell in ϕ direction
β_n : phase variation in z direction for dielectric rod problem
c : velocity of the light in the free-space, $3 \cdot 10^8$ *m/sec*
f : frequency
j : imaginary number $\sqrt{-1}$
$J_v(z)$: Bessel function of the first kind of order v and argument z
$H_v^{(1)}(z)$: Hankel function of the first kind of order v and argument z.
$H_v^{(2)}(z)$: Hankel function of the second kind of order v and argument z.
k_0 : wave number of the free-space, $\omega\sqrt{\mu_0 \varepsilon_0}$.
κ_n : propagation constant of a Bessel function in the free space
κ_{in} : propagation constant of a Bessel function in the *i-th* region
l : length of a strip
N : number of elements in the circumferential direction
w : width of a strip
$Y_v(z)$: Bessel function of the second kind of order v and argument z
Z_0 : intrinsic impedance of the free-space, 120π
T_ϕ : periodicity of the cylindrical structure in the circumferential direction
T_z : periodicity of the cylindrical structure in the axial direction
ε_0 : permittivity of the free-space, $10^{-9}/36\pi$ Farad/meter
ε_r : relative permittivity of a dielectric material
ψ_{mn} : Floquet mode
λ : wavelength in the free-space
μ_0 : permeability of the free-space, $4\pi 10^{-7}$ *H*/*m*
ρ : radial variable of the cylindrical coordinate system
$\zeta(s)$: zeta function of the argument s
$\cong$: asymptotically equal to

1. INTRODUCTION

Measurements demonstrate that periodic surfaces have band-pass and band-stop characteristics when illuminated by an incident electromagnetic wave of variable frequency. There are many important structures whose characteristics are periodic in space. Examples are three-dimensional lattice structures for crystals, artificial dielectrics consisting of periodically placed conducting pieces, and waveguides with periodic loadings. The waves along these structures exhibit a unique frequency dependence often characterized as stop-bands and pass-bands [1, 2].

Basically a Frequency Selective Surface may be of two types, either in the form of periodically perforated screens (apertures), or in the form of an array of conducting patches printed on a dielectric substrate. At a specific frequency, the surface exhibits a total transmission for the screen problem, or a total reflection for the dual case. Such specific frequencies are called as “resonant frequencies”. Resonant frequencies depend on the shape of the elements (patches/slots).

1.1. Typical Applications of Frequency Selective Surfaces

Typical applications are many and varied. They range over much of the electromagnetic spectrum. For example in the microwave region the frequency selective properties of periodic screens are exploited to make more efficient use of reflector antennas. As shown in Figure 1.1, a frequency selective surface may be placed between two feeds, which are radiating at two different frequencies. The resonant frequency of the surface is designed such that the surface becomes totally reflective over the operating band of feed 1, but becomes transparent over the operating band of feed 2. Hence with this configuration, two independent feeds may share a single reflector simultaneously [3].

A next example for the exploitation of frequency selective properties of periodic screens in the microwave region is the applications in radome designs. The main function of a radome is to protect an antenna from environmental conditions such as rain and snow. Although a radome covers the antenna, it must be transparent at the antenna's operation frequencies. The screens of the radome are designed such that it gives band-pass transmission characteristics at the operating frequencies of the antenna. At the out-of-band frequencies, the radome becomes totally reflecting [2].

In the far-infrared region, periodic screens are used as polarizes, beam splitters, as well as mirrors for improving the pumping efficiency in molecular lasers [2]. A polarizer can be constructed from a diffraction grating such that the fields polarized parallel to the grating are reflected, while those with orthogonal polarizations are transmitted.

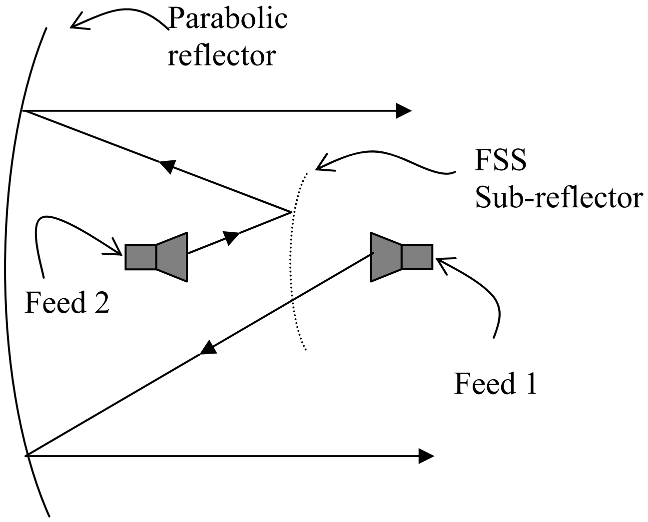

Figure 1.1. An application of frequency selective surfaces. Two feeding antennas are placed at front and back focus of the sub-reflector.

Another application in the far-infrared region is infrared sensors where the frequency selective property of a frequency selective surface is used to absorb the desired frequencies in the substrate material backing the screen, while rejecting the out-of-band frequencies [2]. In the near-infrared and visible portions of the electromagnetic spectrum, periodic screens are proposed as solar selective surfaces to aid in the collection of solar energy. A screen is designed such that it is essentially transparent in the frequency band where the solar cells are most efficient and is reflecting at frequencies out of this band [2].

1.2. Previous Works for Planar Frequency Selective Surfaces

In 1961, a problem of scattering from a conducting screen perforated periodically with apertures is analyzed by Keiburt and Ishimaru [4]. Later on, the scattering from two-dimensional periodic array of rectangular plates is investigated by Ott, Kouyoumjian, and Peters [5]. The given solution is restricted to the case of narrow width plates arranged in a rectangular lattice and the incident field is assumed to be a normally incident plane wave. In 1970, a general formulation technique for two-dimensional periodic arrays is presented by C. C. Chen [6]. The field distributions are expanded into a set of Floquet Mode functions, and an integral equation is obtained. Then the equation is solved for the unknown induced currents by using a Moment Method (MM).

In 1975, J. P. Montgomery [7] give solutions to unsymmetrical problems of scattering of plane waves by the infinite periodic arrays of thin conductors. Later on, Tsao and Mittra [8] in 1982 present an iterative procedure in spectral domain to solve simultaneously for the current distribution and the aperture field of a frequency selective surface. They derive a differential equation, based on the Floquet Mode expansion and the electromagnetic boundary conditions. They also presented a full wave analysis of both the cross shaped and Jerusalem type elements.

1.3. Previous Works for Cylindrical Frequency Selective Surfaces

In [9] Floquet Theorem is applied to a cylindrical phased array antenna problem consisting of periodically arranged axial dipoles, which are excited by a matching network at their centers. The far fields radiated from a dipole are determined by employing cylindrical Floquet modes. Later on, Tom Cwik [10] considers circular cylindrical structures covered periodically with metallic patches. He presents formulations in terms of the cylindrical Floquet modes for calculating the induced currents on the surfaces of free-standing strips. The numerical results are given for infinitely long strips. References [11, 12] analyze dispersion characteristics of circular waveguides made up of free-standing conducting strips or patches. In [13, 14] plane wave scattering from square patches is considered. When obtaining the numerical the MM solutions, the references [10-14] use sub-domain basis functions and a conjugate gradient fast Fourier transform method in order to circumvent the slow convergence difficulties of infinite sums.

A. Freni [15] considers scattering of plane waves from circular cylinders loaded periodically with groups of metallic rings along the longitudinal axes. Also, Ahmed A. Kishk and Per-Simon Kildal [16] describe asymptotic boundary conditions that are intended to be used to model grids of metal strips. But as stated by them, their methods are restricted because the given boundary conditions lose accuracy if the period of the grid is not small in terms of the wavelength.

The reference [17] analyzes a cylindrical wave incidence to a cylindrical frequency selective surface comprising of metal strips and determine the reflection and transmission coefficients of the problem. The results show that the reflection and transmission coefficients are dependent on the problem geometry as in the planar frequency selective surfaces. The MM solutions of periodic cylindrical structures generally yield slowly convergent infinite sums. In [18], a convergence acceleration technique is given for the MM solutions of periodic cylindrical structures. In [19] the radiated far fields due to a current filament located inside a periodic cylindrical structure are determined. Later on, [20] computes the radar cross sections (RCS) of conducting circular cylinders perforated periodically with axial slots. More recently, the convergence acceleration method in [18] is further improved and generalized [21].

1.4. The Methods Utilized in this Study

A periodic excitation to a linear system produces a response that is also periodic. As a consequence of this, Floquet theorem recognizes that the responses may be represented by an infinite sum of periodic functions, which are called as Floquet modes [10]. In Chapter 2, Floquet theorem will be described and the relevant modes for periodic cylindrical structures are derived.

Periodic cylindrical structures comprising of free-standing conducting patches are considered in the first part of Chapter 3. The scattered waves of the problem are expressed in terms of the surface currents by using the Floquet Theorem. The currents are then determined from the exciting wave and from the boundary conditions of the problem. Also, the dual problem where the conducting circular cylinders perforated periodically with axial slots is analyzed similarly in the second part of Chapter 3. In the second problem, the Equivalence Principle is utilized to replace slot fields with equivalent magnetic currents. Later on, boundary conditions relevant to the problem are used to determine the scattered waves in terms of the exciting wave. The numerical results in all problems are obtained by applying the MM solution techniques. In MM solutions, the surface currents or the slot fields of the problems mentioned above are expanded into entire domain sinusoidal basis functions. A convergence acceleration method is given for efficient and accurate computations of the infinite sums in MM solutions. In appendices A and B, the acceleration method is explained in detail.

In Chapter 4, dielectric shell structures covered periodically with conducting strips are analyzed. Problem is formulated by writing the scattered waves as infinite sums of the Floquet modes. The scattered waves involve transverse magnetic (TM) and transverse electric (TE) modes simultaneously. The unknown surface currents of the problem are related to the incident wave and the resulting equations are solved by MM techniques. It is important to note that the convergence acceleration methods of Chapter 3 become applicable if a Kummer's acceleration method is exploited in the MM solution. This point is fully described in appendix C.

The numerical results for all of the problems considered in this thesis are given in Chapter 5. RCS and the field couplings into the cylindrical structures are computed against the problem parameters such as the strip/slot lengths, the number of strips/slots, the dielectric shell thicknesses, etc. Also our results are compared with those available in the literature [10].

2. FLOQUET THEOREM FOR PERIODIC CYLINDRICAL STRUCTURES

In this chapter we concentrate on cylindrical wave solutions of periodic cylindrical structures. When solving a periodic problem in the cylindrical coordinate system, scattered fields are written as infinite sums of cylindrical waves, which are called as cylindrical Floquet modes. Starting from the Helmhotz wave equation, the Floquet modes are derived for a cylindrical wave excitation case in the following section. If the incident wave is not cylindrical –as is a plane wave- it can be represented by cylindrical waves as described in Section 2.2. Also in Section 2.3, the cylindrical waves radiated from a line current located at the origin are given.

2.1. Derivation of the Floquet modes

Consider a periodic cylindrical structure as shown in Figure 2.1, which may consist of periodically located elements. The periodicities of the structure are denoted by T_ϕ and T_z in ϕ and z directions, respectively. If the structure is excited by a cylindrical wave, it can be shown that the scattered waves should also be periodic. Hence, the scattered waves may be represented as infinite sums of periodic functions, which are known as the cylindrical Floquet modes [10]. To obtain the cylindrical Floquet modes, we start with a scalar Helmhotz wave equation in a source free region

$$(\nabla^2 + k^2)A_p(\rho,\phi,z) = 0\,, \tag{2.1}$$

where A_p, denotes a vector potential and p indicates its polarization (the polarization may be transverse magnetic (TM) or transverse electric (TE)). Here k denotes the wave number of the medium, $k = \omega\sqrt{\mu\varepsilon}$. Assume the structure is excited by a cylindrical wave, which has a phase factor $e^{-j\nu_0\phi}e^{-j\beta_0 z}$. Since the scattered waves should be periodic in the cylindrical coordinate variables ϕ and z, the solutions to the wave equation should satisfy the periodicity requirements:

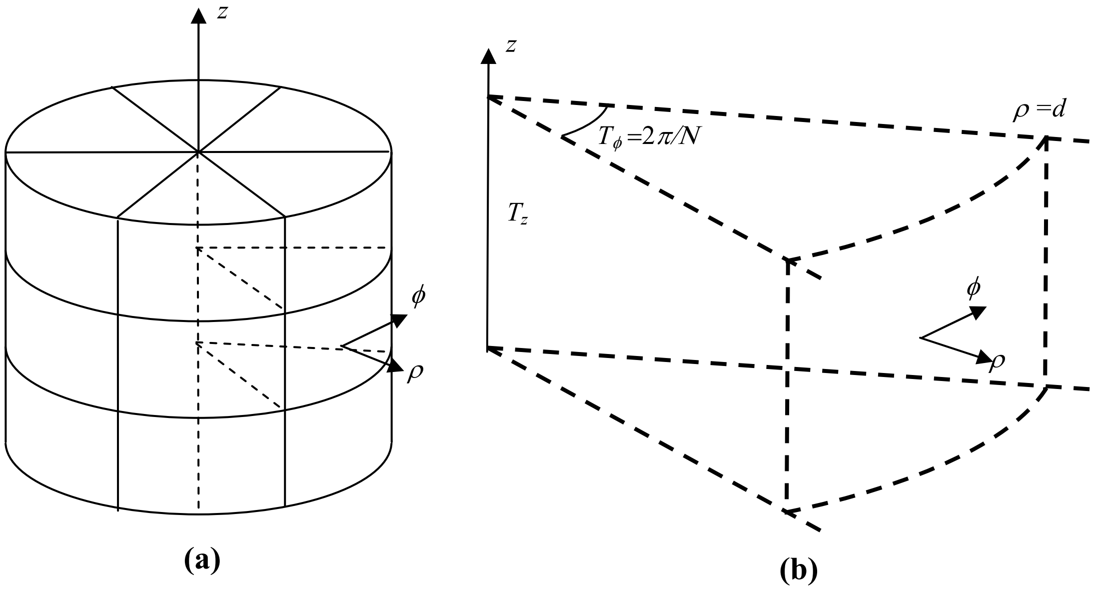

Figure 2.1. (a) A cylindrical structure with two-dimensional periodicity. **(b)** A unit cell of the problem at ϕ=0. N denotes the number of periodic cells in ϕ direction.

$$A_p(\rho,\phi,z+T_z)=A_p(\rho,\phi,z)e^{-j\beta_0 T_z}\,, \tag{2.2}$$

$$A_p(\rho,\phi+T_\phi,z)=A_p(\rho,\phi,z)e^{-j\nu_0 T_\phi}\,. \tag{2.3}$$

In the cylindrical coordinate system, the wave equation in (2.1) is expressed as in [22]

$$\left(\frac{\partial^2}{\partial\rho^2}+\frac{1}{\rho}\frac{\partial}{\partial\rho}+\frac{1}{\rho^2}\frac{\partial^2}{\partial\phi^2}+\frac{\partial^2}{\partial z^2}+k^2\right)A_p(\rho,\phi,z)=0\,. \tag{2.4}$$

This partial differential equation can be solved by the separation of variables method. For this, let us write the vector potential as a product of three functions

$$A_p(\rho,\phi,z)=R(\rho)\Phi(\phi)Z(z)\,. \tag{2.5}$$

Substituting this into (2.4) and dividing the resultant equation by $R(\rho)\Phi(\phi)Z(z)$, we get

$$\frac{1}{R(\rho)}\left(\frac{\partial^2 R(\rho)}{\partial\rho^2}+\frac{\partial R(\rho)}{\rho\partial\rho}\right)+\frac{1}{\rho^2}\frac{1}{\Phi(\phi)}\frac{\partial^2\Phi(\phi)}{\partial\phi^2}+\frac{1}{Z(z)}\frac{\partial^2 Z(z)}{\partial z^2}+k^2=0\,. \tag{2.6}$$

That yields three ordinary differential equations

$$\frac{1}{Z(z)}\frac{d^2 Z(z)}{dz^2} = -\beta^2, \tag{2.7}$$

$$\frac{1}{\Phi(\phi)}\frac{d^2 \Phi(\phi)}{d\phi^2} = -v^2, \tag{2.8}$$

and

$$\rho^2\frac{d^2 R(\rho)}{d\rho^2} + \rho\frac{dR(\rho)}{d\rho} + \left(\kappa^2\rho^2 - v^2\right)R(\rho) = 0. \tag{2.9}$$

Here κ is given by the dispersion relation

$$\kappa^2 = k^2 - \beta^2, \tag{2.10}$$

and the eigenvalues v and β denote real numbers. A general solution to (2.7) is written as

$$Z(z) = C_p^- e^{j\beta z} + C_p^+ e^{-j\beta z}. \tag{2.11}$$

Applying the condition (2.2), the eigenvalues β are determined as follows:

$$C_p^- e^{j\beta(z+T_z)} + C_p^+ e^{-j\beta(z+T_z)} = \left(C_p^- e^{j\beta z} + C_p^+ e^{-j\beta z}\right)e^{-j\beta_0 T_z},$$

$$C_p^- e^{j2\beta z}\left(e^{j(\beta_0+\beta)T_z} - 1\right) = C_p^+\left(1 - e^{j(\beta_0-\beta)T_z}\right). \tag{2.12}$$

(2.12) is satisfied only if

$$C_p^- e^{j2\beta z}\left(e^{j(\beta_0+\beta)T_z} - 1\right) = C_p^+\left(1 - e^{j(\beta_0-\beta)T_z}\right) = 0. \tag{2.13}$$

When $C_p^+ = C_p^-$, a trivial solution is obtained but that has no significance. There are two possibilities for satisfying the conditions in (2.13): either $C_p^- = 0$ and $e^{j(\beta_0-\beta)T_z} = 1$, or $e^{j(\beta_0+\beta)T_z} = 1$ and $C_p^+ = 0$. A solution satisfying the conditions in (2.13) is

$$\beta_n = \beta_0 + 2\pi n / T_z \,;\, n = 0, \pm 1, \pm 2, \ldots \tag{2.14}$$

and thus

$$Z_n(z) = \frac{e^{-j\beta_n z}}{\sqrt{T_z}}, \tag{2.15}$$

where β_n and Z_n denote eigenvalues and normalized eigenfunctions, respectively. Similarly, using the condition (2.3), the eigenvalues v and the corresponding eigenfunctions are obtained as

$$v_m = v_0 + 2\pi m / T_\phi \,;\, m = 0, \pm 1, \pm 2, \ldots, \tag{2.16}$$

$$\Phi_m(\phi) = \frac{e^{-jv_m\phi}}{\sqrt{T_\phi}}. \tag{2.17}$$

In that case, the equation (2.9) becomes

$$\rho^2 \frac{d^2 R_{mn}(\rho)}{d\rho^2} + \rho \frac{dR_{mn}(\rho)}{d\rho} + \left(\kappa_n^2 \rho^2 - v_m^2\right) R_{mn}(\rho) = 0. \tag{2.18}$$

This form of equations is known as Bessel's differential equations [22]. A general solution to (2.18) can be written in terms of the Hankel functions of the first kind $H^{(1)}$ and the second kind $H^{(2)}$:

$$R_{mn}(\rho) = A^-_{p,mn} H^{(1)}_{v_m}(\kappa_n \rho) + A^+_{p,mn} H^{(2)}_{v_m}(\kappa_n \rho). \tag{2.19}$$

Here Hankel functions represent cylindrical traveling waves, as do the exponential functions, $H^{(1)}$ representing an inward-traveling wave and $H^{(2)}$ representing an outward-traveling wave. Alternatively, it is sometimes more convenient to express the general solution of (2.18) in a form

$$R_{mn}(\rho) = a_{p,mn} J_{v_m}(\kappa_n \rho) + b_{p,mn} Y_{v_m}(\kappa_n \rho), \tag{2.20}$$

where J and Y denote Bessel functions of the first kind and the second kind, respectively. As emphasized in Appendix C, these functions exhibit oscillatory behavior, as do the sinusoidal functions and so (2.20) can be used for the standing wave solutions. Their relations to the Hankel functions are

$$H^{(1)}_{v_m}(\kappa_n \rho) = J_{v_m}(\kappa_n \rho) + jY_{v_m}(\kappa_n \rho), \tag{2.21}$$

$$H^{(2)}_{v_m}(\kappa_n \rho) = J_{v_m}(\kappa_n \rho) - jY_{v_m}(\kappa_n \rho). \tag{2.22}$$

Hence the solution for A_p can be written as infinite sums of the traveling waves:

$$A_p(\rho,\phi,z) = \sum_{m=-\infty}^{\infty}\sum_{n=-\infty}^{\infty}\left\{A^{-}_{p,mn}H^{(1)}_{v_m}(\kappa_n\rho) + A^{+}_{p,mn}H^{(2)}_{v_m}(\kappa_n\rho)\right\}\psi_{mn}(\phi,z)\,, \tag{2.23}$$

or whenever appropriate it may be written in terms of the standing waves:

$$A_p(\rho,\phi,z) = \sum_{m=-\infty}^{\infty}\sum_{n=-\infty}^{\infty}\left\{a_{p,mn}J_{v_m}(\kappa_n\rho) + b_{p,mn}Y_{v_m}(\kappa_n\rho)\right\}\psi_{mn}(\phi,z)\,. \tag{2.24}$$

Here ψ_{mn} are called as the Floquet modes, which involve the products of the eigenfunctions $\Phi_m(\phi)$ and $Z_n(z)$

$$\psi_{mn}(\phi,z) = \frac{e^{-jv_m\phi}e^{-j\beta_n z}}{\sqrt{T_\phi T_z}}\,. \tag{2.25}$$

The propagation constants of the Floquet modes are given by

$$v_m = v_0 + 2\pi m/T_\phi\ , \tag{2.26}$$

$$\beta_n = \beta_0 + 2\pi n/T_z\ , \tag{2.27}$$

$$\kappa_n = \sqrt{k^2 - \beta_n^2}\,. \tag{2.28}$$

The roots for the double valued square-root function, "$\sqrt{\ }$", in (2.28) should be chosen properly with the conventions described in [22], that is

$$\kappa_n = \begin{cases} \sqrt{k^2 - \beta_n^2} & \text{when} \quad k^2 > \beta_n^2 \\ -j\sqrt{\beta_n^2 - k^2} & \text{when} \quad \beta_n^2 > k^2 \end{cases}. \tag{2.29}$$

If the region under the consideration is lossy, the root choice should be such that

$$\kappa_n = \kappa'_n - j\kappa''_n\,, \tag{2.30}$$

where κ'_n and κ''_n represent non-negative real numbers. Whenever the argument of a Bessel function takes an imaginary value ($\kappa_n\rho = -j\alpha$) as may come across in using (2.29), it is appropriate to use the modified Bessel functions. The modified Bessel functions are related to the regular Bessel functions through

$$J_{v_m}(-j\alpha) = e^{-jv_m\pi/2}I_{v_m}(\alpha)\,, \tag{2.31}$$

$$Y_{v_m}(-j\alpha) = -je^{-jv_m\pi/2} I_{v_m}(\alpha) - \frac{2}{\pi} e^{jv_m\pi/2} K_{v_m}(\alpha), \tag{2.32}$$

and

$$H_{v_m}^{(2)}(-j\alpha) = J_{v_m}(-j\alpha) - jY_{v_m}(-j\alpha) = \frac{2j}{\pi} e^{jv_m\pi/2} K_{v_m}(\alpha), \tag{2.33}$$

where I_{v_m} are known as the modified Bessel functions of the first kind and K_{v_m} are known as the modified Bessel functions of the second kind.

The weighting coefficients $A_{p,mn}^-$ and $A_{p,mn}^+$ in (2.23) or $a_{p,mn}$ and $b_{p,mn}$ in the alternative expression (2.24) should be determined from the boundary conditions in the radial direction. When the outermost region of the cylindrical structure in Figure 2.1.b is considered, the expression (2.23) should be utilized because the waves travel in the radial direction. Furthermore, inward-traveling waves should not exist and that leads to $A_{p,mn}^- = 0$. However, when the innermost region of the cylindrical structure is considered, the expression (2.24) should be exploited because the standing waves are expected in that region. Also the wave amplitudes should be finite at ρ=0. Among the solutions of Bessel's differential equation, only $J_{v_m}(\kappa_n \rho)$ are nonsingular at ρ=0 as shown in Appendix C. Thus the boundary condition in that region requires $b_{p,mn} = 0$.

Once the vector potential of the problem is written in terms of the Floquet modes, the corresponding electric and magnetic fields can be determined from the curl equations written in the cylindrical coordinate system [23]

$$\mathbf{E} = \frac{1}{j\omega\varepsilon} \nabla \times \nabla \times \mathbf{a}_z A_{TM} - \nabla \times \mathbf{a}_z A_{TE}, \tag{2.34}$$

$$\mathbf{H} = \nabla \times \mathbf{a}_z A_{TM} - \frac{1}{j\omega\mu} \nabla \times \nabla \times \mathbf{a}_z A_{TE}. \tag{2.35}$$

which result in the electric and magnetic field expressions

$$E_\phi = \frac{1}{j\omega\varepsilon\rho} \frac{\partial^2 A_{TM}}{\partial\phi\partial z} + \frac{\partial A_{TE}}{\partial\rho}, \tag{2.36}$$

$$E_z = \frac{1}{j\omega\varepsilon}\left(\frac{\partial^2}{\partial z^2} + k^2\right)A_{TM}, \tag{2.37}$$

$$H_\phi = -\frac{\partial A_{TM}}{\partial \rho} + \frac{1}{j\omega\mu\rho}\frac{\partial^2 A_{TE}}{\partial\phi\partial z}, \tag{2.38}$$

$$H_z = \frac{1}{j\omega\mu}\left(\frac{\partial^2}{\partial z^2} + k^2\right)A_{TE}. \tag{2.39}$$

Here, no attention is paid to ρ components of the electric and magnetic fields since they are normal to the surface.

TM and TE vector potentials in a region are expressed as infinite sums of the Floquet modes

$$A_{TM} = \sum_m \sum_n a_{TM,mn} R_{mn}(\kappa_n \rho)\psi_{mn}(\phi, z), \tag{2.40}$$

$$A_{TE} = \sum_m \sum_n a_{TE,mn} R_{mn}(\kappa_n \rho)\psi_{mn}(\phi, z), \tag{2.41}$$

where *R* may be any of the Bessel functions $H_{\nu_m}^{(1)}$, $H_{\nu_m}^{(2)}$, J_{ν_m}, or Y_{ν_m}. The partial differentiations with respect to ρ, ϕ, and *z* in (2.36)-(2.39) simplify to the algebraic expressions. That is

$$\frac{\partial}{\partial\phi}\left\{\sum_m \sum_n a_{p,mn} R_{mn}(\kappa_n \rho)\psi_{mn}(\phi, z)\right\} = \sum_m \sum_n - j\nu_m a_{p,mn} R_{mn}(\kappa_n \rho)\psi_{mn}(\phi, z), \tag{2.42}$$

$$\frac{\partial}{\partial z}\left\{\sum_m \sum_n a_{p,mn} R_{mn}(\kappa_n \rho)\psi_{mn}(\phi, z)\right\} = \sum_m \sum_n - j\beta_n a_{p,mn} R_{mn}(\kappa_n \rho)\psi_{mn}(\phi, z), \tag{2.43}$$

$$\frac{\partial}{\partial\rho}\left\{\sum_m \sum_n a_{p,mn} R_{mn}(\kappa_n \rho)\psi_{mn}(\phi, z)\right\} = \sum_m \sum_n \kappa_n a_{p,mn} R'_{mn}(\kappa_n \rho)\psi_{mn}(\phi, z). \tag{2.44}$$

Then the corresponding electric and magnetic fields can be written as

$$E_\phi = \frac{-1}{j\omega\varepsilon\rho}\sum_m \sum_n a_{TM,mn}\nu_m \beta_n R_{mn}(\kappa_n \rho)\psi_{mn}(\phi, z) + \sum_m \sum_n a_{TE,mn}\kappa_n R'_{mn}(\kappa_n \rho)\psi_{mn}(\phi, z), \tag{2.45}$$

$$E_z = \frac{1}{j\omega\varepsilon}\sum_m\sum_n a_{TM,mn}\kappa_n^2 R_{mn}(\kappa_n\rho)\psi_{mn}(\phi,z)\,, \tag{2.46}$$

$$H_\phi = -\sum_m\sum_n a_{TM,mn}\kappa_n R'_{mn}(\kappa_n\rho)\psi_{mn}(\phi,z) - \frac{1}{j\omega\mu\rho}\sum_m\sum_n a_{TE,mn}v_m\beta_n R_{mn}(\kappa_n\rho)\psi_{mn}(\phi,z)\,, \tag{2.47}$$

$$H_z = \frac{1}{j\omega\mu}\sum_m\sum_n a_{TE,mn}\kappa_n^2 R_{mn}(\kappa_n\rho)\psi_{mn}(\phi,z)\,. \tag{2.48}$$

Here a prime (') means a differentiation with respect to the whole argument of a Bessel function, that is: $R'_{mn}(\kappa_n\rho) \equiv \partial R_{mn} / \partial(\kappa_n\rho)$. Once the vector potential in a region is specified and written as infinite sums of the Floquet modes, the expressions given in (2.45)-(2.48) can be used to obtain the corresponding electric and magnetic fields in that region. Later, boundary conditions can be applied to determine unknown coefficients of the infinite sums. This procedure is followed in the subsequent chapters.

In the MM solutions, a suitable inner product has to be defined. In this thesis the following inner product is used as defined in [10]

$$< f(\phi,z), g(\phi,z) >= \int_{-T_z/2}^{T_z/2}\int_{-T_\phi/2}^{T_\phi/2} f(\phi,z)g^*(\phi,z)d\phi dz\,, \tag{2.49}$$

where (*) denotes a complex conjugate. It may easily be shown that the Floquet modes $\psi_{mn}(\phi,z)$ are orthogonal to each other, that is,

$$< \psi_{mn}(\phi,z), \psi_{pq}(\phi,z) >= \begin{cases} 1 & \text{for } p = m \text{ and } q = n \\ 0 & \text{otherwise} \end{cases}\,. \tag{2.50}$$

2.2. Decomposition of a plane wave into cylindrical waves

If plane wave incidence is assumed, the incident wave should be decomposed into cylindrical wave components. Then the responses (scattered waves) of the problem should be determined separately for each of the cylindrical wave components. The total response can then be obtained by summing the individual responses [10].

In this section a plane wave propagating in free-space in a direction $(\theta^{inc},\phi^{inc})$ is considered. If the incident plane wave has a unit amplitude vector potential, its vector potential can be written as

$$A_p(x,y,z) = e^{jk_0(\sin\theta^{inc}\cos\phi^{inc}x+\sin\theta^{inc}\sin\phi^{inc}y-\cos\theta^{inc}z)}, \tag{2.51}$$

where p denotes the polarization of the plane wave (may be TM or TE). It is convenient to transform the rectangular variables x, y, and z into the cylindrical coordinate system variables ρ, ϕ, and z by using $x=\rho\cos\phi$ and $y=\rho\sin\phi$. That gives

$$A_p(x,y,z) = e^{j\kappa_0\rho\cos(\phi-\phi^{inc})}e^{-j\beta_0 z}, \tag{2.52}$$

where

$$\beta_0 = k_0\cos\theta^{inc}, \tag{2.53}$$

$$\kappa_0 = k_0\sin\theta^{inc}. \tag{2.54}$$

Then a useful identity given in [23] may be utilized, which is

$$e^{j\kappa_0\rho\cos(\phi-\phi^{inc})} = \sum_{v_0=-\infty}^{\infty} e^{jv_0(\pi/2+\phi^{inc}-\phi)}J_{v_0}(\kappa_0\rho), \tag{2.55}$$

where J_{v_0} denotes the Bessel function of the first kind of order v_0. By using the identity, the incident wave is decomposed into the cylindrical waves of the form

$$A_p(x,y,z) = \sum_{v_0=-\infty}^{\infty} A_p^{inc}(\rho,\phi,z), \tag{2.56}$$

where the cylindrical wave components are

$$A_p^{inc}(\rho,\phi,z) = e^{jv_0(\phi^{inc}-\pi/2)}J_{v_0}(\kappa_0\rho)e^{-jv_0\phi}e^{-j\beta_0 z}. \tag{2.57}$$

The corresponding electric and magnetic fields can be obtained using (2.57) in (2.45)-(2.48). For a TM incidence case, the electric and magnetic fields are given as,

$$E_\phi^{inc} = \frac{-1}{j\omega\varepsilon_0\rho}a_{TM}^{inc}v_0\beta_0 J_{v_0}(\kappa_0\rho)e^{-jv_0\phi}e^{-j\beta_0 z}, \tag{2.58}$$

$$E_z^{inc} = \frac{1}{j\omega\varepsilon_0} a_{TM}^{inc} \kappa_0^2 J_{v_0}(\kappa_0 \rho) e^{-jv_0\phi} e^{-j\beta_0 z}, \tag{2.59}$$

$$H_\phi^{inc} = -a_{TM}^{inc} \kappa_0 J'_{v_0}(\kappa_0 \rho) e^{-jv_0\phi} e^{-j\beta_0 z}, \tag{2.60}$$

$$H_z = 0, \tag{2.61}$$

where

$$a_{TM}^{inc} = e^{jv_0(\phi^{inc} - \pi/2)}. \tag{2.62}$$

For a TE incidence case, the corresponding electric and magnetic fields are

$$E_\phi^{inc} = a_{TE}^{inc} \kappa_0 J'_{v_0}(\kappa_0 \rho) e^{-jv_0\phi} e^{-j\beta_0 z}, \tag{2.63}$$

$$E_z^{inc} = 0, \tag{2.64}$$

$$H_\phi^{inc} = \frac{-1}{j\omega\mu_0 \rho} a_{TE}^{inc} v_0 \beta_0 J_{v_0}(\kappa_0 \rho) e^{-jv_0\phi} e^{-j\beta_0 z}, \tag{2.65}$$

$$H_z^{inc} = \frac{1}{j\omega\mu_0} a_{TE}^{inc} \kappa_0^2 J_{v_0}(\kappa_0 \rho) e^{-jv_0\phi} e^{-j\beta_0 z}, \tag{2.66}$$

where

$$a_{TE}^{inc} = e^{jv_0(\phi^{inc} - \pi/2)}. \tag{2.67}$$

An important parameter in scattering studies is the electromagnetic scattering by a target which is usually represented by its echo area or radar cross section (RCS). The RCS is defined as “the area intercepting the amount of power that, when scattered isotropically, produces at the receiver a density that is equal to the density scattered by the actual target” [23]. For a cylindrical structure, the RCS is also referred to as the “scattering width”. The RCS of a cylindrical structure is calculated using

$$RCS = \lim_{\rho \to \infty} 2\pi\rho \frac{\left|\mathbf{E}^s\right|^2}{\left|\mathbf{E}^i\right|^2}, \tag{2.68}$$

where $\mathbf{E}^s$ represents the scattered electric field and $\mathbf{E}^i$ represents the incident electric field. Another way of determining the RCS is to use the scattered magnetic fields

$$RCS = \lim_{\rho\to\infty} 2\pi\rho \frac{\left|\mathbf{H}^s\right|^2}{\left|\mathbf{H}^i\right|^2}. \tag{2.69}$$

The magnitudes of the terms appearing in the denominators of (2.68) and (2.69) can be determined from the vector potential given in (2.50). For a TM incidence, the corresponding electric and magnetic fields are obtained as

$$\left|\mathbf{H}^i\right| = \left|\nabla \times \mathbf{a}_z A_{TM}(x,y,z)\right| = \kappa_0 = k_0 \sin\theta^{inc}, \tag{2.70}$$

$$\left|\mathbf{E}^i\right| = 120\pi\left|\mathbf{H}^i\right| = 120\pi\kappa_0 = 120\pi k_0 \sin\theta^{inc}, \tag{2.71}$$

but for TE incidence, we have

$$\left|\mathbf{E}^i\right| = \left|-\nabla \times \mathbf{a}_z A_{TE}(x,y,z)\right| = \kappa_0 = k_0 \sin\theta^{inc}, \tag{2.72}$$

$$\left|\mathbf{H}^i\right| = \frac{\left|\mathbf{E}^i\right|}{120\pi} = \frac{\kappa_0}{120\pi} = \frac{k_0 \sin\theta^{inc}}{120\pi}, \tag{2.73}$$

where 120π stands for the intrinsic impedance of the free-space. In the subsequent chapters, the RCS of cylindrical structures are determined by using these expressions. When computing the fields scattered from a cylindrical structure in the far field region (as $\rho\to\infty$), the asymptotic forms for the Hankel functions for large arguments [24] are used. That is,

$$H_v^{(2)}(\kappa\rho) \approx \sqrt{\frac{2}{\pi\kappa\rho}} e^{j\pi/4 + jv\pi/2} e^{-j\kappa\rho} \text{ as } \rho\to\infty, \tag{2.74}$$

$$H_v'^{(2)}(\kappa\rho) \approx -j\sqrt{\frac{2}{\pi\kappa\rho}} e^{j\pi/4 + jv\pi/2} e^{-j\kappa\rho} \text{ as } \rho\to\infty. \tag{2.75}$$

2.3. The electromagnetic field couplings into the cylindrical structures

Electromagnetic field couplings into the cylindrical structures have some importance in antenna applications. The coupling is defined as the total power measured at the center of a cylindrical structure when a plane wave is incident on the structure. That is to say, the coupling is defined as

$$Coupling = \lim_{\rho \to 0} \frac{\left|\mathbf{E}^i + \mathbf{E}^s\right|^2}{\left|\mathbf{E}^i\right|^2}, \tag{2.76}$$

where $\mathbf{E}^i$ denotes the incident electric field and $\mathbf{E}^s$ denotes the scattered electric field. However, making use of the Reciprocity Theorem the coupling can be determined more easily by considering the fields radiated from a line current located at the origin [10]. According to the Reciprocity Theorem the response of a system to a source is unchanged when source and measurer are interchanged [22].

Suppose that the incident plane wave of the original problem is due to a line current (a transmitter) located at the infinity. Furthermore, let a receiver located at the origin of the cylindrical structure measures the scattered fields. According to the reciprocity theorem, the locations of the line current and the receiver can be interchanged. In that case, we evaluate the radiated fields at the infinity and normalize these with respect to the fields that would exist at the infinity if the cylindrical structure were not present. That is,

$$Coupling = \lim_{\rho \to \infty} \frac{\left|\mathbf{E}^{inc} + \mathbf{E}^s\right|^2}{\left|\mathbf{E}^{inc}\right|^2}, \tag{2.77}$$

or if the magnetic fields are used

$$Coupling = \lim_{\rho \to \infty} \frac{\left|\mathbf{H}^{inc} + \mathbf{H}^s\right|^2}{\left|\mathbf{H}^{inc}\right|^2}, \tag{2.78}$$

where $\mathbf{E}^s$ and $\mathbf{H}^s$ denote the fields in the presence of the cylindrical structure; $\mathbf{E}^{inc}$ and $\mathbf{H}^{inc}$ denote the fields in the absence of the cylindrical structure. In this section, we shall determine the fields $\mathbf{E}^{inc}$ and $\mathbf{H}^{inc}$ appearing in (2.77) and (2.78).

When a line current is located at the origin of a cylindrical structure and radiates into the free-space (in non-existence of the cylindrical structure), the radiated electric and magnetic fields can be derived from a vector potential A_{TM} or A_{TM}, depending on the type of the line current. For an electric type current, the fields are derived from a vector potential A_{TM} and for a magnetic type current, the fields are derived from a vector potential A_{TE}.

Consider an electric type line current carrying a current I_0 is located at the origin and it is represented by

$$\mathbf{I} = \mathbf{a}_z I_0 e^{-j\beta_0 z}, \tag{2.79}$$

where β_0 denotes a linear phase variation along z axis. Since the line current is directed along the z axis, the fields radiated by the line current can be obtained by letting

$$A_{TM} = a_{TM}^{inc} H_0^{(2)}(\kappa_0 \rho) e^{-j\beta_0 z}, \tag{2.80}$$

where a_0^{inc} denote an unknown to be determined, $H_0^{(2)}$ denote a Hankel function of the second kind, and

$$\kappa_0 = \sqrt{k_0^2 - \beta_0^2}, \tag{2.81}$$

denotes the propagation constant of the wave in ρ direction. The corresponding electric and magnetic fields can be derived by using (2.80) in (2.45)-(2.48)

$$E_\phi^{inc} = 0, \tag{2.82}$$

$$E_z^{inc} = \frac{1}{j\omega\varepsilon_0} a_{TM}^{inc} \kappa_0^2 H_0^{(2)}(\kappa_0 \rho) e^{-j\beta_0 z}, \tag{2.83}$$

$$H_\phi^{inc} = -a_{TM}^{inc} \kappa_0 H_0'^{(2)}(\kappa_0 \rho) e^{-j\beta_0 z}, \tag{2.84}$$

$$H_z^{inc} = 0. \tag{2.85}$$

The unknown a_0^{inc} is determined in the limit as $\rho \to 0$

$$I_0 e^{-j\beta_0 z} = \lim_{\rho \to 0} \oint_C \mathbf{H} \cdot dl = \lim_{\rho \to 0} \int_{-\pi}^{\pi} \left(\mathbf{a}_\phi H_\phi^{inc}\right) \cdot \left(\mathbf{a}_\phi \rho d\phi\right) = \lim_{\rho \to 0} \int_{-\pi}^{\pi} H_\phi^{inc} \rho d\phi. \tag{2.86}$$

Since the integration of (2.86) must be performed in the limit as $\rho \to 0$, it is convenient to represent the Hankel function by its asymptotic expansion for small arguments. By using a small argument approximation for the derivative of the Hankel function [24], the unknown a_{TM}^{inc} is determined as follows

$$
\begin{aligned}
I_0 e^{-j\beta_0 z} &= \lim_{\rho \to 0} \int_{-\pi}^{\pi} H_\phi^{inc} \rho d\phi \\
&= \lim_{\rho \to 0} \int_{-\pi}^{\pi} -a_{TM}^{inc} \kappa_0 H_0'^{(2)}(\kappa_0 \rho) e^{-j\beta_0 z} \rho d\phi \\
&= \lim_{\rho \to 0} \int_{-\pi}^{\pi} -a_{TM}^{inc} \kappa_0 \frac{-j2}{\pi \kappa_0 \rho} e^{-j\beta_0 z} \rho d\phi \\
&= -a_{TM}^{inc} \kappa_0 \frac{-j2}{\pi \kappa_0} e^{-j\beta_0 z} 2\pi \\
&\Rightarrow a_{TM}^{inc} = \frac{I_0}{4j}. \qquad (2.87)
\end{aligned}
$$

Thus, the radiated electric and magnetic fields for the line current considered are

$$E_\phi^{inc} = 0, \qquad (2.88)$$

$$E_z^{inc} = \frac{1}{j\omega\varepsilon_0} \frac{I_0}{4j} \kappa_0^2 H_0^{(2)}(\kappa_0 \rho) e^{-j\beta_0 z}, \qquad (2.89)$$

$$H_\phi^{inc} = -\frac{I_0}{4j} \kappa_0 H_0'^{(2)}(\kappa_0 \rho) e^{-j\beta_0 z}, \qquad (2.90)$$

$$H_z^{inc} = 0. \qquad (2.91)$$

When a magnetic type line current is located at the origin then the corresponding electric and magnetic fields can be determined similarly. But, more simply, duality principle may be utilized and the radiated fields can be determined from the expressions in (2.87)-(2.91). Assume a magnetic type line current carries a current M_0,

$$\mathbf{M} = \mathbf{a}_z M_0 e^{-j\beta_0 z}. \qquad (2.92)$$

According to the duality principle, the variables appearing in (2.87)- (2.91) should be replaced as follows:

$$I_0 \to M_0, \qquad (2.93)$$

$$E^{inc} \to H^{inc}, \qquad (2.94)$$

$$H^{inc} \to -E^{inc}, \qquad (2.95)$$

$$\mu_0 \to \varepsilon_0, \qquad (2.96)$$

$$\varepsilon_0 \to \mu_0 . \tag{2.97}$$

The radiated electric and magnetic fields for the magnetic line current are

$$a_{TE}^{inc} = \frac{M_0}{4j} , \tag{2.98}$$

$$H_\phi^{inc} = 0 , \tag{2.99}$$

$$H_z^{inc} = \frac{1}{j\omega\mu_0} \frac{M_0}{4j} \kappa_0^2 H_0^{(2)}(\kappa_0 \rho) e^{-j\beta_0 z} , \tag{2.100}$$

$$E_\phi^{inc} = \frac{M_0}{4j} \kappa_0 H_0'^{(2)}(\kappa_0 \rho) e^{-j\beta_0 z} , \tag{2.101}$$

$$E_z^{inc} = 0 . \tag{2.102}$$

3. SCATTERING FROM CYLINDRICAL SURFACES CONSISTING OF FREE-STANDING STRIPS OR SLOTS

Periodic cylindrical structures consisting of free-standing conducting patches or slots are analyzed. When formulating the problem, the scattered waves are written as infinite sums of the Floquet modes with unknown weighting coefficients. The weighting coefficients are related to the surface currents (aperture fields) of the conducting patches (slots) by applying the appropriate boundary conditions. Later on, an integral equation is obtained for the surface currents (aperture fields) and solved numerically by using the MM techniques. The infinite sums appearing in the MM solutions are seen to be slowly convergent. The infinite sums should be handled properly in order to circumvent slow convergence difficulties. One approach in such a case is to use sub-domain basis functions in conjunction with a conjugate gradient fast Fourier transform method as suggested in [10]. Another approach is to use entire-domain basis functions together with a convergence acceleration method that is based on a Kummer's series acceleration method, as described in [18, 21]. Here, we follow the second approach to accelerate the infinite sums.

3.1. Determination of the scattered waves from the free-standing strips

Consider a cylindrical structure consisting of free-standing periodically located rectangular strips of dimension $l \times w$ as shown in Figure 3.1. The periodicities in ϕ and z directions are denoted by T_ϕ and $T_{z,}$, respectively. The cylindrical surface is located at $\rho = \rho_0$.

When a plane wave is incident on the structure, the incident plane wave can be decomposed into cylindrical waves. This procedure is described in section 2.2. If the incident plane wave has a unit amplitude vector potential and its polarization is TM, its cylindrical wave components are of the form

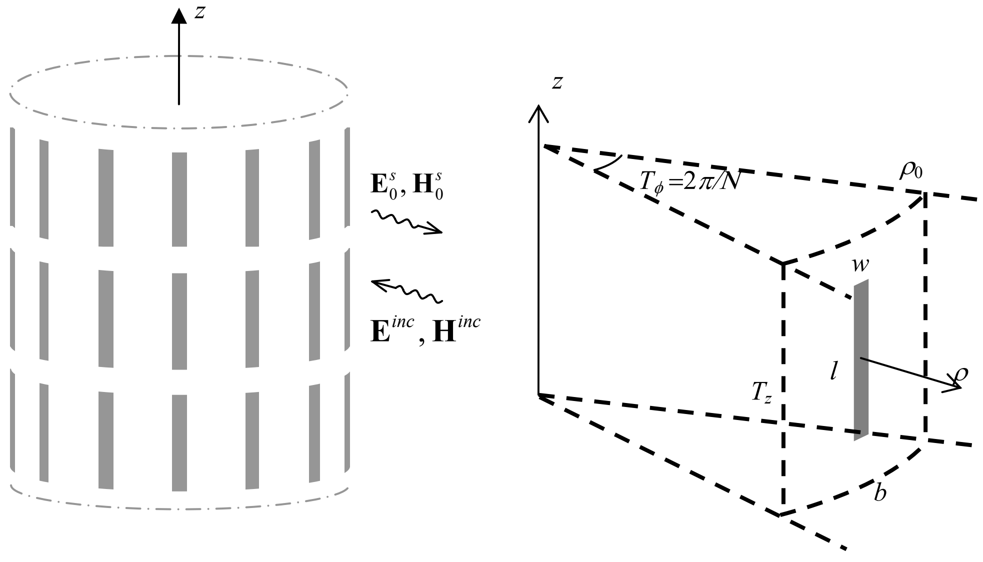

(a) **(b)**

Figure 3.1. a) A cylindrical structure consisting of free-standing rectangular strips that are periodically located on a cylindrical surface. A cylindrical TM wave is incident on the structure **(b)** A unit cell at ϕ=0, showing the parameters of the problem. N denotes the number of strips in ϕ direction.

$$A_{TM}^{inc} = a_{TM}^{inc} J_{v_0}(\kappa_0 \rho) e^{-jv_0\phi} e^{-j\beta_0 z}, \tag{3.1}$$

where

$$a_{TM}^{inc} = e^{jv_0(\phi^{inc} - \pi/2)}, \tag{3.2}$$

$$\beta_0 = k_0 \cos\theta^{inc}, \tag{3.3}$$

$$\kappa_0 = k_0 \sin\theta^{inc}, \tag{3.4}$$

v_0 denotes an integer, θ^{inc} and ϕ^{inc} denote propagation directions of the incident wave. The corresponding electric fields are obtained as

$$E_\phi^{inc} = \frac{-1}{j\omega\varepsilon_0 \rho} a_{TM} v_0 \beta_0 J_{v_0}(\kappa_0 \rho) e^{-jv_0\phi} e^{-j\beta_0 z}, \tag{3.5}$$

$$E_z^{inc} = \frac{1}{j\omega\varepsilon_0} a_{TM}^{inc} \kappa_0^2 J_{v_m}(\kappa_0 \rho_0) e^{-jv_0\phi} e^{-j\beta_0 z}. \tag{3.6}$$

Such an excitation induces surface currents on the conducting strips. In turn, these currents radiate giving rise to scattered waves. In accordance with the Floquet Theorem described in Chapter 2, the scattered waves are represented as infinite sums of the Floquet modes. If the strip widths are very small compared to the free-space wavelength, then ϕ components of the surface currents may be ignored. As a consequence, the scattered fields can be derived from the vector potentials;

$$A^s_{TM,0} = \sum_m \sum_n a_{TM,0mn} H^{(2)}_{v_m}(\kappa_n \rho)\psi_{mn}(\phi, z) \text{ for } \rho_0 < \rho, \tag{3.7}$$

$$A^s_{TM,1} = \sum_m \sum_n a_{TM,1mn} J_{v_m}(\kappa_n \rho)\psi_{mn}(\phi, z) \text{ for } \rho < \rho_0, \tag{3.8}$$

where the weighting coefficients $a_{TM,0mn}$ and $a_{TM,1mn}$ denote unknowns to be determined from boundary conditions of the problem. The Floquet modes are given in Chapter 2:

$$\psi_{mn}(\phi, z) = \frac{e^{-jv_m\phi}e^{-j\beta_n z}}{\sqrt{T_\phi T_z}}, \tag{3.9}$$

$$\beta_n = \beta_0 + 2\pi n / T_z, \tag{3.10}$$

$$v_m = v_0 + 2\pi m / T_\phi, \tag{3.11}$$

$$\kappa_n = \sqrt{k_0^2 - \beta_n^2}. \tag{3.12}$$

Here v_0 and β_0 denote the phase constants of the exciting wave in the circumferential and longitudinal directions, respectively. In the summations, J_{v_m} and $H^{(2)}_{v_m}$ respectively denote the Bessel functions of the first kind and the Hankel functions of the second kind, both of order v_m. Note that in the external region, the Hankel functions of the second kind are chosen to represent the outward traveling waves. But for the internal region, the Bessel functions of the first kind are used due to the standing wave nature of the waves in this region.

In order to determine the unknown coefficients in (3.7) and (3.8), boundary conditions are applied. The boundary conditions of the problem are:

a. Tangential components of the total electric field should be continuous at $\rho = \rho_0$,

b. Tangential components of the total magnetic field should be discontinuous at $\rho = \rho_0$ by an amount equal to the induced current density J_z.

The tangential electric and magnetic fields are obtained from the vector potentials in (3.7) and (3.8) by using the expressions (2.45)-(2.48).The fields in the external region are therefore

$$E_{0\phi}^{s}(\rho,\phi,z) = \frac{-1}{j\omega\varepsilon_0\rho}\sum_m\sum_n a_{TM,0mn}\nu_m\beta_n H_{\nu_m}^{(2)}(\kappa_n\rho)\psi_{mn}(\phi,z)\,, \tag{3.13}$$

$$E_{0z}^{s}(\rho,\phi,z) = \frac{1}{j\omega\varepsilon_0}\sum_m\sum_n a_{TM,0mn}\kappa_n^2 H_{\nu_m}^{(2)}(\kappa_n\rho)\psi_{mn}(\phi,z)\,, \tag{3.14}$$

$$H_{0\phi}^{s}(\rho,\phi,z) = -\sum_m\sum_n a_{TM,0mn}\kappa_n H_{\nu_m}'^{(2)}(\kappa_n\rho)\psi_{mn}(\phi,z)\,, \tag{3.15}$$

$$H_{0z}^{s}(\rho,\phi,z) = 0\,. \tag{3.16}$$

The fields in the internal region are expressed similarly. However in this case all Hankel functions of the second kind ($H_{\nu_m}^{(2)}$) are replaced by the Bessel functions of the first kind (J_{ν_m}), that is,

$$E_{1\phi}^{s}(\rho,\phi,z) = \frac{-1}{j\omega\varepsilon_0\rho}\sum_m\sum_n a_{TM,1mn}\nu_m\beta_n J_{\nu_m}(\kappa_n\rho)\psi_{mn}(\phi,z)\,, \tag{3.17}$$

$$E_{1z}^{s}(\rho,\phi,z) = \frac{1}{j\omega\varepsilon_0}\sum_m\sum_n a_{TM,1mn}\kappa_n^2 J_{\nu_m}(\kappa_n\rho)\psi_{mn}(\phi,z)\,, \tag{3.18}$$

$$H_{1\phi}^{s}(\rho,\phi,z) = -\sum_m\sum_n a_{TM,1mn}\kappa_n J_{\nu_m}'(\kappa_n\rho)\psi_{mn}(\phi,z)\,, \tag{3.19}$$

$$H_{1z}^{s}(\rho,\phi,z) = 0\,. \tag{3.20}$$

The boundary conditions are then applied

$$\frac{-1}{j\omega\varepsilon_0\rho_0}\sum_m\sum_n a_{TM,1mn}\nu_m\beta_n J_{\nu_m}(\kappa_n\rho_0)\psi_{mn}(\phi,z) =$$

$$\frac{-1}{j\omega\varepsilon_0\rho_0}\sum_m\sum_n a_{TM,0mn}v_m\beta_n H_{v_m}^{(2)}(\kappa_n\rho_0)\psi_{mn}(\phi,z), \quad (3.21)$$

$$\frac{1}{j\omega\varepsilon_0}\sum_m\sum_n a_{TM,1mn}\kappa_n^2 J_{v_m}(\kappa_n\rho_0)\psi_{mn}(\phi,z) =$$

$$\frac{1}{j\omega\varepsilon_0}\sum_m\sum_n a_{TM,0mn}\kappa_n^2 H_{v_m}^{(2)}(\kappa_n\rho_0)\psi_{mn}(\phi,z), \quad (3.22)$$

$$\sum_m\sum_n a_{TM,1mn}\kappa_n J_{v_m}'(\kappa_n\rho_0)\psi_{mn}(\phi,z) =$$

$$J_z + \sum_m\sum_n a_{TM,0mn}\kappa_n H_{v_m}'^{(2)}(\kappa_n\rho_0)\psi_{mn}(\phi,z). \quad (3.23)$$

If the inner product operation described in Chapter 2 is employed, the equations that hold for doubly-infinite sums simplify. By taking the inner products of both sides of the equations with the Floquet modes, the boundary conditions become

$$a_{TM,1mn}J_{v_m}(\kappa_n\rho_0) = a_{TM,0mn}H_{v_m}^{(2)}(\kappa_n\rho_0), \quad (3.24)$$

$$a_{TM,1mn}J_{v_m}(\kappa_n\rho_0) = a_{TM,0mn}H_{v_m}^{(2)}(\kappa_n\rho_0), \quad (3.25)$$

$$a_{TM,1mn}\kappa_n J_{v_m}'(\kappa_n\rho_0) = a_{TM,0mn}\kappa_n H_{v_m}'^{(2)}(\kappa_n\rho_0) + \langle J_z, \psi_{mn}^*(\phi,z)\rangle. \quad (3.26)$$

The resultant equations can then be solved for the coefficients $a_{TM,0mn}$ and $a_{TM,1mn}$. The coefficients for the fields in the external region are

$$a_{TM,0mn} = \frac{-j}{2}\pi\rho_0 J_{v_m}(\kappa_n\rho_0)\langle J_z, \psi_{mn}^*(\phi,z)\rangle. \quad (3.27)$$

In obtaining the expression (3.27), the Wronskian relation

$$J_{v_m}(\kappa_n\rho)H_{v_m}'^{(2)}(\kappa_n\rho) - J_{v_m}'(\kappa_n\rho)H_{v_m}^{(2)}(\kappa_n\rho) = \frac{-i2}{\pi\kappa_n\rho}, \quad (3.28)$$

is utilized [24].

So far, the scattered fields are expressed in terms of the surface current J_z. However, it is still an unknown quantity in the formulation above and has to be determined using the additional boundary condition that the total tangential electric field has to be zero at the surface of a strip. Note that the surface current is also related to the incident wave. Then the surface current can be computed numerically by using the MM technique.

3.2. An integral equation for the surface currents and the MM Solution

As mentioned, an integral equation for the problem considered in this chapter is obtained by equating total tangential electric fields to zero across a strip surface. Since the strips are oriented in z direction and their widths are very narrow, only z components of the electric fields are taken into consideration. So starting with

$$E_{0z}^{s}(\rho_0,\phi,z)+E_{z}^{inc}(\rho_0,\phi,z)=0 \text{ on the strip,} \tag{3.29}$$

where E_z^{inc} denotes the exciting and E_{0z}^{s} the scattered electric field respectively. From the expression (2.46), we have

$$E_{0z}^{s}(\rho,\phi,z)=\frac{1}{j\omega\varepsilon_0}\sum_m\sum_n a_{TM,0mn}\kappa_n^2 H_{v_m}^{(2)}(\kappa_n\rho)\psi_{mn}(\phi,z)=$$
$$\frac{1}{j\omega\varepsilon_0}\sum_m\sum_n \frac{-j}{2}\pi\rho_0 J_{v_m}(\kappa_n\rho_0)<J_z,\psi_{mn}^{*}(\phi,z)>\kappa_n^2 H_{v_m}^{(2)}(\kappa_n\rho)\psi_{mn}(\phi,z)\,. \tag{3.30}$$

E_z^{inc} is obtained from the vector potential of the incident wave as in (3.1). Therefore the exciting electric field is

$$E_z^{inc}(\rho,\phi,z)=\frac{1}{j\omega\varepsilon_0}a_{TM}^{inc}\kappa_0^2 J_{v_m}(\kappa_0\rho)e^{-jv_0\phi}e^{-j\beta_0 z}\,. \tag{3.31}$$

An integral equation is then obtained as follows

$$E_{0z}^{s}(\rho_0,\phi,z)=-E_z^{inc}(\rho_0,\phi,z)\,,$$

$$\frac{1}{j\omega\varepsilon_0}\sum_{mn}\frac{-j}{2}\pi\rho_0 J_{v_m}(\kappa_n\rho_0)<J_z,\psi_{mn}^{*}(\phi,z)>\kappa_n^2 H_{v_m}^{(2)}(\kappa_n\rho_0)\psi_{mn}(\phi,z)=$$
$$\frac{-1}{j\omega\varepsilon_0}a_{TM}^{inc}\kappa_0^2 J_{v_m}(\kappa_0\rho_0)e^{-jv_0\phi}e^{-j\beta_0 z}\,,$$

and finally

$$\sum_{mn}Z_{zz_0}<J_z,\psi_{mn}^{*}(\phi,z)>\psi_{mn}(\phi,z)=\frac{-1}{j\omega\varepsilon_0}a_{TM}^{inc}\kappa_0^2 J_{v_m}(\kappa_0\rho_0)e^{-jv_0\phi}e^{-j\beta_0 z} \text{ on } \partial S\,, \tag{3.32}$$

where

$$Z_{zz_0}=\frac{-\pi\rho_0}{2\omega\varepsilon_0}\kappa_n^2 J_{v_m}(\kappa_n\rho_0)H_{v_m}^{(2)}(\kappa_n\rho_0)\,. \tag{3.33}$$

Here ∂S denotes the strip surface. That is,

$$\partial S = \{\rho = \rho_0 \, ; -w/2a < \phi < w/2a \, ; -l/2 < z < l/2\}. \tag{3.34}$$

This integral equation may be solved numerically by using a MM technique. For obtaining a numerical solution, the current is expanded into entire domain sinusoidal basis functions for narrow strips [25]

$$J_z = \sum_{q=1}^{Q} c_q f_q \, , \tag{3.35}$$

where

$$f_q = \sin\left\{\tfrac{q\pi}{l}\left(z + \tfrac{l}{2}\right)\right\}, \tag{3.36}$$

and c_q denote unknown expansion coefficients. Substituting the expansion of the current into the integral equation, one obtains

$$\sum_{q=1}^{Q} c_q \sum_m \sum_n Z_{zz_0} < f_q , \psi^*_{mn}(\phi, z) > \psi_{mn}(\phi, z) = \frac{-1}{j\omega\varepsilon_0} \kappa_0^2 a_{TM}^{inc} J_{v_m}(\kappa_0 \rho_0) e^{-jv_0\phi} e^{-j\beta_0 z} \text{ on } \partial S \tag{3.37}$$

In accordance with the Galerkin's method, by taking inner products of both sides of (3.37) with basis functions f_p, a new equation

$$\sum_{q=1}^{Q} c_q \sum_m \sum_n Z_{zz_0} < f_q , \psi^*_{mn}(\phi, z) >< f_p , \psi_{mn}(\phi, z) > = \frac{-1}{j\omega\varepsilon_0} \kappa_0^2 a_{TM}^{inc} J_{v_m}(\kappa_0 \rho_0) < f_p , e^{-jv_0\phi} e^{-j\beta_0 z} >, \tag{3.38}$$

is obtained. This is performed for p=1, 2, . . ., Q. This results in a set of equations that can be written in matrix form

$$\begin{bmatrix} A_{11} & A_{12} & \cdots & \\ A_{21} & A_{22} & \cdots & \\ \vdots & \vdots & \ddots & \\ & & & A_{QQ} \end{bmatrix} \begin{bmatrix} c_1 \\ c_2 \\ \vdots \\ c_Q \end{bmatrix} = \begin{bmatrix} B_1 \\ B_2 \\ \vdots \\ B_Q \end{bmatrix}, \tag{3.39}$$

where

$$A_{pq} = \sum_m \sum_n Z_{zz_0} < f_q, \psi^*_{mn}(\phi, z) >< f_p, \psi_{mn}(\phi, z) >$$
$$= \frac{-\pi\rho_0}{2\omega\varepsilon_0} \sum_m \sum_n \kappa_n^2 J_{v_m}(\kappa_n \rho_0) H^{(2)}_{v_m}(\kappa_n \rho_0) C^*_{nq} C_{np} S^2_{v_m} \,, \tag{3.40}$$

$$B_p = -\frac{1}{j\omega\varepsilon_0} \kappa_0^2 a^{inc}_{TM} J_{v_m}(\kappa_0 \rho_0) < f_p, e^{-jv_0\phi} e^{-j\beta_0 z} >= -a^{inc}_{TM} \frac{\kappa_0^2}{j\omega\varepsilon_0} J_{v_m}(\kappa_0 \rho_0) \sqrt{T_\phi T_z} S_{v_0} C_{0p} \,, \tag{3.41}$$

$$C_{np} = \int_{-l/2}^{l/2} \sin\left\{\tfrac{p\pi}{l}(z + \tfrac{l}{2})\right\} \frac{e^{-j\beta_n z}}{\sqrt{T_z}} dz = \frac{p\pi l}{\sqrt{T_z}} \frac{(-1)^p e^{-j\beta_n l/2} - e^{j\beta_n l/2}}{(\beta_n l)^2 - (p\pi)^2} \,, \tag{3.42}$$

$$C^*_{nq} = \int_{-l/2}^{l/2} \sin\left\{\tfrac{q\pi}{l}(z + \tfrac{l}{2})\right\} \frac{\left(e^{-j\beta_n z}\right)^*}{\sqrt{T_z}} dz = \frac{q\pi l}{\sqrt{T_z}} \frac{(-1)^q e^{j\beta_n l/2} - e^{-j\beta_n l/2}}{(\beta_n l)^2 - (q\pi)^2} \,, \tag{3.43}$$

$$S_{v_m} = \int_{-\frac{w}{2a}}^{\frac{w}{2a}} \frac{e^{-jv_m\phi}}{\sqrt{T_\phi}} d\phi = \frac{w}{a\sqrt{T_\phi}} \frac{\sin\left(\frac{w}{2a} v_m\right)}{\frac{w}{2a} v_m} \,. \tag{3.44}$$

In the computations of the matrix elements A_{pq} in (3.40), the infinite sum with respect to the summation index m is seen to be slowly convergent. Therefore we use a convenient computation method that is based on a Kummer's series acceleration method to circumvent the slow convergence difficulty.

As the summation index m in (3.40) tends to infinity, it is noted that the products of the Bessel functions asymptotically equal to

$$J_{v_m}(\kappa_n \rho_0) H^{(2)}_{v_m}(\kappa_n \rho_0) \cong \frac{j}{\pi |v_m|} \text{ as } |v_m| = |v_0 + 2\pi m / T_\phi| = |v_0 + mN| \to \infty \,, \tag{3.45}$$

where "||" means an absolute value and N denotes the number of strips in ϕ direction such that $T_\phi = 2\pi / N$. Then it is convenient to compute A_{pq} as follows:

$$A_{pq} = \frac{-\pi\rho_0}{2\omega\varepsilon_0} \sum_m \sum_n \kappa_n^2 C^*_{nq} C_{np} \kappa_n^2 J_{v_m}(\kappa_n \rho_0) H^{(2)}_{v_m}(\kappa_n \rho_0) C^*_{nq} C_{np} S^2_{v_m}$$
$$= \frac{-\pi\rho_0}{2\omega\varepsilon_0} \sum_{n=-\infty}^{\infty} \kappa_n^2 C^*_{nq} C_{np} \sum_{m=-\infty}^{\infty} S^2_{v_m} J_{v_m}(\kappa_n \rho_0) H^{(2)}_{v_m}(\kappa_n \rho_0)$$
$$= \frac{-\pi\rho_0}{2\omega\varepsilon_0} \sum_{n=-\infty}^{\infty} \kappa_n^2 C^*_{nq} C_{np} \left\{ \sum_{m=-\infty}^{\infty} S^2_{v_m} \left(J_{v_m}(\kappa_n \rho_0) H^{(2)}_{v_m}(\kappa_n \rho_0) - \frac{j}{\pi |v_m|} \right) + \sum_{m=-\infty}^{\infty} S^2_{v_m} \frac{j}{\pi |v_m|} \right\}$$
$$= \frac{-\pi\rho_0}{2\omega\varepsilon_0} \sum_{n=-\infty}^{\infty} \kappa_n^2 C^*_{nq} C_{np} \left\{ \sum_{m=-\infty}^{\infty} S^2_{v_m} \left(J_{v_m}(\kappa_n \rho_0) H^{(2)}_{v_m}(\kappa_n \rho_0) - \frac{j}{\pi |v_m|} \right) + I \right\}$$

$$= \frac{-\pi\rho_0}{2\omega\varepsilon_0} \sum_{n=-\infty}^{\infty} \kappa_n^2 C_{nq}^* C_{np} \sum_{m=-\infty}^{\infty} S_{v_m}^2 \left(J_{v_m}(\kappa_n\rho_0) H_{v_m}^{(2)}(\kappa_n\rho_0) - \frac{j}{\pi\,|\,v_m\,|} \right) + \frac{-\pi\rho_0}{2\omega\varepsilon_0} I \sum_{n=-\infty}^{\infty} \kappa_n^2 C_{nq}^* C_{np} \,, \tag{3.46}$$

where

$$I = \frac{j}{\pi} \sum_{m=-\infty}^{\infty} \frac{S_{v_m}^2}{|\,v_m\,|} = \frac{jw^2}{\pi N \rho_0^2 T_\phi} \sum_{m=-\infty}^{\infty} \frac{\sin^2\big((v_0/N+m)\pi w/b\big)}{(\pi w/b)^2\,|\,v_0/N+m\,|^3} \,. \tag{3.47}$$

Now, the infinite sum with respect to *m* in (3.46) converges more rapidly. However, the infinite sum in (3.47) converges slowly as shown in [18, 21]. In Appendix A, a computation scheme for slowly convergent infinite sums is described. Also, as an example, the computation of (3.47) is provided in the same appendix.

Once the MM solution of the problem is obtained for the surface current, the coefficients $a_{TM,0mn}$ in (3.27) are expressed in terms of the current coefficients c_q as follows :

$$\begin{aligned} a_{TM,0mn} &= \frac{-j}{2} \pi\rho_0 J_{v_m}(\kappa_n\rho_0) < J_z, \psi_{mn}^*(\phi,z) > \\ &= \frac{-j}{2} \pi\rho_0 J_{v_m}(\kappa_n\rho_0) \sum_{q=1}^{Q} c_q < f_q, \psi_{mn}^*(\phi,z) > \\ &= \frac{-j}{2} \pi\rho_0 J_{v_m}(\kappa_n\rho_0) \left\{ \sum_{q=1}^{Q} c_q C_{nq}^* \right\} S_{v_m} \,. \end{aligned} \tag{3.48}$$

By using these coefficients, the scattered fields are determined by using the expressions in (2.45)-(2.48)

$$E_{0\phi}^s = \frac{\pi}{2\omega\varepsilon_0} \sum_m \sum_n \left\{ \sum_{q=1}^{Q} c_q C_{nq}^* \right\} S_{v_m} v_m \beta_n J_{v_m}(\kappa_n\rho_0) H_{v_m}^{(2)}(\kappa_n\rho) \psi_{mn}(\phi,z) \,, \tag{3.49}$$

$$E_{0z}^s = \frac{-\pi\rho_0}{2\omega\varepsilon_0} \sum_m \sum_n \left\{ \sum_{q=1}^{Q} c_q C_{nq}^* \right\} S_{v_m} \kappa_n^2 J_{v_m}(\kappa_n\rho_0) H_{v_m}^{(2)}(\kappa_n\rho) \psi_{mn}(\phi,z) \tag{3.50}$$

$$H_{0\phi}^s(\rho,\phi,z) = \frac{j}{2} \pi\rho_0 \sum_m \sum_n \left\{ \sum_{q=1}^{Q} c_q C_{nq}^* \right\} S_{v_m} \kappa_n J_{v_m}(\kappa_n\rho_0) H_{v_m}'^{(2)}(\kappa_n\rho) \psi_{mn}(\phi,z) \,, \tag{3.51}$$

$$H_{0z}^s(\rho,\phi,z) = 0 \,. \tag{3.52}$$

The scattered fields obtained so far correspond to a single cylindrical wave excitation of the form given in (3.1). However, if the excitation is a plane wave then the scattered fields are determined separately for each cylindrical wave components of the incident plane wave. Using the superposition principle, the total scattered fields are then obtained by summing the individual scattered fields. The decomposition of a plane wave into the cylindrical wave components has already been considered in Section 2.2. The RCS of the problem is therefore

$$RCS = \lim_{\rho \to \infty} 2\pi\rho \frac{\left| \sum_{v_0=-\infty}^{\infty} \mathbf{H}^s(\rho,\phi,z) \right|^2}{\left| \mathbf{H}^i \right|^2}. \tag{3.53}$$

Here the infinite sum in the numerator indicates the total scattered magnetic field and $\mathbf{H}^i$ denotes the magnetic field of the incident plane wave. As shown in Chapter 2, when the vector potential of the incident plane wave has unit amplitude, the absolute value of the magnetic field is given by

$$\left| \mathbf{H}^i \right| = \kappa_0 = k_0 \sin\theta^{inc}. \tag{3.54}$$

On the other hand, the scattered magnetic fields in the far field region are determined from the expression (3.51) by using the asymptotic form for the Hankel functions [24],

$$H_{v_m}^{(2)}(\kappa_n \rho) \approx \sqrt{\frac{2}{\pi \kappa_n \rho}} e^{j\pi/4 + jv_m\pi/2} e^{-j\kappa_n\rho} \text{ ; as } \rho \to \infty, \tag{3.55}$$

$$H_{v_m}'^{(2)}(\kappa_n \rho) \approx -j\sqrt{\frac{2}{\pi \kappa_n \rho}} e^{j\pi/4 + jv_m\pi/2} e^{-j\kappa_n\rho} \text{ ; as } \rho \to \infty. \tag{3.56}$$

Thus the absolute value of the total scattered magnetic field in the far field region is obtained as follows

$$\left| \sum_{v_0=-\infty}^{\infty} \mathbf{H}^s(\rho,\phi,z) \right|^2 = \left| \sum_{v_0=-\infty}^{\infty} H_{0\phi}^s(\rho,\phi,z) \right|^2$$

$$= \left| \sum_{v_0=-\infty}^{\infty} \frac{j}{2} \pi\rho_0 \sum_m \sum_n \left\{ \sum_{q=1}^{Q} c_q C_{nq}^* \right\} S_{v_m} \kappa_n J_{v_m}(\kappa_n \rho_0) H_{v_m}'^{(2)}(\kappa_n \rho) \psi_{mn}(\phi,z) \right|^2$$

$$= \frac{\rho_0^2 \pi}{2\rho T_\phi T_z} \left| \sum_{v_0=-\infty}^{\infty} \sum_{m=-\infty}^{\infty} \sum_{n=-\infty}^{\infty} \sum_{q=1}^{Q} c_q C_{nq}^{*} S_{v_m} \sqrt{\kappa_n} J_{v_m}(\kappa_n \rho_0) e^{-j(\kappa_n \rho + v_m(\varphi - \pi/2) + \beta_n z)} \right|^2 \text{, as } \rho \to \infty \quad (3.57)$$

and the RCS is determined from

$$RCS = \lim_{\rho \to \infty} \frac{2\pi\rho}{(k_0 \sin\theta^{inc})^2} \left| \sum_{v_0=-\infty}^{\infty} \mathbf{H}^s(\rho, \phi, z) \right|^2$$
$$= \frac{\rho_0^2 \pi^2}{(k_0 \sin\theta^{inc})^2 T_\phi T_z} \left| \sum_{v_0=-\infty}^{\infty} \sum_{m=-\infty}^{\infty} \sum_{n=-\infty}^{\infty} \sum_{q=1}^{Q} c_q C_{nq}^{*} S_{v_m} \sqrt{\kappa_n} J_{v_m}(\kappa_n \rho_0) e^{-j(\kappa_n \rho + v_m(\varphi - \pi/2) + \beta_n z)} \right|^2 . \quad (3.58)$$

Electromagnetic field couplings into the cylindrical structures have some practical importance in antenna applications. The coupling is defined as the total power measured at the center of a cylindrical structure when a plane wave is incident on the structure. As discussed in section 2.3, the coupling can be determined by considering the far fields radiated from an electric type line current located at the center of the cylindrical structure shown in Figure 3.1. The coupling is determined using

$$Coupling = \lim_{\rho \to \infty} \frac{\left| H_\phi^{inc} + H_{0\phi}^{s} \right|^2}{\left| H_\phi^{inc} \right|^2}, \quad (3.59)$$

where H^s denotes the scattered magnetic field in the presence of the cylindrical structure; H^{inc} denotes the incident magnetic field in the absence of the cylindrical structure, as given in section 2.3. As $\rho \to \infty$, the limiting value of the expression in (2.84) is obtained as

$$H_\phi^{inc} = -a_{TM}^{inc} \kappa_0 H_0'^{(2)}(\kappa_0 \rho) e^{-j\beta_0 z}$$
$$\cong -a_{TM}^{inc} \kappa_0 \left(-j\right) \sqrt{\frac{2}{\pi \kappa_0 \rho}} e^{j\pi/4} e^{-j\kappa_0 \rho} e^{-j\beta_0 z}$$
$$\cong j a_{TM}^{inc} \sqrt{\frac{2\kappa_0}{\pi \rho}} e^{j\pi/4} e^{-j\kappa_0 \rho} e^{-j\beta_0 z} \text{ as } \rho \to \infty, \quad (3.60)$$

and the coupling is determined by using this expression and the corresponding asymptotic expression of the scattered magnetic field in (3.57).

3.3. Determination of the scattered waves from axial slots and the Equivalence principle

Now consider a periodic cylindrical structure as shown in Figure 3.2, which consists of a perfectly conducting circular cylinder perforated periodically with axial slots. The periodicities in the circumferential and longitudinal directions are denoted by T_ϕ and T_z respectively as shown in the unit cell of the problem. In the figure, the slot dimensions are taken as $w \times l$.

When a plane wave is incident on the structure, the incident plane wave can be decomposed into cylindrical waves. This procedure has already been described in Chapter 2. If the incident plane wave has unit amplitude vector potential and its polarization is TE, its cylindrical wave components are of the form

$$A_{TE}^{inc} = a_{TE}^{inc} J_{v_0}(\kappa_0 \rho) e^{-jv_0\phi} e^{-j\beta_0 z}, \tag{3.61}$$

where

$$\beta_0 = k_0 \cos\theta^{inc}, \tag{3.62}$$

$$\kappa_0 = k_0 \sin\theta^{inc}, \tag{3.63}$$

$$a_{TE}^{inc} = e^{jv_0(\phi^{inc} - \pi/2)}, \tag{3.64}$$

v_0 denotes an integer, θ^{inc} and ϕ^{inc} denote propagation directions of the incident wave. The corresponding magnetic fields are obtained as

$$H_\phi^{inc} = -\frac{1}{j\omega\mu_0\rho} a_{TE}^{inc} v_0 \beta_0 J_{v_0}(\kappa_0 \rho) e^{-jv_0\phi} e^{-j\beta_0 z}, \tag{3.65}$$

$$H_z^{inc} = \frac{1}{j\omega\mu_0} \kappa_0^2 a_{TE}^{inc} J_{v_m}(\kappa_0 \rho) e^{-jv_0\phi} e^{-j\beta_0 z}. \tag{3.66}$$

Such an excitation induces aperture fields across the slotted regions of the conducting cylinder. Scattered fields of the problem are assumed to be radiated by those aperture fields. In accordance with the Floquet Theorem described in Chapter 2, the scattered fields are represented as infinite sums of the Floquet modes. If the slots are very thin compared to the free-space wavelength, then *z* components of the aperture fields may be ignored. As a consequence of this the scattered fields can be derived from the vector potentials

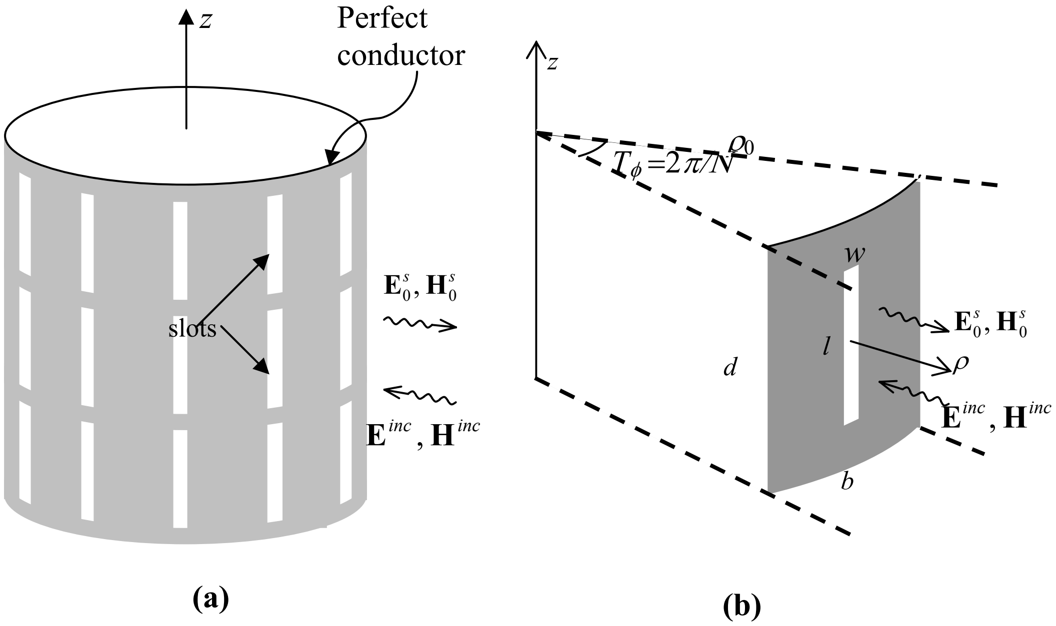

Figure 3.2. A perfectly conducting circular cylinder perforated periodically with axial slots. A cylindrical TE wave is incident on the structure **(a)** Array geometry. **(b)** A unit cell of the problem at ϕ=0. N denotes the number of slots in ϕ direction.

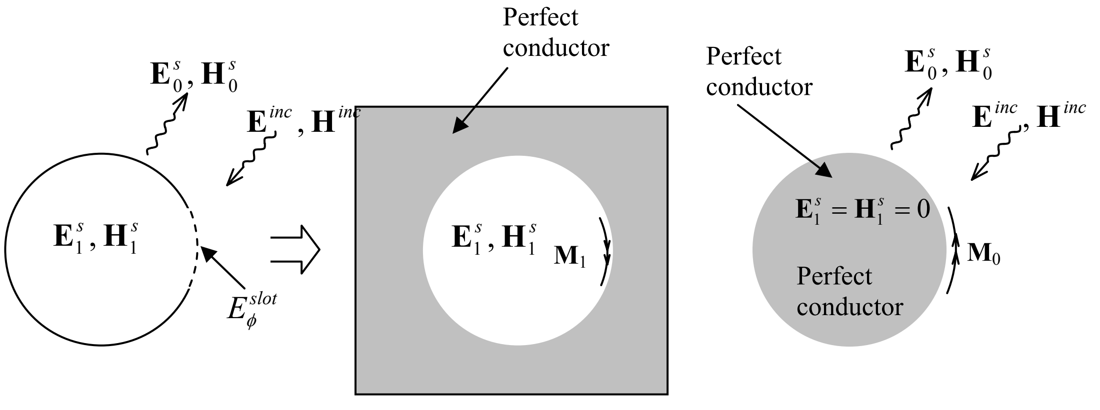

a) Top view of the original problem

b) Equivalent problem for the internal region

c) Equivalent problem for the external region

Figure 3.3. Application of the Equivalence Principle for the conducting circular cylinder with the slots. **a)** The original problem, **b)** The equivalent problem for the internal region. The aperture field in the original problem is replaced by a magnetic current $\mathbf{M}_1$, which radiates the fields $\mathbf{E}_1^s, \mathbf{H}_1^s$. **c)** The equivalent problem for the external region. A magnetic current $\mathbf{M}_0 = -\mathbf{M}_1$ radiates the fields $\mathbf{E}_0^s, \mathbf{H}_0^s$.

$$A_{TE,0}^{s} = \sum_{m}\sum_{n} a_{TE,0mn} J_{\nu_m}(\kappa_n \rho)\psi_{mn}(\phi, z) \qquad \text{for } \rho < \rho_0 \quad , \tag{3.67}$$

$$A_{TE,1}^{s} = \sum_{m}\sum_{n} a_{TE,1mn} H_{\nu_m}^{(2)}(\kappa_n \rho)\psi_{mn}(\phi, z) \qquad \text{for } \rho_0 < \rho \quad , \tag{3.68}$$

where the weighting coefficients $a_{TE,0mn}$ and $a_{TE,1mn}$ denote unknowns to be determined from boundary conditions of the problem. Note that for the external region, the Hankel functions of the second kind are chosen to represent outward traveling waves. But for the internal region, the Bessel functions of the first kind are used because the waves should be purely standing.

Before applying the boundary conditions of the problem, the Equivalence principle [23] is utilized. In accordance with the Equivalence Principle, the slots on the conducting cylinder are replaced by equivalent magnetic currents denoted by $\mathbf{M}_0$ and $\mathbf{M}_1$ for the external and internal regions as shown in Figure 3.3. An equivalent magnetic current in the external region is defined as

$$\mathbf{M}_0 = \mathbf{a}_\phi E_\phi^{slot} \times \mathbf{a}_\rho = -\mathbf{a}_z E_\phi^{slot} , \tag{3.69}$$

while the current for the internal region is defined as

$$\mathbf{M}_1 = \mathbf{a}_\phi E_\phi^{slot} \times (-\mathbf{a}_\rho) = \mathbf{a}_z E_\phi^{slot} . \tag{3.70}$$

Here E_ϕ^{slot} denote ϕ component of the electric field on the slotted region. In that case, the scattered fields for the external region are determined from the magnetic current $\mathbf{M}_0$, while the scattered fields for the internal region are determined from the magnetic current $\mathbf{M}_1$.

Consider the equivalent problem for the external region of the cylindrical structure shown in Figure 3.3.b. The current source $\mathbf{M}_0$ is backed by a perfectly conducting cylinder. In that case, a boundary condition for the scattered fields is

$$\mathbf{a}_\phi \mathbf{E}_0^s \times \mathbf{a}_\rho = \mathbf{M}_0 \text{ at } \rho = \rho_0 . \tag{3.71}$$

The scattered electric and magnetic fields are obtained from the vector potentials in (3.67) and (3.68) and by using the expression (2.45)-(2.48).The fields in the external region are therefore

$$E_{0\phi}^{s}=\sum_{m}\sum_{n}a_{TE,0mn}\kappa_{n}H_{v_m}^{\prime(2)}(\kappa_{n}\rho)\psi_{mn}(\phi,z)\,, \tag{3.72}$$

$$E_{0z}^{s}=0\,, \tag{3.73}$$

$$H_{0\phi}^{s}=-\frac{1}{j\omega\mu_{0}\rho}\sum_{m}\sum_{n}a_{TE,0mn}v_{m}\beta_{n}H_{v_m}^{(2)}(\kappa_{n}\rho)\psi_{mn}(\phi,z)\,, \tag{3.74}$$

$$H_{0z}^{s}=\frac{1}{j\omega\mu_{0}}\sum_{m}\sum_{n}a_{TE,0mn}\kappa_{n}^{2}H_{v_m}^{(2)}(\kappa_{n}\rho)\psi_{mn}(\phi,z)\,. \tag{3.75}$$

Similarly, the scattered fields in the internal region can be inferred from these expressions by replacing all occurrences of the Hankel functions ($H_{v_m}^{(2)}$) with the Bessel functions (J_{v_m}). The scattered fields in the internal region are

$$E_{1\phi}^{s}=\sum_{m}\sum_{n}a_{TE,1mn}\kappa_{n}J_{v_m}^{\prime}(\kappa_{n}\rho)\psi_{mn}(\phi,z)\,, \tag{3.76}$$

$$E_{1z}^{s}=0\,, \tag{3.77}$$

$$H_{1\phi}^{s}=-\frac{1}{j\omega\mu_{0}\rho}\sum_{m}\sum_{n}a_{TE,1mn}v_{m}\beta_{n}J_{v_m}(\kappa_{n}\rho)\psi_{mn}(\phi,z)\,, \tag{3.78}$$

$$H_{1z}^{s}=\frac{1}{j\omega\mu_{0}}\sum_{m}\sum_{n}a_{TE,1mn}\kappa_{n}^{2}J_{v_m}(\kappa_{n}\rho)\psi_{mn}(\phi,z)\,. \tag{3.79}$$

Performing the cross product operations in (3.71), a scalar equation involving infinite sums of Floquet modes is obtained. Taking the inner product of both sides of the resulting equation with Floquet modes, the unknown coefficients $a_{TE,0mn}$ are determined in terms of the slot field E_{ϕ}^{slot} ;

$$a_{TE,0mn}=\frac{<E_{\phi}^{slot},\psi_{mn}^{*}(\phi,z)>}{\kappa_{n}H_{v_m}^{\prime(2)}(\kappa_{n}\rho_{0})}\,. \tag{3.80}$$

Next, the equivalent problem for the internal region as shown in Figure 3.3.c is considered, where the current source $\mathbf{M}_1$ is backed by a perfectly conducting cylinder. In this case, the boundary condition requires that

$$\mathbf{a}_{\phi}\mathbf{E}_{1}^{s}\times(-\mathbf{a}_{\rho})=\mathbf{M}_{1}\ \text{at}\ \rho=\rho_{0}\,. \tag{3.81}$$

Similarly, using the expression (3.76), the unknown coefficients for the internal region are determined as

$$a_{TE,1mn} = \frac{< E_{\phi}^{slot}, \psi_{mn}^{*}(\phi, z) >}{\kappa_n J'_{v_m}(\kappa_n \rho_0)}. \tag{3.82}$$

Note that, the scattered fields are all expressed in terms of the slot field E_{ϕ}^{slot}. However, it is still an unknown quantity and has to be determined from an additional boundary condition. In the next section, an integral equation will be obtained for the slot field by using the fact that the total tangential magnetic fields are continuous on both sides of the slot.

3.4. An integral equation for the aperture fields and the MM Solution

The slot field is an unknown quantity and should be determined in terms of the exciting wave of the problem. The vector potential of the exciting wave is given in (3.61), and the corresponding magnetic field is given in (3.65). Since there is no electric current at the slotted region and the slots are narrow, we require that *z* components of the magnetic fields should be continuous across the slot. This requirement is written in a mathematical form

$$H_{1z}^{s} = H_{0z}^{s} + H_{z}^{inc} + H_{z}^{c}, \text{ on } \partial S. \tag{3.83}$$

Here ∂S refers to the slotted region, H_{z}^{inc} denote the magnetic field of the exciting wave, and H_{z}^{c} denote the magnetic field that would have been scattered by the conducting cylinder if the slots were not present. To determine H_{z}^{c}, consider a conducting cylinder without slots of radius ρ_0. Since the incident field is known, H_{z}^{c}, can be determined from TE fields

$$A_{TE}^{c} = a_{TE}^{c} H_{v_0}^{(2)}(\kappa_0 \rho) e^{-jv_0\phi} e^{-j\beta_0 z}. \tag{3.84}$$

The unknown coefficient is determined by writing a boundary condition for the corresponding electric fields of the vector potential. Since the tangential electric field must vanish on the surface of a conductor, the ϕ component of the total electric field should be equal to zero across the cylinder. That is,

$$E_\phi^{inc}(\rho_0) + E_\phi^{c}(\rho_0) = 0,$$

$$\kappa_0 a_{TE}^{inc} J'_{v_0}(\kappa_0\rho_0) e^{-jv_0\phi} e^{-j\beta_0 z} + \kappa_0 a_{TE}^{c} H'^{(2)}_{v_0}(\kappa_0\rho_0) e^{-jv_0\phi} e^{-j\beta_0 z} = 0,$$

and so

$$a_{TE}^{c} = \frac{-a_{TE}^{inc} J'_{v_0}(\kappa_0\rho_0)}{H'^{(2)}_{v_0}(\kappa_0\rho_0)}. \tag{3.85}$$

The corresponding electric fields are therefore

$$E_\phi^{inc} = -a_{TE}^{inc} \frac{J'_{v_0}(\kappa_0\rho_0)}{H'^{(2)}_{v_0}(\kappa_0\rho_0)} \kappa_0 H'^{(2)}_{v_0}(\kappa_0\rho) e^{-jv_0\phi} e^{-j\beta_0 z}. \tag{3.86}$$

Substituting (3.75), (3.79), (3.80), and (3.82) into (3.83) yields

$$\frac{1}{j\omega\mu_0}\sum_m\sum_n \frac{< E_\phi^{slot}, \psi_{mn}^*(\phi,z) >}{\kappa_n J'_{v_m}(\kappa_n\rho_0)} \kappa_n^2 J_{v_m}(\kappa_n\rho_0)\psi_{mn}(\phi,z) =$$
$$\frac{1}{j\omega\mu_0}\sum_m\sum_n \frac{< E_\phi^{slot}, \psi_{mn}^*(\phi,z) >}{\kappa_n H'^{(2)}_{v_m}(\kappa_n\rho_0)} \kappa_n^2 H^{(2)}_{v_m}(\kappa_n\rho_0)\psi_{mn}(\phi,z) + H_z^{inc} + H_z^{c},$$

$$\sum_m\sum_n \frac{< E_\phi^{slot}, \psi_{mn}^*(\phi,z) > \kappa_n \psi_{mn}(\phi,z)}{-j\omega\mu_0 J'_{v_m}(\kappa_n\rho_0) H'^{(2)}_{v_m}(\kappa_n\rho_0)} \left\{ J_{v_m}(\kappa_n\rho_0) H'^{(2)}_{v_m}(\kappa_n\rho_0) - J'_{v_m}(\kappa_n\rho_0) H^{(2)}_{v_m}(\kappa_n\rho_0) \right\}$$
$$= -(H_z^{inc} + H_z^{c}),$$

$$\sum_m\sum_n Y_{mn} < E_\phi^{slot}, \psi_{mn}^*(\phi,z) > \psi_{mn}(\phi,z) = -(H_z^{inc} + H_z^{c}) \text{ on } \partial S, \tag{3.87}$$

where

$$Y_{mn} = \frac{2}{\omega\mu_0\pi\rho_0} \frac{1}{J'_{v_m}(\kappa_n\rho_0) H'^{(2)}_{v_m}(\kappa_n\rho_0)}. \tag{3.88}$$

In obtaining (3.87), the Wronskian relation given in (3.28) is used

To solve (3.87) the slot field is expanded into entire domain sinusoidal basis functions as in the previous section,

$$E_\phi^{slot} = \sum_{q=1}^{Q} \hat{c}_q f_q, \tag{3.89}$$

where

$$f_q = \sin\left\{\tfrac{q\pi}{l}(z + \tfrac{l}{2})\right\}, \tag{3.90}$$

and $\widehat{c}_q$ denote unknown expansion coefficients. When (3.90) is substituted into the equation (3.87) one gets

$$\sum_{q=1}^{Q} \widehat{c}_q \sum_m \sum_n Y_{mn} < f_q, \psi^*_{mn}(\phi, z) > \psi_{mn}(\phi, z) = -(H_z^{inc} + H_z^c) \text{ on } \partial S . \tag{3.91}$$

In accordance with the Galerkin's method, taking inner products of both sides of (3.91) with a basis functions f_p, a new equation is obtained

$$\sum_{q=1}^{Q} \widehat{c}_q \sum_m \sum_n Y_{mn} < f_q, \psi^*_{mn}(\phi, z) >< f_p, \psi_{mn}(\phi, z) > =< f_p, -(H_z^{inc} + H_z^c) > \text{ on } \partial S . \tag{3.92}$$

If this is performed for p=1, 2, . . ., Q, a new set of equations is obtained in matrix form

$$\begin{bmatrix} A_{11} & A_{12} & \cdots & \\ A_{21} & A_{22} & \cdots & \\ \vdots & \vdots & \ddots & \\ & & & A_{QQ} \end{bmatrix} \begin{bmatrix} \widehat{c}_1 \\ \widehat{c}_2 \\ \vdots \\ \widehat{c}_Q \end{bmatrix} = \begin{bmatrix} \widehat{B}_1 \\ \widehat{B}_2 \\ \vdots \\ \widehat{B}_Q \end{bmatrix}, \tag{3.93}$$

that can be solved by a matrix inversion, $[\widehat{c}_q] = [\widehat{A}_{pq}]^{-1}[\widehat{B}_p]$. The matrix elements are

$$\widehat{A}_{pq} = \sum_m \sum_n Y_{mn} < f_q, \psi^*_{mn}(\phi, z) >< f_p, \psi_{mn}(\phi, z) > = \frac{2}{\omega\mu_0\pi\rho_0} \sum_m \sum_n \frac{C^*_{nq} C_{np} S^2_{\nu_m}}{J'_{\nu_m}(\kappa_n\rho_0) H'^{(2)}_{\nu_m}(\kappa_n\rho_0)}, \tag{3.94}$$

$$\widehat{B}_p =< f_p, -(H_z^{inc} + H_z^c) >= a_{TE}^{inc} \frac{2\kappa_0}{\omega\mu_0\pi\rho_0} \frac{\sqrt{T_\phi T_z} S_{\nu_0} C_{0p}}{H'^{(2)}_{\nu_0}(\kappa_0\rho_0)} . \tag{3.95}$$

Here C_{np}, C^*_{nq}, and S_{ν_m} are given by (3.42)-(3.44).

As in the conducting strips problem considered in Section 3.2, numerical computations of the matrix elements have convergence difficulties. The convergence acceleration method discussed for the strips problem is also applicable to the slot problem of this Section. The asymptotic value of the products of Bessel functions [24] is

$$J'_{\nu_m}(\kappa_n\rho_0)H'^{(2)}_{\nu_m}(\kappa_n\rho_0) \cong \frac{-j|\nu_m|}{\pi(\kappa_n\rho_0)^2} \text{ as } |\nu_m| = |\nu_0 + 2\pi m/T_\phi| = |\nu_0 + mN| \to \infty . \quad (3.96)$$

It is therefore more convenient to write $\widehat{A}_{pq}$ as follows:

$$\begin{aligned}
\widehat{A}_{pq} &= \frac{2}{\omega\mu_0\pi\rho_0}\sum_m\sum_n \frac{C^*_{nq}C_{np}S^2_{\nu_m}}{J'_{\nu_m}(\kappa_n\rho_0)H'^{(2)}_{\nu_m}(\kappa_n\rho_0)} \\
&= \sum_{n=-\infty}^{\infty}\frac{2C^*_{nq}C_{np}}{\omega\mu_0\pi\rho_0}\sum_{m=-\infty}^{\infty}\frac{S^2_{\nu_m}}{J'_{\nu_m}(\kappa_n\rho_0)H'^{(2)}_{\nu_m}(\kappa_n\rho_0)} \\
&= \sum_{n=-\infty}^{\infty}\frac{2C^*_{nq}C_{np}}{\omega\mu_0\pi\rho_0}\left\{\sum_{m=-\infty}^{\infty}S^2_{\nu_m}\left(\frac{1}{J_{\nu_m}(\kappa_n\rho_0)H^{(2)}_{\nu_m}(\kappa_n\rho_0)} + \frac{\pi(\kappa_n\rho_0)^2}{j|\nu_m|}\right) - \sum_{m=-\infty}^{\infty}S^2_{\nu_m}\frac{\pi(\kappa_n\rho_0)^2}{j|\nu_m|}\right\} \\
&= \sum_{n=-\infty}^{\infty}\frac{2C^*_{nq}C_{np}}{\omega\mu_0\pi\rho_0}\left\{\sum_{m=-\infty}^{\infty}S^2_{\nu_m}\left(\frac{1}{J_{\nu_m}(\kappa_n\rho_0)H^{(2)}_{\nu_m}(\kappa_n\rho_0)} + \frac{\pi(\kappa_n\rho_0)^2}{j|\nu_m|}\right)\right\} \\
&\qquad - \widehat{I}\sum_{n=-\infty}^{\infty}\frac{2C^*_{nq}C_{np}}{\omega\mu_0\pi\rho_0}(\kappa_n\rho_0)^2 \text{ ,} \quad (3.97)
\end{aligned}$$

where

$$\widehat{I} = \frac{\pi}{j}\sum_{m=-\infty}^{\infty}\frac{S^2_{\nu_m}}{|\nu_m|} = -\pi^2 I . \quad (3.98)$$

Here *I* is given by (3.47) and it can be computed as described in Appendix A.

Once the matrix equation is solved for the coefficients $\widehat{c}_q$, the scattered electric and magnetic fields are determined easily. For the external region of the structure, the coefficients $a_{TE,0mn}$ are determined as follows

$$a_{TE,0mn} = \frac{< E^{slot}_\phi, \psi^*_{mn}(\phi,z) >}{\kappa_n H'^{(2)}_{\nu_m}(\kappa_n\rho_0)} = \frac{\sum_{q=1}^{Q}\widehat{c}_q < f_q, \psi^*_{mn}(\phi,z) >}{\kappa_n H'^{(2)}_{\nu_m}(\kappa_n\rho_0)} = \left\{\sum_{q=1}^{Q}\widehat{c}_q C^*_{nq}\right\}\frac{S_{\nu_m}}{\kappa_n H'^{(2)}_{\nu_m}(\kappa_n\rho_0)} . \quad (3.99)$$

Then the fields in (3.76)-(3.79), which are given for the external region become

$$H^s_{0\phi} = \frac{-1}{j\omega\mu_0\rho}\sum_m\sum_n\left\{\sum_{q=1}^{Q}\widehat{c}_q C^*_{nq}\right\}\frac{\nu_m\beta_n S_{\nu_m}}{\kappa_n H'^{(2)}_{\nu_m}(\kappa_n\rho_0)}H^{(2)}_{\nu_m}(\kappa_n\rho)\psi_{mn}(\phi,z) , \quad (3.100)$$

$$H_{0z}^{s} = \frac{1}{j\omega\mu_0}\sum_{m}\sum_{n}\left\{\sum_{q=1}^{Q}\widehat{c}_q C_{nq}^{*}\right\}\frac{\kappa_n S_{\nu_m}}{H_{\nu_m}'^{(2)}(\kappa_n\rho_0)}H_{\nu_m}^{(2)}(\kappa_n\rho)\psi_{mn}(\phi,z), \qquad (3.101)$$

$$E_{0\phi}^{s}(\rho,\phi,z) = \sum_{m}\sum_{n}\left\{\sum_{q=1}^{Q}\widehat{c}_q C_{nq}^{*}\right\}\frac{S_{\nu_m}}{H_{\nu_m}'^{(2)}(\kappa_n\rho_0)}H_{\nu_m}'^{(2)}(\kappa_n\rho)\psi_{mn}(\phi,z), \qquad (3.102)$$

$$E_{0z}^{s}(\rho,\phi,z) = 0\,. \qquad (3.103)$$

As before, the scattered fields are determined separately for each cylindrical wave components of the incident plane wave. The RCS of the surface is determined from (2.76);

$$RCS = \lim_{\rho\to\infty} 2\pi\rho\frac{\left|\sum_{\nu_0=-\infty}^{\infty}\left\{\mathbf{E}^{c}(\rho,\phi,z)+\mathbf{E}^{s}(\rho,\phi,z)\right\}\right|^{2}}{\left|\mathbf{E}^{i}\right|^{2}}, \qquad (3.104)$$

where $\mathbf{E}^{s}$ refers to the scattered electric fields given in (3.102), $\mathbf{E}^{c}$ refers to the electric fields corresponding to (3.84), and $\mathbf{E}^{i}$ refers to the electric field of the incident wave. According to Section 2.2 of Chapter 2, the absolute value of a unit amplitude TE plane wave is

$$\left|\mathbf{E}^{i}\right| = \kappa_0 = k_0\sin\theta^{inc}\,. \qquad (3.105)$$

In the far field region, the scattered electric fields that are due to the magnetic currents are determined from the expression (3.102) using the asymptotic form of the Hankel functions in (2.75)

$$\begin{aligned}\mathbf{E}^{s}(\rho,\phi,z) &= \mathbf{a}_z\sum_{m}\sum_{n}\left\{\sum_{q=1}^{Q}\widehat{c}_q C_{nq}^{*}\right\}\frac{S_{\nu_m}}{H_{\nu_m}'^{(2)}(\kappa_n\rho_0)}H_{\nu_m}'^{(2)}(\kappa_n\rho)\psi_{mn}(\phi,z)\\ &= \mathbf{a}_z\sum_{m}\sum_{n}\left\{\sum_{q=1}^{Q}\widehat{c}_q C_{nq}^{*}\right\}\frac{S_{\nu_m}}{H_{\nu_m}'^{(2)}(\kappa_n\rho_0)}(-j)\sqrt{\frac{2}{\pi\kappa_n\rho}}e^{j\pi/4+j\nu_m\pi/2}e^{-j\kappa_n\rho}\frac{e^{-j\nu_m\phi}e^{-j\beta_n z}}{\sqrt{T_\phi T_z}}\\ &= \mathbf{a}_z e^{-j\pi/4}\sqrt{\frac{2}{\pi\rho}}\sum_{m}\sum_{n}\left\{\sum_{q=1}^{Q}\widehat{c}_q C_{nq}^{*}\right\}\frac{S_{\nu_m}e^{-j\kappa_n\rho-j\nu_m(\phi-\pi/2)-j\beta_n z}}{\sqrt{T_\phi T_z}\sqrt{\kappa_n}H_{\nu_m}'^{(2)}(\kappa_n\rho_0)} \quad \text{as } \rho\to\infty. \qquad (3.106)\end{aligned}$$

Similarly, the electric fields $\mathbf{E}^{c}$ that are scattered from the conducting cylinder when the slots were not present are determined from the expression (3.85) using the asymptotic form of the Hankel functions in (2.75), that is

$$\mathbf{E}^{c}(\rho,\phi,z) = \mathbf{a}_z\kappa_0 a_{TE}^{c}H_{\nu_0}'^{(2)}(\kappa_0\rho_0)e^{-j\nu_0\phi}e^{-j\beta_0 z}$$

$$
\begin{aligned}
&= \mathbf{a}_z a_{TE}^{inc} \frac{\kappa_0 J'_{v_0}(\kappa_0 \rho_0)}{H'^{(2)}_{v_0}(\kappa_0 \rho_0)} H'^{(2)}_{v_0}(\kappa_0 \rho) e^{-jv_0\phi} e^{-j\beta_0 z} \\
&= \mathbf{a}_z a_{TE}^{inc} \frac{\kappa_0 J'_{v_0}(\kappa_0 \rho_0)}{H'^{(2)}_{v_0}(\kappa_0 \rho_0)} (-j) \sqrt{\frac{2}{\pi \kappa_0 \rho}} e^{j\pi/4 + jv_0\pi/2} e^{-j\kappa_0 \rho} e^{-jv_0\phi} e^{-j\beta_0 z} \\
&= \mathbf{a}_z e^{-j\pi/4} \sqrt{\frac{2}{\pi \rho}} \frac{a_{TE}^{inc} \sqrt{\kappa_0} J'_{v_0}(\kappa_0 \rho_0)}{H'^{(2)}_{v_0}(\kappa_0 \rho_0)} e^{-j\kappa_0\rho - jv_0(\phi - \pi/2) - j\beta_0 z} \text{ as } \rho \to \infty. \qquad (3.107)
\end{aligned}
$$

The RCS of the cylindrical structure can be determined by using the far field region expressions of the scattered electric fields established in (3.106) and (3.107) in (3.104). That is,

$$
\begin{aligned}
RCS = \frac{4}{k_0 \sin\theta^{inc}} \Bigg| \sum_{v_0=-\infty}^{\infty} \Bigg\{ & \frac{a_{TE}^{inc} \sqrt{\kappa_0} J'_{v_0}(\kappa_0 \rho_0)}{H'^{(2)}_{v_0}(\kappa_0 \rho_0)} e^{-j\kappa_0\rho - jv_0(\phi - \pi/2) - j\beta_0 z} \\
& - \sum_m \sum_n \left\{ \sum_{q=1}^{Q} \hat{c}_q C^*_{nq} \right\} \frac{S_{v_m} e^{-j\kappa_n\rho - jv_m(\phi - \pi/2) - j\beta_n z}}{\sqrt{T_\phi T_z} \sqrt{\kappa_n} H'^{(2)}_{v_m}(\kappa_n \rho_0)} \Bigg\} \Bigg|^2 .(3.108)
\end{aligned}
$$

Electromagnetic field penetrations into the conducting cylinders perforated with the slots have also important consequences in antenna applications. The amount of penetration is measured by a quantity that is called as “the coupling”. The coupling is defined as the total power measured at the center of a cylindrical structure when a plane wave is incident on the structure. As discussed in section 2.3, it can be determined by considering the far fields radiated from a magnetic type line current located at the center of the cylindrical structure. The definition of the coupling is

$$
Coupling = \lim_{\rho \to \infty} \frac{\left| E^s_{0\phi} \right|^2}{\left| E^{inc}_{\phi} \right|^2}, \qquad (3.109)
$$

where E^s denotes the scattered electric field in the far field region (as $\rho \to \infty$); E^{inc} denote the electric field radiated from a magnetic type line current located at the center of the cylindrical structure, and is given by (2.101). As $\rho \to \infty$, the limiting value of the expression for E^{inc} is obtained as

$$
\begin{aligned}
E^{inc}_{\phi} &= a_{TE}^{inc} \kappa_0 H'^{(2)}_0(\kappa_0 \rho) e^{-j\beta_0 z} \cong a_{TE}^{inc} \kappa_0 (-j) \sqrt{\frac{2}{\pi \kappa_0 \rho}} e^{j\pi/4} e^{-j\kappa_0 \rho} e^{-j\beta_0 z} \\
&\cong -j a_{TE}^{inc} \sqrt{\frac{2\kappa_0}{\pi \rho}} e^{j\pi/4} e^{-j\kappa_0 \rho} e^{-j\beta_0 z} \text{ as } \rho \to \infty. \qquad (3.110)
\end{aligned}
$$

4. SCATTERING FROM A CYLINDRICAL SURFACE CONTAINING A DIELECTRIC SHELL

A cylindrical structure consisting of a dielectric shell covered periodically with conducting patches is analyzed by considering the TE and TM modes simultaneously. When formulating the problem, the scattered waves are written as infinite sums of the Floquet modes with unknown weighting coefficients. The weighting coefficients are then related to the surface currents of the conducting patches by using boundary conditions of the problem. Later on, an integral equation is obtained for the surface currents and solved numerically by using MM techniques. The formulation technique given in this Chapter can be extended to multiple dielectric layer problems.

As in the problems considered in the previous chapters, the infinite sums appearing in this chapter are found to be slowly convergent. When solving the problem by a MM technique, the infinite sums should be handled properly in order to circumvent slow convergence difficulties. One approach in such a case is to use sub-domain basis functions in conjunction with a conjugate gradient fast Fourier transform method as in [10]. Another approach is to use entire-domain basis functions together with a convergence acceleration method as described by us in [18, 21] which is based on a Kummer's series acceleration method. Here, we followed the same approach and derived the appropriate convergence acceleration method for the problem.

4.1. The scattered waves from a dielectric shell covered by conducting strips

A periodic cylindrical structure consisting of conducting patches printed on a dielectric shell is shown in Figure 4.1. The scattered waves in three different regions are illustrated in Figure 4.2. The strips are periodically located on a surface at $\rho = \rho_0$ with periodicities T_ϕ and T_z in the directions ϕ and z. When a plane wave is incident on the structure, the incident wave can be decomposed into cylindrical waves as described in Section 2.2. If the incident plane wave has unit amplitude vector potential and its polarization is TM, the cylindrical wave components are given by

$$\begin{pmatrix} A_{TM}^{inc} \\ A_{TE}^{inc} \end{pmatrix} = \begin{pmatrix} a_{TM}^{inc} \\ a_{TE}^{inc} \end{pmatrix} J_{v_0}(\kappa_{00}\rho) e^{-jv_0\phi} e^{-j\beta_0 z}, \tag{4.1}$$

where

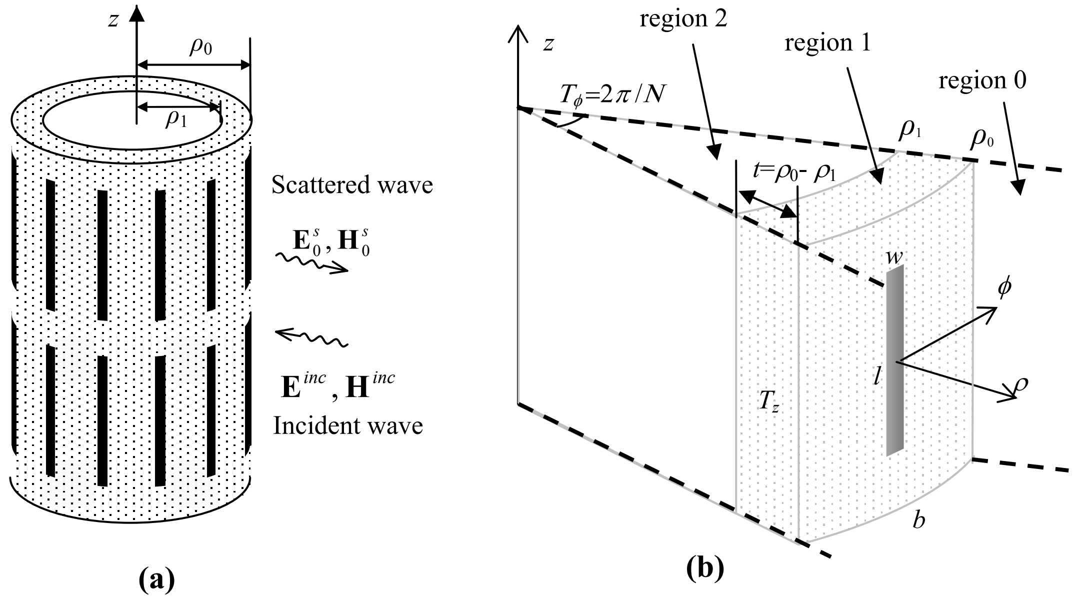

Figure 4.1. **a)** A periodic cylindrical structure consisting of rectangular strips on the surface of a dielectric shell. A cylindrical wave is incident on the structure **(b)** A unit cell at ϕ=0, showing the parameters of the problem. N denotes the number of periodic strips in ϕ direction.

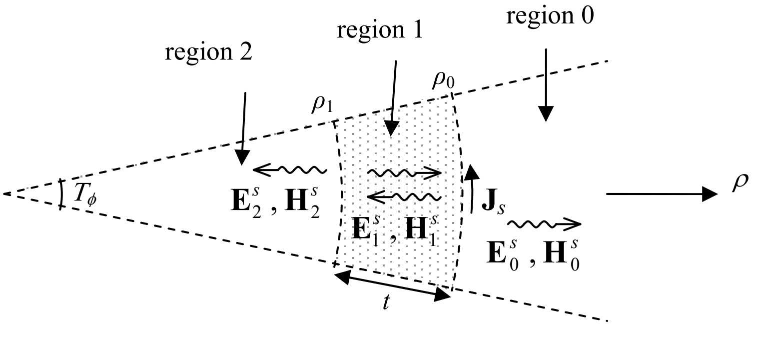

Figure 4.2. The top view of the unit cell of the problem. Scattered waves in regions 0, 1, and 2 are radiated by a current, $\mathbf{J}_s$, which is induced due to the incident wave.

$$\begin{pmatrix} a_{TM}^{inc} \\ a_{TE}^{inc} \end{pmatrix} = \begin{pmatrix} 1 \\ 0 \end{pmatrix} e^{jv_0(\phi^{inc}-\pi/2)}. \tag{4.2}$$

$$\beta_0 = k_0 \cos\theta^{inc}, \tag{4.3}$$

$$\kappa_{00} = k_0 \sin\theta^{inc}, \tag{4.4}$$

v_0 denotes an integer, θ^{inc} and ϕ^{inc} denote propagation directions of the incident wave. Such an excitation induces a surface current, $\mathbf{J}_s$, on a patch surface as seen in the unit cell of the problem. In turn, those currents radiate the scattered waves. In accordance with the Floquet Theorem described in Chapter 2, the scattered waves are represented as infinite sums of the Floquet modes. The scattered waves involve TM and TE modes simultaneously, and they can be derived from vector potentials A_{TM} and A_{TE}. According to the conventions discussed in Chapter 2, the appropriate expressions for the three distinct regions are

$$A_{TM,0}^{s} = \sum_m \sum_n a_{TM,0mn} H_{v_m}^{(2)}(\kappa_{0n}\rho)\psi_{mn}(\phi,z) \text{ in region 0,} \tag{4.5}$$

$$A_{TE,0}^{s} = \sum_m \sum_n a_{TE,0mn} H_{v_m}^{(2)}(\kappa_{0n}\rho)\psi_{mn}(\phi,z) \text{ in region 0,} \tag{4.6}$$

$$A_{TM,1}^{s} = \sum_m \sum_n \left\{ a_{TM,1mn}^{-} J_{v_m}(\kappa_{1n}\rho) + a_{TM,1mn}^{+} Y_{v_m}(\kappa_{1n}\rho) \right\} \psi_{mn}(\phi,z) \text{ in region 1,} \tag{4.7}$$

$$A_{TE,1}^{s} = \sum_m \sum_n \left\{ a_{TE,1mn}^{-} J_{v_m}(\kappa_{1n}\rho) + a_{TE,1mn}^{+} Y_{v_m}(\kappa_{1n}\rho) \right\} \psi_{mn}(\phi,z) \text{ in region 1,} \tag{4.8}$$

$$A_{TM,2}^{s} = \sum_m \sum_n a_{TM,2mn} J_{v_m}(\kappa_{2n}\rho)\psi_{mn}(\phi,z) \text{ in region 2,} \tag{4.9}$$

$$A_{TE,2}^{s} = \sum_m \sum_n a_{TE,2mn} J_{v_m}(\kappa_{2n}\rho)\psi_{mn}(\phi,z) \text{ in region 2,} \tag{4.10}$$

where J_{v_m}, Y_{v_m}, and $H_{v_m}^{(2)}$ denote the cylindrical Bessel functions of order v_m. The weighting coefficients $a_{TM,imn}$ and $a_{TE,imn}$ denote the unknowns to be determined from boundary conditions. The Floquet modes denoted by ψ_{mn} are given in Chapter 2,

$$\psi_{mn}(\phi, z) = \frac{e^{-jv_m\phi}e^{-j\beta_n z}}{\sqrt{T_\phi T_z}}, \tag{4.11}$$

$$\beta_n = \beta_0 + 2\pi n / T_z, \tag{4.12}$$

$$v_m = v_0 + 2\pi m / T_\phi, \tag{4.13}$$

$$\kappa_{in} = \sqrt{k_i^2 - \beta_n^2}. \tag{4.14}$$

Here v_0 and β_0 denote the phase constants of the exciting wave in (4.1) and $k_i = \omega\sqrt{\mu_0 \varepsilon_i}$ denotes the wave-number of *i-th* region. Since purely standing waves exist in the innermost region of the cylindrical structure (region 2), Bessel functions of the first kind J_{v_m} are used in the relevant expressions. For the external region, the waves should be propagating in $+\rho$ direction and so Hankel functions of the second kind $H_{v_m}^{(2)}$ are used in the expressions. However, the waves in the dielectric shell region are represented by using the functions J_{v_m} and Y_{v_m} because there should exist forward and backward traveling waves in that region. It is shown in Appendix C that the functions J_{v_m} and Y_{v_m} exhibit oscillatory behavior, as do the sinusoidal functions [22]. Hence, the waves in the dielectric shell are represented by cylindrical standing waves.

If there is no current at an interface, boundary conditions require that the tangential components of electric and magnetic fields should be continuous. Otherwise the fields should be discontinuous by amounts equal to the magnitudes of the surface currents. Consider the boundary at $\rho = \rho_1$ as shown in Figure 4.2. Since there is no current at the boundary, the tangential components of the electric and magnetic fields should be continuous

$$E_{2z}^s(\rho_1) = E_{1z}^s(\rho_1), \tag{4.15}$$

$$E_{2\phi}^s(\rho_1) = E_{1\phi}^s(\rho_1), \tag{4.16}$$

$$H_{2\phi}^s(\rho_1) = H_{1\phi}^s(\rho_1), \tag{4.17}$$

$$H_{2z}^s(\rho_1) = H_{1z}^s(\rho_1). \tag{4.18}$$

On the other hand, there exists a surface current $\mathbf{J}_s$ at the boundary $\rho = \rho_0$ and so

$$E_{1z}^s(\rho_0) = E_{0z}^s(\rho_0), \tag{4.19}$$

$$E_{1\phi}^s(\rho_0) = E_{0\phi}^s(\rho_0), \tag{4.20}$$

$$H_{1\phi}^s(\rho_0) = -J_z + H_{0\phi}^s(\rho_0), \tag{4.21}$$

$$H_{1z}^s(\rho_0) = J_\phi + H_{0z}^s(\rho_0), \tag{4.22}$$

where J_ϕ and J_z denote the components of the surface current $\mathbf{J}_s$, that is,

$$\mathbf{J}_s = \mathbf{a}_\phi J_\phi + \mathbf{a}_z J_z . \tag{4.23}$$

The electric and magnetic fields can be obtained from the vector potentials A_{TM} and A_{TE} as discussed in Chapter 2. To simplify the application of the boundary conditions, we use matrix representations for the tangential components of electric and magnetic fields. The expressions for distinct regions are written as follows

$$\begin{pmatrix} E_{0\phi}^s(\rho,\phi,z) \\ E_{0z}^s(\rho,\phi,z) \end{pmatrix} = \sum_m \sum_n e_{0mn}(\rho) \begin{pmatrix} a_{TM,0mn} \\ a_{TE,0mn} \end{pmatrix} \psi_{mn}(\phi,z) \text{ for region 0,} \tag{4.24}$$

$$\begin{pmatrix} H_{0z}^s(\rho,\phi,z) \\ -H_{0\phi}^s(\rho,\phi,z) \end{pmatrix} = \sum_m \sum_n h_{0mn}(\rho) \begin{pmatrix} a_{TM,0mn} \\ a_{TE,0mn} \end{pmatrix} \psi_{mn}(\phi,z) \text{ for region 0,} \tag{4.25}$$

$$\begin{pmatrix} E_{1\phi}^s(\rho,\phi,z) \\ E_{1z}^s(\rho,\phi,z) \end{pmatrix} = \sum_m \sum_n \left\{ e_{1mn}^-(\rho) \begin{pmatrix} a_{TM,1mn}^- \\ a_{TE,1mn}^- \end{pmatrix} + e_{1mn}^+(\rho) \begin{pmatrix} a_{TM,1mn}^+ \\ a_{TE,1mn}^+ \end{pmatrix} \right\} \psi_{mn}(\phi,z) \text{ for region 1,} \tag{4.26}$$

$$\begin{pmatrix} H_{1z}^s(\rho,\phi,z) \\ -H_{1\phi}^s(\rho,\phi,z) \end{pmatrix} = \sum_m \sum_n \left\{ h_{1mn}^-(\rho) \begin{pmatrix} a_{TM,1mn}^- \\ a_{TE,1mn}^- \end{pmatrix} + h_{1mn}^+(\rho) \begin{pmatrix} a_{TM,1mn}^+ \\ a_{TE,1mn}^+ \end{pmatrix} \right\} \psi_{mn}(\phi,z) \text{ for region 1,} \tag{4.27}$$

$$\begin{pmatrix} E_{2\phi}^s(\rho,\phi,z) \\ E_{2z}^s(\rho,\phi,z) \end{pmatrix} = \sum_m \sum_n e_{2mn}(\rho) \begin{pmatrix} a_{TM,2mn} \\ a_{TE,2mn} \end{pmatrix} \psi_{mn}(\phi,z) \text{ for region 2,} \tag{4.28}$$

$$\begin{pmatrix} H^{s}_{2z}(\rho,\phi,z) \\ -H^{s}_{2\phi}(\rho,\phi,z) \end{pmatrix} = \sum_{m}\sum_{n} h_{2mn}(\rho) \begin{pmatrix} a_{TM,2mn} \\ a_{TE,2mn} \end{pmatrix} \psi_{mn}(\phi,z) \text{ for region 2,} \tag{4.29}$$

where *e* and *h* stand for 2x2 square matrices that are obtained from the expressions given in (2.45)-(2.48) as;

$$e_{0mn}(\rho) = \frac{1}{j\omega\varepsilon_{0}\rho} \begin{bmatrix} -\nu_{m}\beta_{n}H^{(2)}_{\nu_{m}}(\kappa_{0n}\rho) & j\omega\varepsilon_{0}\rho\kappa_{0n}H'^{(2)}_{\nu_{m}}(\kappa_{0n}\rho) \\ \kappa^{2}_{0n}\rho H^{(2)}_{\nu_{m}}(\kappa_{0n}\rho) & 0 \end{bmatrix}, \tag{4.30}$$

$$h_{0mn}(\rho) = \frac{1}{j\omega\mu_{0}\rho} \begin{bmatrix} 0 & \kappa^{2}_{0n}\rho H^{(2)}_{\nu_{m}}(\kappa_{0n}\rho) \\ j\omega\mu_{0}\rho\kappa_{0n}H'^{(2)}_{\nu_{m}}(\kappa_{0n}\rho) & \nu_{m}\beta_{n}H^{(2)}_{\nu_{m}}(\kappa_{0n}\rho) \end{bmatrix}, \tag{4.31}$$

$$e^{-}_{1mn}(\rho) = \frac{1}{j\omega\varepsilon_{1}\rho} \begin{bmatrix} -\nu_{m}\beta_{n}J_{\nu_{m}}(\kappa_{1n}\rho) & j\omega\varepsilon_{1}\rho\kappa_{1n}J'_{\nu_{m}}(\kappa_{1n}\rho) \\ \kappa^{2}_{1n}\rho J_{\nu_{m}}(\kappa_{1n}\rho) & 0 \end{bmatrix}, \tag{4.32}$$

$$h^{-}_{1mn}(\rho) = \frac{1}{j\omega\mu_{0}\rho} \begin{bmatrix} 0 & \kappa^{2}_{1n}\rho J_{\nu_{m}}(\kappa_{1n}\rho) \\ j\omega\mu_{0}\rho\kappa_{1n}J'_{\nu_{m}}(\kappa_{1n}\rho) & \nu_{m}\beta_{n}J_{\nu_{m}}(\kappa_{1n}\rho) \end{bmatrix}, \tag{4.33}$$

$$e^{+}_{1mn}(\rho) = \frac{1}{j\omega\varepsilon_{1}\rho} \begin{bmatrix} -\nu_{m}\beta_{n}Y_{\nu_{m}}(\kappa_{1n}\rho) & j\omega\varepsilon_{1}\rho\kappa_{1n}Y'_{\nu_{m}}(\kappa_{1n}\rho) \\ \kappa^{2}_{1n}\rho Y_{\nu_{m}}(\kappa_{1n}\rho) & 0 \end{bmatrix}, \tag{4.34}$$

$$h^{+}_{1mn}(\rho) = \frac{1}{j\omega\mu_{0}\rho} \begin{bmatrix} 0 & \kappa^{2}_{1n}\rho Y_{\nu_{m}}(\kappa_{1n}\rho) \\ j\omega\mu_{0}\rho\kappa_{1n}Y'_{\nu_{m}}(\kappa_{1n}\rho) & \nu_{m}\beta_{n}Y_{\nu_{m}}(\kappa_{1n}\rho) \end{bmatrix}, \tag{4.35}$$

$$e_{2mn}(\rho) = \frac{1}{j\omega\varepsilon_{0}\rho} \begin{bmatrix} -\nu_{m}\beta_{n}J_{\nu_{m}}(\kappa_{2n}\rho) & j\omega\varepsilon_{0}\rho\kappa_{2n}J'_{\nu_{m}}(\kappa_{2n}\rho) \\ \kappa^{2}_{2n}\rho J_{\nu_{m}}(\kappa_{2n}\rho) & 0 \end{bmatrix}, \tag{4.36}$$

$$h_{2mn}(\rho) = \frac{1}{j\omega\mu_{0}\rho} \begin{bmatrix} 0 & \kappa^{2}_{2n}\rho J_{\nu_{m}}(\kappa_{2n}\rho) \\ j\omega\mu_{0}\rho\kappa_{2n}J'_{\nu_{m}}(\kappa_{2n}\rho) & \nu_{m}\beta_{n}J_{\nu_{m}}(\kappa_{2n}\rho) \end{bmatrix}, \tag{4.37}$$

and a prime over a Bessel function implies the derivative of that function with respect to the argument, that is

$$R'(\kappa\rho) = \frac{\partial R(\kappa\rho)}{\partial(\kappa\rho)}. \tag{4.38}$$

By using the matrix representations for the electric and magnetic fields, the boundary conditions in (4.15)-(4.22) are expressed as

$$\sum_m\sum_n e_{2mn}(\rho_1)\begin{pmatrix} a_{TM,2mn}\\ a_{TE,2mn}\end{pmatrix}\psi_{mn}(\phi,z) = \sum_m\sum_n e^-_{1mn}(\rho_1)\begin{pmatrix} a^-_{TM,1mn}\\ a^-_{TE,1mn}\end{pmatrix}\psi_{mn}(\phi,z)+\sum_m\sum_n e^+_{1mn}(\rho_1)\begin{pmatrix} a^+_{TM,1mn}\\ a^+_{TE,1mn}\end{pmatrix}\psi_{mn}(\phi,z)\,, \tag{4.39}$$

$$\sum_m\sum_n h_{2mn}(\rho_1)\begin{pmatrix} a_{TM,2mn}\\ a_{TE,2mn}\end{pmatrix}\psi_{mn}(\phi,z) = \sum_m\sum_n h^-_{1mn}(\rho_1)\begin{pmatrix} a^-_{TM,1mn}\\ a^-_{TE,1mn}\end{pmatrix}\psi_{mn}(\phi,z)+\sum_m\sum_n h^+_{1mn}(\rho_1)\begin{pmatrix} a^+_{TM,1mn}\\ a^+_{TE,1mn}\end{pmatrix}\psi_{mn}(\phi,z)\,, \tag{4.40}$$

$$\sum_m\sum_n e^-_{1mn}(\rho_0)\begin{pmatrix} a^-_{TM,1mn}\\ a^-_{TE,1mn}\end{pmatrix}\psi_{mn}(\phi,z)+\sum_m\sum_n e^+_{1mn}(\rho_0)\begin{pmatrix} a^+_{TM,1mn}\\ a^+_{TE,1mn}\end{pmatrix}\psi_{mn}(\phi,z) = \sum_m\sum_n e_{0mn}(\rho_0)\begin{pmatrix} a_{TM,0mn}\\ a_{TE,0mn}\end{pmatrix}\psi_{mn}(\phi,z)\,, \tag{4.41}$$

$$\sum_m\sum_n h^-_{1mn}(\rho_0)\begin{pmatrix} a^-_{TM,1mn}\\ a^-_{TE,1mn}\end{pmatrix}\psi_{mn}(\phi,z)+\sum_m\sum_n h^+_{1mn}(\rho_0)\begin{pmatrix} a^+_{TM,1mn}\\ a^+_{TE,1mn}\end{pmatrix}\psi_{mn}(\phi,z) = \begin{pmatrix} J_\phi\\ J_z\end{pmatrix}+\sum_m\sum_n h_{0mn}(\rho_0)\begin{pmatrix} a_{TM,0mn}\\ a_{TE,0mn}\end{pmatrix}\psi_{mn}(\phi,z)\,. \tag{4.42}$$

An inner product for the Floquet modes is defined in (2.49) and it was shown in Chapter 2 that the modes $\psi_{mn}(\phi,z)$ are orthogonal to each other. Taking the inner products of both sides of equations (4.39)-. (4.42) with the Floquet modes one obtains:

$$e_{2mn}(\rho_1)\begin{pmatrix} a_{TM,2mn}\\ a_{TE,2mn}\end{pmatrix} = e^-_{1mn}(\rho_1)\begin{pmatrix} a^-_{TM,1mn}\\ a^-_{TE,1mn}\end{pmatrix}+e^+_{1mn}(\rho_1)\begin{pmatrix} a^+_{TM,1mn}\\ a^+_{TE,1mn}\end{pmatrix}, \tag{4.43}$$

$$h_{2mn}(\rho_1)\begin{pmatrix} a_{TM,2mn}\\ a_{TE,2mn}\end{pmatrix} = h^-_{1mn}(\rho_1)\begin{pmatrix} a^-_{TM,1mn}\\ a^-_{TE,1mn}\end{pmatrix}+h^+_{1mn}(\rho_1)\begin{pmatrix} a^+_{TM,1mn}\\ a^+_{TE,1mn}\end{pmatrix}, \tag{4.44}$$

$$e^-_{1mn}(\rho_0)\begin{pmatrix} a^-_{TM,1mn}\\ a^-_{TE,1mn}\end{pmatrix}+e^+_{1mn}(\rho_0)\begin{pmatrix} a^+_{TM,1mn}\\ a^+_{TE,1mn}\end{pmatrix} = e_{0mn}(\rho_0)\begin{pmatrix} a_{TM,0mn}\\ a_{TE,0mn}\end{pmatrix}, \tag{4.45}$$

$$h^-_{1mn}(\rho_0)\begin{pmatrix} a^-_{TM,1mn}\\ a^-_{TE,1mn}\end{pmatrix}+h^+_{1mn}(\rho_0)\begin{pmatrix} a^+_{TM,1mn}\\ a^+_{TE,1mn}\end{pmatrix} = h_{0mn}(\rho_0)\begin{pmatrix} a_{TM,0mn}\\ a_{TE,0mn}\end{pmatrix}+\begin{pmatrix} \left\langle J_\phi,\psi^*_{mn}(\phi,z)\right\rangle\\ \left\langle J_z,\psi^*_{mn}(\phi,z)\right\rangle\end{pmatrix}, \tag{4.46}$$

where the brackets “<>” represent the inner products, that is,

$$\begin{pmatrix} \langle J_\phi, \psi^*_{mn}(\phi,z) \rangle \\ \langle J_z, \psi^*_{mn}(\phi,z) \rangle \end{pmatrix} = \int_{-T_z/2}^{T_z/2} \int_{-T_\phi/2}^{T_\phi/2} \begin{pmatrix} J_\phi \psi^*_{mn}(\phi,z) \\ J_z \psi^*_{mn}(\phi,z) \end{pmatrix} d\phi dz\,. \tag{4.47}$$

Next, the unknown coefficients $a_{TM,0mn}$ and $a_{TE,0mn}$ of the scattered waves are expressed in terms of the surface currents by solving the set of equations algebraically. For example, the unknowns $a_{TM,2mn}$ and $a_{TE,2mn}$ can be eliminated from the equations (4.43)-(4.46) by writing

$$\begin{pmatrix} a_{TM,2mn} \\ a_{TE,2mn} \end{pmatrix} = [e_{2mn}(\rho_1)]^{-1} e^-_{1mn}(\rho_1) \begin{pmatrix} a^-_{TM,1mn} \\ a^-_{TE,1mn} \end{pmatrix} + [e_{2mn}(\rho_1)]^{-1} e^+_{1mn}(\rho_1) \begin{pmatrix} a^+_{TM,1mn} \\ a^+_{TE,1mn} \end{pmatrix}, \tag{4.48}$$

and similarly remaining unknowns can be eliminated. The solution for $a_{TM,0mn}$ and $a_{TE,0mn}$ can be written in the matrix form:

$$\begin{pmatrix} a_{TM,0mn} \\ a_{TE,0mn} \end{pmatrix} = [e_{0mn}(\rho_0)]^{-1} Z_Q \begin{pmatrix} \langle J_\phi, \psi^*_{mn}(\phi,z) \rangle \\ \langle J_z, \psi^*_{mn}(\phi,z) \rangle \end{pmatrix}, \tag{4.49}$$

where

$$Z_Q = \begin{bmatrix} Z_{\phi\phi} & Z_{\phi z} \\ Z_{z\phi} & Z_{zz} \end{bmatrix} = \left\{ Y_{0mn} - h_{0mn}(\rho_0)[e_{0mn}(\rho_0)]^{-1} \right\}^{-1}, \tag{4.50}$$

$$Y_{0mn} = \left\{ h^-_{1mn}(\rho_0)[e^-_{1mn}(\rho_0)]^{-1} + h^+_{1mn}(\rho_0)[e^+_{1mn}(\rho_0)]^{-1} \zeta_{0mn} \right\} \left\{ I_{2\times2} + \zeta_{0mn} \right\}^{-1}, \tag{4.51}$$

$$\zeta_{0mn} = e^+_{1mn}(\rho_0)[e^+_{1mn}(\rho_1)]^{-1} \zeta_{1mn} e^-_{1mn}(\rho_1)[e^-_{1mn}(\rho_0)]^{-1}, \tag{4.52}$$

$$\zeta_{1mn} = \left\{ h^+_{1mn}(\rho_1)[e^+_{1mn}(\rho_1)]^{-1} - h_{2mn}(\rho_1)[e_{2mn}(\rho_1)]^{-1} \right\}^{-1} \left\{ h_{2mn}(\rho_1)[e_{2mn}(\rho_1)]^{-1} - h^-_{1mn}(\rho_1)[e^-_{1mn}(\rho_1)]^{-1} \right\}. \tag{4.53}$$

Here $I_{2\times2}$ denotes an identity matrix,

$$I_{2\times2} = \begin{bmatrix} 1 & 0 \\ 0 & 1 \end{bmatrix}. \tag{4.54}$$

However, the surface currents J_ϕ and J_z appearing in (4.49) are still unknown quantities. To determine these quantities we equate total tangential electric field on a strip to zero, as described in the next section. This will allow us to express the surface current density in terms of the incident wave.

4.2. An integral equation for the surface currents

An integral equation for the problem can be obtained from the requirement that the total tangential electric field should be zero across a conducting patch surface. This condition has already been applied to the problems of the previous chapters, where there was no dielectric shell. For the problem of this chapter, the requirement can be expressed as

$$\begin{pmatrix} E_{\phi}^{inc}(\rho_0,\phi,z) \\ E_{z}^{inc}(\rho_0,\phi,z) \end{pmatrix} + \begin{pmatrix} E_{0\phi}^{c}(\rho_0,\phi,z) \\ E_{0z}^{c}(\rho_0,\phi,z) \end{pmatrix} + \begin{pmatrix} E_{0\phi}^{s}(\rho_0,\phi,z) \\ E_{0z}^{s}(\rho_0,\phi,z) \end{pmatrix} = 0 \text{ on } \partial s, \qquad (4.55)$$

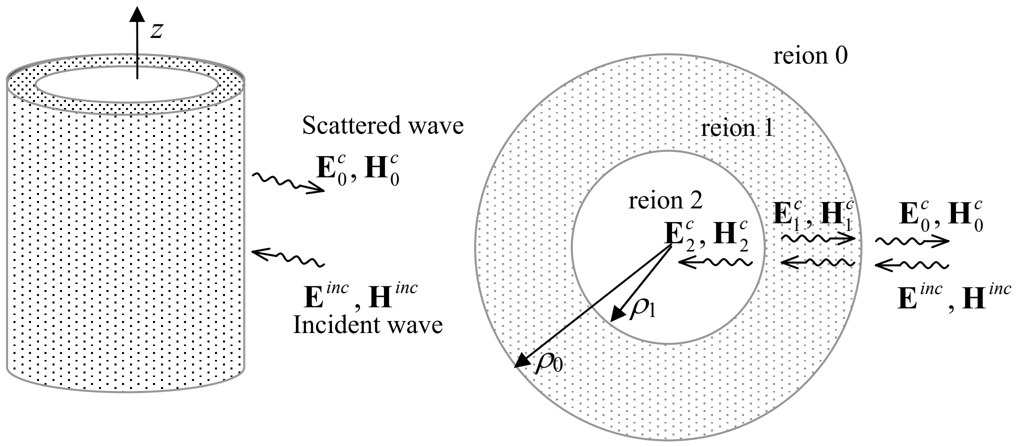

(a) **(b)**

Figure 4.3. (a) The incident and scattered waves when the conducting strips were not present in Figure 4.2. (**b)** Top view of the problem showing three different regions.

where ∂s refers to the surface of the conducting patch. Here $\mathbf{E}_0^s$ denotes the electric fields scattered by the conducting patches, $\mathbf{E}_0^c$ denotes the fields that would be scattered if the conducting patches were not present, and $\mathbf{E}^{inc}$ denotes the exciting electric field.

Initially, $\mathbf{E}_0^c$ is determined by using appropriate expressions for TM and TE waves in absence of the conducting patches. Assume a cylindrical wave $\mathbf{E}^{inc}$ is incident on the cylindrical structure shown in Figure 4.3.a. Referring to three different regions seen in Figure 4.3.b, the scattered TM and TE waves may be derived from vector potentials:

$$A_{TM,0}^{c} = a_{TM,000}^{c} H_{\nu_0}^{(2)}(\kappa_{00}\rho) e^{-j\nu_0\phi} e^{-j\beta_0 z} \text{ in region 0,} \tag{4.56}$$

$$A_{TE,0}^{c} = a_{TE,000}^{c} H_{\nu_0}^{(2)}(\kappa_{00}\rho) e^{-j\nu_0\phi} e^{-j\beta_0 z} \text{ in region 0,} \tag{4.57}$$

$$A_{TM,1}^{c} = a_{TM,100}^{c-} J_{\nu_0}(\kappa_{10}\rho) e^{-j\nu_0\phi} e^{-j\beta_0 z} + a_{TM,100}^{c+} Y_{\nu_0}(\kappa_{10}\rho) e^{-j\nu_0\phi} e^{-j\beta_0 z} \text{ in region 1,} \tag{4.58}$$

$$A_{TE,1}^{c} = a_{TE,100}^{c-} J_{\nu_0}(\kappa_{10}\rho) e^{-j\nu_0\phi} e^{-j\beta_0 z} + a_{TE,100}^{c+} Y_{\nu_0}(\kappa_{10}\rho) e^{-j\nu_0\phi} e^{-j\beta_0 z} \text{ in region 1,} \tag{4.59}$$

$$A_{TM,2}^{c} = a_{TM,200}^{c} J_{\nu_0}(\kappa_{20}\rho) e^{-j\nu_0\phi} e^{-j\beta_0 z} \text{ in region 2,} \tag{4.60}$$

$$A_{TE,2}^{c} = a_{TE,200}^{c} J_{\nu_0}(\kappa_{20}\rho) e^{-j\nu_0\phi} e^{-j\beta_0 z} \text{ in region 2.} \tag{4.61}$$

Here $a_{TM,i00}^{c}$ and $a_{TE,i00}^{c}$ denote the unknown coefficients to be determined in terms of the exciting wave and κ_{i0} is given by (4.14), which denotes the propagation constants of cylindrical modes. The boundary conditions of the problem require that the tangential components of the electric and magnetic fields should be continuous across the cylindrical interfaces at $\rho = \rho_0$ and $\rho = \rho_1$, that is:

$$e_{200}(\rho_1)\begin{pmatrix} a_{TM,200}^{c} \\ a_{TE,200}^{c} \end{pmatrix} = e_{100}^{-}(\rho_1)\begin{pmatrix} a_{TM,100}^{c-} \\ a_{TE,100}^{c-} \end{pmatrix} + e_{100}^{+}(\rho_1)\begin{pmatrix} a_{TM,100}^{c+} \\ a_{TE,100}^{c+} \end{pmatrix}, \tag{4.62}$$

$$h_{200}(\rho_1)\begin{pmatrix} a_{TM,200}^{c} \\ a_{TE,200}^{c} \end{pmatrix} = h_{100}^{-}(\rho_1)\begin{pmatrix} a_{TM,100}^{c-} \\ a_{TE,100}^{c-} \end{pmatrix} + h_{100}^{+}(\rho_1)\begin{pmatrix} a_{TM,100}^{c+} \\ a_{TE,100}^{c+} \end{pmatrix}, \tag{4.63}$$

$$e_{100}^{-}(\rho_0)\begin{pmatrix} a_{TM,100}^{c-} \\ a_{TE,100}^{c-} \end{pmatrix} + e_{100}^{+}(\rho_0)\begin{pmatrix} a_{TM,100}^{c+} \\ a_{TE,100}^{c+} \end{pmatrix} = e_{000}(\rho_0)\begin{pmatrix} a_{TM,000}^{c} \\ a_{TE,000}^{c} \end{pmatrix} + e^{inc}(\rho_0)\begin{pmatrix} a_{TM}^{inc} \\ a_{TE}^{inc} \end{pmatrix}, \tag{4.64}$$

$$h_{100}^{-}(\rho_0)\begin{pmatrix} a_{TM,100}^{c-} \\ a_{TE,100}^{c-} \end{pmatrix} + h_{100}^{+}(\rho_0)\begin{pmatrix} a_{TM,100}^{c+} \\ a_{TE,100}^{c+} \end{pmatrix} = h_{000}(\rho_0)\begin{pmatrix} a_{TM,000}^{c} \\ a_{TE,000}^{c} \end{pmatrix} + h^{inc}(\rho_0)\begin{pmatrix} a_{TM}^{inc} \\ a_{TE}^{inc} \end{pmatrix}, \tag{4.65}$$

where e_{i00} and h_{i00} are given by (4.30)-(4.37) with $m = n = 0$. Here a_{TM}^{inc} and a_{TE}^{inc} denote the coefficients given in (4.2) and the matrices e^{inc} and h^{inc} are given by

$$e^{inc}(\rho) = \frac{1}{j\omega\varepsilon_0\rho}\begin{bmatrix} -v_0\beta_0 J_{v_0}(\kappa_{00}\rho) & j\omega\varepsilon_0\rho\kappa_{00}J'_{v_0}(\kappa_{00}\rho) \\ \kappa_{00}^2\rho J_{v_0}(\kappa_{00}\rho) & 0 \end{bmatrix}, \tag{4.66}$$

$$h^{inc}(\rho) = \frac{1}{j\omega\mu_0\rho}\begin{bmatrix} 0 & \kappa_{00}^2\rho J_{v_0}(\kappa_{00}\rho) \\ j\omega\mu_0\rho\kappa_{00}J'_{v_0}(\kappa_{00}\rho) & v_0\beta_0 J_{v_0}(\kappa_{00}\rho) \end{bmatrix}. \tag{4.67}$$

Next, the set of equations are solved algebraically for the coefficients $a_{TM,000}^c$ and $a_{TE,000}^c$. An expression is obtained in matrix form;

$$\begin{pmatrix} a_{TM,000}^c \\ a_{TE,000}^c \end{pmatrix} = [e_{000}(\rho_0)]^{-1}\zeta_Q^c e^{inc}(\rho_0)\begin{pmatrix} a_{TM}^{inc} \\ a_{TE}^{inc} \end{pmatrix}, \tag{4.68}$$

where

$$\zeta_Q^c = \left\{h_{000}(\rho_0)[e_{000}(\rho_0)]^{-1} - Y_{000}^c\right\}^{-1}\left\{Y_{000}^c - h^{inc}(\rho_0)[e^{inc}(\rho_0)]^{-1}\right\}, \tag{4.69}$$

$$Y_{000}^c = \left\{h_{100}^-(\rho_0)[e_{100}^-(\rho_0)]^{-1} + h_{100}^+(\rho_0)[e_{100}^+(\rho_0)]^{-1}\zeta_{000}^c\right\}\left\{I_{2\times 2} + \zeta_{000}^c\right\}^{-1}, \tag{4.70}$$

$$\zeta_{000}^c = e_{100}^+(\rho_0)[e_{100}^+(\rho_1)]^{-1}\zeta_{100}^c e_{100}^-(\rho_1)[e_{100}^-(\rho_0)]^{-1}, \tag{4.71}$$

$$\zeta_{100}^c = \left\{h_{100}^+(\rho_1)[e_{100}^+(\rho_1)]^{-1} - h_{200}(\rho_1)[e_{200}(\rho_1)]^{-1}\right\}^{-1} \left\{h_{200}(\rho_1)[e_{200}(\rho_1)]^{-1} - h_{100}^-(\rho_1)[e_{100}^-(\rho_1)]^{-1}\right\}. \tag{4.72}$$

In that case, the electric fields $\mathbf{E}^{inc}$ and $\mathbf{E}_0^c$ in (4.55) are established as follows:

$$\begin{aligned} \begin{pmatrix} E_\phi^{inc} + E_{0\phi}^c \\ E_z^{inc} + E_{0z}^c \end{pmatrix} &= e_{000}(\rho_0)\begin{pmatrix} a_{TM,000}^c \\ a_{TE,000}^c \end{pmatrix} e^{-jv_0\phi}e^{-j\beta_0 z} + e^{inc}(\rho_0)\begin{pmatrix} a_{TM}^{inc} \\ a_{TE}^{inc} \end{pmatrix} e^{-jv_0\phi}e^{-j\beta_0 z} \\ &= (\zeta_Q^c + I_{2\times 2})e^{inc}(\rho_0)\begin{pmatrix} a_{TM}^{inc} \\ a_{TE}^{inc} \end{pmatrix} e^{-jv_0\phi}e^{-j\beta_0 z}. \end{aligned} \tag{4.73}$$

Recall that in the previous section, the unknown coefficients $a_{TM,0mn}$ and $a_{TE,0mn}$ of the scattered electric field $\mathbf{E}_0^s$ in (4.55) is expressed in terms of the surface currents. Substituting the expression (4.49) into (4.24), the tangential components of the scattered electric field outside the cylindrical structure are obtained as

$$\begin{aligned}\begin{pmatrix} E_{0\phi}(\rho_0,\phi,z) \\ E_{0z}(\rho_0,\phi,z)\end{pmatrix} &= \sum_m\sum_n e_{0mn}(\rho_0)\begin{pmatrix} a_{TM,0mn} \\ a_{TE,0mn}\end{pmatrix}\psi_{mn}(\phi,z) \\ &= \sum_m\sum_n e_{0mn}(\rho_0)[e_{0mn}(\rho_0)]^{-1} Z_Q \begin{pmatrix}\left\langle J_\phi,\psi^*_{mn}(\phi,z)\right\rangle \\ \left\langle J_z,\psi^*_{mn}(\phi,z)\right\rangle\end{pmatrix}\psi_{mn}(\phi,z) \\ &= \sum_m\sum_n Z_Q \begin{pmatrix}\left\langle J_\phi,\psi^*_{mn}(\phi,z)\right\rangle \\ \left\langle J_z,\psi^*_{mn}(\phi,z)\right\rangle\end{pmatrix}\psi_{mn}(\phi,z)\,. \end{aligned} \tag{4.74}$$

(4.55) can therefore be written as

$$\begin{pmatrix} E^{inc}_\phi(\rho_0,\phi,z)+E^c_{0\phi}(\rho_0,\phi,z) \\ E^{inc}_z(\rho_0,\phi,z)+E^c_{0z}(\rho_0,\phi,z)\end{pmatrix} + \sum_m\sum_n Z_Q \begin{pmatrix}\left\langle J_\phi,\psi^*_{mn}(\phi,z)\right\rangle \\ \left\langle J_z,\psi^*_{mn}(\phi,z)\right\rangle\end{pmatrix}\psi_{mn}(\phi,z) = 0 \text{ on } \partial s\,, \tag{4.75}$$

or as

$$\sum_m\sum_n Z_Q \begin{pmatrix}\left\langle J_\phi,\psi^*_{mn}(\phi,z)\right\rangle \\ \left\langle J_z,\psi^*_{mn}(\phi,z)\right\rangle\end{pmatrix}\psi_{mn}(\phi,z) = -\begin{pmatrix} E^{inc}_\phi(\rho_0,\phi,z)+E^c_{0\phi}(\rho_0,\phi,z) \\ E^{inc}_z(\rho_0,\phi,z)+E^c_{0z}(\rho_0,\phi,z)\end{pmatrix} \text{ on } \partial s\,. \tag{4.76}$$

If the constitutive parameters of the dielectric shell were equal to that of the free-space $(\varepsilon_1=\varepsilon_0)$ or if its thickness were zero $(\rho_1=\rho_0)$, one can easily show that the expressions given for Z_Q (denoted by Z_{Q_0} in this case) in (4.50)-. (4.53) would simplify to those given in [10]. That is,

$$Z_{Q_0} = \frac{-\pi}{2\omega\varepsilon_0} J_{v_m}(\kappa_{0n}\rho_0)H^{(2)}_{v_m}(\kappa_{0n}\rho_0)\begin{bmatrix} k_0^2\rho_0\dfrac{J'_{v_m}(\kappa_{0n}\rho_0)H'^{(2)}_{v_m}(\kappa_{0n}\rho_0)}{J_{v_m}(\kappa_{0n}\rho_0)H^{(2)}_{v_m}(\kappa_{0n}\rho_0)}+\dfrac{1}{\rho_0}\left(\dfrac{v_m\beta_n}{\kappa_{0n}}\right)^2 & -v_m\beta_n \\ -v_m\beta_n & \kappa_{0n}^2\rho_0\end{bmatrix}. \tag{4.77}$$

Furthermore, if the conducting patches were infinitely long in *z* direction, Z_Q would then simplify to

$$\frac{-\pi k_0^2\rho_0}{2\omega\varepsilon_0}\begin{bmatrix} J'_{v_m}(k_0\rho_0)H'^{(2)}_{v_m}(k_0\rho_0) & 0 \\ 0 & J_{v_m}(k_0\rho_0)H^{(2)}_{v_m}(k_0\rho_0)\end{bmatrix}. \tag{4.78}$$

The problems involving free-standing and infinitely long strips are analyzed in [10], where the surface currents of the problems are expanded into sub-domain basis functions in MM solutions and a “conjugate gradient fast Fourier transform method” is utilized. It is shown in Chapter 3 that the direct computations of the matrix elements in MM solutions are difficult because the resultant infinite sums are slowly convergent with respect to the summation index *m*. It is also the case for the problem considered in this chapter, where a dielectric shell is involved. The infinite sums should be handled properly in order to circumvent slow convergence difficulties. One approach is to use sub-domain basis functions in conjunction with a conjugate gradient fast Fourier transform method as done in [10]. Another approach is to use entire-domain basis functions together with a convergence acceleration method based on a Kummer's series acceleration method, as described in [18, 21]. Here, we go along with the second approach and use a convergence acceleration method.

In Appendix C, it is shown that the matrices Z_Q and Z_{Q_0} both have the same asymptotic form. That is,

$$Z_Q \cong Z_{Q_0} \cong Z_{Q_a} \text{ as } |v_m| \to \infty, \tag{4.79}$$

where Z_{Q_a} is given as

$$Z_{Q_a} = \begin{bmatrix} Z_{\phi\phi_a} & Z_{\phi z_a} \\ Z_{z\phi_a} & Z_{zz_a} \end{bmatrix} = \frac{j\omega\mu_0}{2k_0^2|v_m|} \begin{bmatrix} \dfrac{v_m^2}{\rho_0} & v_m\beta_n \\ v_m\beta_n & -\kappa_{0n}^2\rho_0 \end{bmatrix}. \tag{4.80}$$

The integral equation (4.76) can be solved more easily by rearranging its terms as follows;

$$\sum_m\sum_n \left\{Z_Q - Z_{Q_0}\right\} \begin{pmatrix} \left\langle J_\phi, \psi_{mn}^*(\phi,z)\right\rangle \\ \left\langle J_z, \psi_{mn}^*(\phi,z)\right\rangle \end{pmatrix} \psi_{mn}(\phi,z) + \sum_m\sum_n Z_{Q_0} \begin{pmatrix} \left\langle J_\phi, \psi_{mn}^*(\phi,z)\right\rangle \\ \left\langle J_z, \psi_{mn}^*(\phi,z)\right\rangle \end{pmatrix} \psi_{mn}(\phi,z) =$$
$$-\begin{pmatrix} E_\phi^{inc}(\rho_0,\phi,z) + E_{0\phi}^c(\rho_0,\phi,z) \\ E_z^{inc}(\rho_0,\phi,z) + E_{0z}^c(\rho_0,\phi,z) \end{pmatrix} \text{ on } \partial s \text{ .(4.81)}$$

Now the first part on the left hand side in .(4.81) converges more rapidly because both Z_Q and Z_{Q_0} asymptotically equal to Z_{Q_a} as $m \to \infty$. However, the second part should be computed by employing an appropriate acceleration method as will be given in the following section.

4.3. The MM Solution of the problem

For the problem considered in this chapter, the numerical results are obtained by assuming that the patches are narrow rectangular strips oriented in *z* direction. In that case, ϕ components of the surface currents may be ignored, that is $J_\phi = 0$. Accordingly, the current in the *z* direction is expanded into entire domain sinusoidal basis functions of the form

$$J_z = \sum_{q=1}^{Q} c_q f_q \ , \tag{4.82}$$

where the basis functions are

$$f_q = \sin\left\{\tfrac{q\pi}{l}(z + \tfrac{l}{2})\right\}. \tag{4.83}$$

Here *l* denotes the strip length and c_q denote unknown expansion coefficients. By substituting the expansion (4.82) into the integral equation (4.76), one obtains

$$\sum_{q=1}^{Q} c_q \sum_m \sum_n Z_{zz} \left\langle f_q , \psi^*_{mn}(\phi, z)\right\rangle \psi_{mn}(\phi, z) = -\left(E_z^{inc}(\rho_0, \phi, z) + E_{0z}^{c}(\rho_0, \phi, z)\right) \text{ on } \partial s \ , \tag{4.84}$$

where Z_{zz} is the element in the second row and second column of the 2x2 matrix Z_Q given in (4.50). When both sides of the above equation is inner producted by a basis function f_p, the following equation is obtained

$$\sum_{q=1}^{Q} c_q \sum_m \sum_n Z_{zz} < f_q , \psi^*_{mn}(\phi, z) >< f_p , \psi_{mn}(\phi, z) > =$$
$$< f_p , -\left(E_z^{inc}(\rho_0, \phi, z) + E_{0z}^{c}(\rho_0, \phi, z)\right) > . \tag{4.85}$$

When the process is repeated for *p*=1, 2, . . ., Q, a system of equations is obtained. The equations can be put into a matrix form

$$\begin{bmatrix} A_{11} & A_{12} & \cdots & \\ A_{21} & A_{22} & \cdots & \\ \vdots & \vdots & \ddots & \\ & & & A_{QQ} \end{bmatrix} \begin{bmatrix} c_1 \\ c_2 \\ \vdots \\ c_Q \end{bmatrix} = \begin{bmatrix} B_1 \\ B_2 \\ \vdots \\ B_Q \end{bmatrix}, \tag{4.86}$$

where

$$A_{pq} = \sum_m \sum_n Z_{zz} < f_q, \psi^*_{mn}(\phi,z) >< f_p, \psi_{mn}(\phi,z) > = \sum_m \sum_n Z_{zz} C^*_{nq} C_{np} S^2_{v_m} \ , \quad (4.87)$$

$$B_p = \left\langle f_p, -\left(E_z^{inc}(\rho_0,\phi,z) + E^c_{0z}(\rho_0,\phi,z)\right)\right\rangle , \quad (4.88)$$

$$C_{np} = \int_{-l/2}^{l/2} \frac{e^{-jk_{z_n}z}}{\sqrt{T_z}} \sin[\tfrac{p\pi}{l}(z+\tfrac{l}{2})]dz = \frac{p\pi l}{\sqrt{T_z}} \frac{(-1)^p e^{-jk_{z_n}l/2} - e^{jk_{z_n}l/2}}{(k_{z_n}l)^2 - (p\pi)^2} , \quad (4.89)$$

$$C^*_{nq} = \int_{-l/2}^{l/2} \frac{e^{jk_{z_n}z}}{\sqrt{T_z}} \sin[\tfrac{q\pi}{l}(z+\tfrac{l}{2})]dz = \frac{q\pi l}{\sqrt{T_z}} \frac{(-1)^q e^{jk_{z_n}l/2} - e^{-jk_{z_n}l/2}}{(k_{z_n}l)^2 - (q\pi)^2} , \quad (4.90)$$

$$S_{v_m} = \int_{-w/2a}^{w/2a} \frac{e^{-jv_m\phi}}{\sqrt{T_\phi}} d\phi = \frac{w}{a\sqrt{T_\phi}} \frac{\sin\left(v_m w/2a\right)}{v_m w/2a} . \quad (4.91)$$

Now the unknown coefficients can be determined by an inversion; $[c_q] = [A_{pq}]^{-1}[B_p]$.

As discussed in Section 4.2, the infinite sums in (4.87) are slowly convergent with respect to the index m. However the convergence can be accelerated by employing Kummer's acceleration method as follows:

$$\begin{aligned}
A_{pq} &= \sum_m \sum_n Z_{zz} C^*_{nq} C_{np} S^2_{v_m} \\
&= \sum_{n=-\infty}^{\infty} C^*_{nq} C_{np} \sum_{m=-\infty}^{\infty} S^2_{v_m} Z_{zz} \\
&= \sum_{n=-\infty}^{\infty} C^*_{nq} C_{np} \sum_{m=-\infty}^{\infty} S^2_{v_m} (Z_{zz} - Z_{zz_a}) + \sum_{n=-\infty}^{\infty} C^*_{nq} C_{np} \sum_{m=-\infty}^{\infty} S^2_{v_m} Z_{zz_a} \\
&= \sum_{n=-\infty}^{\infty} C^*_{nq} C_{np} \sum_{m=-\infty}^{\infty} S^2_{v_m} (Z_{zz} - Z_{zz_a}) + \sum_{n=-\infty}^{\infty} C^*_{nq} C_{np} \sum_{m=-\infty}^{\infty} S^2_{v_m} \frac{-j\omega\mu_0}{2k_0^2 \left|v_m\right|} \kappa^2_{0n} \rho_0 \\
&= \sum_{n=-\infty}^{\infty} C^*_{nq} C_{np} \sum_{m=-\infty}^{\infty} S^2_{v_m} (Z_{zz} - Z_{zz_a}) - \frac{j\omega\mu_0\rho_0}{2k_0^2} \sum_{n=-\infty}^{\infty} C^*_{nq} C_{np} \kappa^2_{0n} \sum_{m=-\infty}^{\infty} \frac{S^2_{v_m}}{\left|v_m\right|} \\
&= \sum_{n=-\infty}^{\infty} C^*_{nq} C_{np} \sum_{m=-\infty}^{\infty} S^2_{v_m} (Z_{zz} - Z_{zz_a}) - \frac{\pi\omega\mu_0\rho_0}{2k_0^2} I \sum_{n=-\infty}^{\infty} C^*_{nq} C_{np} \kappa^2_{0n} \ , \quad (4.92)
\end{aligned}$$

where I involves a slowly convergent infinite sum

$$I = \frac{j}{\pi} \sum_{m=-\infty}^{\infty} \frac{S^2_{v_m}}{\left|v_m\right|} , \quad (4.93)$$

and Z_{zz_a} is given in (4.80), which denotes the asymptotic value of Z_{zz},

$$Z_{zz_a} = \frac{-j\omega\mu_0}{2k_0^2\left|v_m\right|}\kappa_{0n}^2\rho_0, \tag{4.94}$$

The first part on the right hand side in (4.92) converges rapidly because,

$$Z_{zz} \cong Z_{zz_a} \text{ as } |\, v_m \,| \to \infty, \tag{4.95}$$

as shown in Appendix C. The second part in (4.92) can be computed with the same approach considered in Chapter 3, since the expressions for Z_{zz_0}, C_{np}, C_{nq}^*, and S_{v_m} in this chapter are exactly the same as that given in Chapter 3. Note that the expression for I is also identical to the expression that was given in Chapter 3, (3.47). So, the infinite sum in I is can be computed as described in Appendix A.

The MM solutions formulated so far correspond to a single cylindrical wave excitation given in (4.1). The solutions have to be determined separately for each individual cylindrical wave component of the incident plane wave. Using the superposition principle, the total solution is obtained by summing the individual solutions. The decomposition of a plane wave into the cylindrical wave components is considered in Chapter 2. Once the MM solutions for the coefficients c_q are obtained, RCS of the structure as defined in (2.68) is determined using

$$RCS = \lim_{\rho\to\infty} 2\pi\rho \frac{\left|\sum_{v_0=-\infty}^{\infty}\left\{\mathbf{E}_0^c(\rho,\phi,z)+\mathbf{E}_0^s(\rho,\phi,z)\right\}\right|^2}{\left|\mathbf{E}^i\right|^2}. \tag{4.96}$$

Here $\mathbf{E}_0^s$ denotes the electric field due to the surface currents on the conducting patches, $\mathbf{E}_0^c$ denotes the field that is scattered by the dielectric shell when the conducting patches are not present and $\mathbf{E}^i$ denotes the electric field of the incident plane wave. As discussed in Chapter 2, if the incident plane wave has a unit amplitude vector potential then the denominator of (4.96) is

$$\left|\mathbf{E}^i\right| = 120\pi\kappa_{00}, \tag{4.97}$$

where κ_{00} is given by (4.14). The scattered electric fields of the problem are written in terms of the coefficients c_q by using (4.24), (4.49), and (4.82)

$$\begin{pmatrix} E_{0\phi}^{s}(\rho,\phi,z) \\ E_{0z}^{s}(\rho,\phi,z) \end{pmatrix} = \sum_{m}\sum_{n} e_{0mn}(\rho)[e_{0mn}(\rho_0)]^{-1}\begin{pmatrix} Z_{\phi z} \\ Z_{zz} \end{pmatrix}\left\langle J_{z_{mn}}, \psi_{mn}^{*}(\phi,z)\right\rangle \psi_{mn}(\phi,z)$$

$$= \sum_{m}\sum_{n} e_{0mn}(\rho)[e_{0mn}(\rho_0)]^{-1}\begin{pmatrix} Z_{\phi z} \\ Z_{zz} \end{pmatrix}\sum_{q=1}^{Q} c_q \left\langle f_q, \psi_{mn}^{*}(\phi,z)\right\rangle \psi_{mn}(\phi,z)$$

$$= \sum_{m}\sum_{n} e_{0mn}(\rho)[e_{0mn}(\rho_0)]^{-1}\begin{pmatrix} Z_{\phi z} \\ Z_{zz} \end{pmatrix} S_{v_m}\psi_{mn}(\phi,z)\sum_{q=1}^{Q} c_q C_{nq}^{*} \, . \tag{4.98}$$

Here, the matrix $e_{0mn}(\rho)$ as $\rho\to\infty$ is computed using the large argument asymptotic forms of the Hankel functions (2.74) and (2.75), that is

$$e_{0mn}(\rho) \cong \frac{1}{j\omega\varepsilon_0\rho}\sqrt{\frac{2\kappa_{0n}\rho}{\pi}}e^{j\pi/4+jv_m\pi/2}e^{-j\kappa_{0n}\rho}\begin{bmatrix} 0 & -j\omega\varepsilon_0 \\ \kappa_{0n} & 0 \end{bmatrix} \text{ as } \rho\to\infty. \tag{4.99}$$

Using (4.73), the fields $\mathbf{E}_0^c$ are written as

$$\begin{pmatrix} E_{0\phi}^{c} \\ E_{0z}^{c} \end{pmatrix} = e_{000}(\rho)[e_{000}(\rho_0)]^{-1}\zeta_Q^c e^{inc}(\rho_0)\begin{pmatrix} a_{TM}^{inc} \\ a_{TE}^{inc} \end{pmatrix} e^{-jv_0\phi}e^{-j\beta_0 z}, \tag{4.100}$$

where $e^{inc}(\rho_0)$ and ζ_Q^c are given in (4.66)- (4.72) and the matrix $e_{000}(\rho)$ is determined asymptotically as

$$e_{000}(\rho) \cong \frac{1}{j\omega\varepsilon_0\rho}\sqrt{\frac{2\kappa_{00}\rho}{\pi}}e^{j\pi/4+jv_0\pi/2}e^{-j\kappa_{00}\rho}\begin{bmatrix} 0 & -j\omega\varepsilon_0 \\ \kappa_{00} & 0 \end{bmatrix} \text{ as } \rho\to\infty. \tag{4.101}$$

Finally, the RCS (4.96) is determined by combining the expressions (4.98)-(4.100).

The coupling for the cylindrical structures is described in section 2.3. When a plane wave is incident on a cylindrical structure, the coupling is defined as the total power measured at the center of the structure. For the cylindrical structure of this chapter, we use the definition given in (2.77) that is

$$Coupling = \lim_{\rho\to\infty}\frac{\left|\mathbf{E}^{inc}(\rho,\phi,z)+\mathbf{E}_0^c(\rho,\phi,z)+\mathbf{E}_0^s(\rho,\phi,z)\right|^2}{\left|\mathbf{E}^{inc}(\rho,\phi,z)\right|^2}, \tag{4.102}$$

where $\mathbf{E}^{inc}$ denotes the electric field that would be radiated by a line current if the cylindrical structure was not present. Those fields are established in section 2.3 and the electric field $\mathbf{E}^{inc}$ is given by (2.88) and (2.89). When $\rho\to\infty$, the limiting value of it is obtained as

$$\begin{aligned}\mathbf{E}^{inc} &= \mathbf{a}_z \frac{1}{j\omega\varepsilon_0} a_{TM}^{inc} \kappa_{00}^2 H_0^{(2)}(\kappa_{00}\rho) e^{-j\beta_0 z} \\ &= \mathbf{a}_z \frac{1}{j\omega\varepsilon_0} a_{TM}^{inc} \kappa_{00}^2 \sqrt{\frac{2}{\pi\kappa_{00}\rho}} e^{j\pi/4} e^{-j\kappa_{00}\rho} e^{-j\beta_0 z} \\ &= \mathbf{a}_z \frac{1}{j\omega\varepsilon_0} a_{TM}^{inc} \kappa_{00}^2 \sqrt{\frac{2}{\pi\kappa_{00}\rho}} e^{j\pi/4} e^{-j\kappa_{00}\rho} e^{-j\beta_0 z} \text{ as } \rho \to \infty. \end{aligned} \quad (4.103)$$

Then the coupling is determined by using this expression and the corresponding asymptotic expressions of the scattered fields appearing in (4.102).

In order to test the accuracy and the validity of our methods, a cylindrical structure that was previously analyzed in the literature [10] is reconsidered and the numerical results are given in Chapter 5. In [10], a cylindrical structure consisting of infinitely long strips is analyzed by using sub-domain basis functions together with a conjugate gradient fast Fourier transform method in MM solutions. But here, we also include a dielectric shell inside the cylindrical structure and use entire domain basis functions in MM solutions. Since the structure is uniform in *z* direction, the induced currents and the scattered fields can be assumed to be uniform in *z* direction. The two dimensional Floquet modes of the problem simplify to

$$\psi_m(\phi) = \frac{e^{-j v_m \phi}}{\sqrt{T_\phi}}, \quad (4.104)$$

and the propagation constants in that are

$$\beta_n = 0, \quad (4.105)$$

$$v_m = v_0 + 2\pi m / T_\phi. \quad (4.106)$$

The matrix elements in MM solutions are determined from the expression given in (4.87). For a TM wave excitation, we set J_ϕ=0 and expand the axial current J_z as

$$J_z = \sum_{q=0}^{Q} c_q f_q = \sum_{q=0}^{Q} c_q \cos\left\{\tfrac{q\pi\rho_0}{w}\left(\phi - \tfrac{w}{2\rho_0}\right)\right\}, \text{ for TM excitation.} \quad (4.107)$$

In that case, the corresponding matrix elements of the MM solution are accelerated as follows

$$\begin{aligned}
A_{pq} &= \sum_{m=-\infty}^{\infty} Z_{zz} < f_q, \psi_m^*(\phi) >< f_p, \psi_m(\phi) > \\
&= \sum_{m=-\infty}^{\infty} \left(Z_{zz} - Z_{zz_a} \right) < f_q, \psi_m^*(\phi) >< f_p, \psi_m(\phi) > + \sum_{m-\infty}^{\infty} Z_{zz_a} < f_q, \psi_m^*(\phi) >< f_p, \psi_m(\phi) > \\
&= \sum_{m=-\infty}^{\infty} \left(Z_{zz} - Z_{zz_a} \right) < f_q, \psi_m^*(\phi) >< f_p, \psi_m(\phi) > + I_{TM} ,
\end{aligned} \tag{4.108}$$

where the inner products are determined as

$$\begin{aligned}
&< f_q, \psi_m^*(\phi) >< f_p, \psi_m(\phi) >= \\
&= \left\{ \int_{-\frac{w}{2\rho_0}}^{\frac{w}{2\rho_0}} \cos\left\{ \tfrac{q\pi\rho_0}{w} \left(\phi - \tfrac{w}{2\rho_0} \right) \right\} \frac{\left(e^{-jv_m\phi} \right)^*}{\sqrt{T_\phi}} d\phi \right\} \left\{ \int_{-\frac{w}{2\rho_0}}^{\frac{w}{2\rho_0}} \cos\left\{ \tfrac{p\pi\rho_0}{w} \left(\phi - \tfrac{w}{2\rho_0} \right) \right\} \frac{e^{-jv_m\phi}}{\sqrt{T_\phi}} d\phi \right\} \\
&= \frac{-jv_m \left(e^{j\frac{w}{2\rho_0}v_m} - (-1)^q e^{-j\frac{w}{2\rho_0}v_m} \right)}{\sqrt{T_\phi} \left(v_m^2 - \left(\frac{q\pi\rho_0}{w} \right)^2 \right)} \frac{jv_m \left(e^{-j\frac{w}{2\rho_0}v_m} - (-1)^p e^{j\frac{w}{2\rho_0}v_m} \right)}{\sqrt{T_\phi} \left(v_m^2 - \left(\frac{p\pi\rho_0}{w} \right)^2 \right)} \\
&= \frac{\left(1 + (-1)^{p+q} - (-1)^p e^{j\frac{w}{\rho_0}v_m} - (-1)^q e^{-j\frac{w}{\rho_0}v_m} \right) v_m^2}{T_\phi \left(v_m^2 - \left(\frac{q\pi\rho_0}{w} \right)^2 \right) \left(v_m^2 - \left(\frac{p\pi\rho_0}{w} \right)^2 \right)} ,
\end{aligned} \tag{4.109}$$

and the function I_{TM} is given in terms of the asymptotic form Z_{zz_a} in (4.80)

$$\begin{aligned}
I_{TM} &= \sum_{m=-\infty}^{\infty} Z_{zz_a} < f_q, \psi_m^*(\phi) >< f_p, \psi_m(\phi) > \\
&= \sum_{m=-\infty}^{\infty} \frac{-j\omega\mu_0}{2k_0^2 |v_m|} \kappa_{0n}^2 \rho_0 < f_q, \psi_m^*(\phi) >< f_p, \psi_m(\phi) > \\
&= \frac{-j\omega\mu\rho_0}{2T_\phi} \sum_{m=-\infty}^{\infty} \frac{\left(1 + (-1)^{p+q} - (-1)^p e^{j\frac{w}{\rho_0}v_m} - (-1)^q e^{-j\frac{w}{\rho_0}v_m} \right) |v_m|}{\left(v_m^2 - \left(\frac{q\pi\rho_0}{w} \right)^2 \right) \left(v_m^2 - \left(\frac{p\pi\rho_0}{w} \right)^2 \right)} .
\end{aligned} \tag{4.110}$$

On the other hand, when the excitation is a TE wave: we set $J_z = 0$ and expand the current J_ϕ as

$$J_\phi = \sum_{q=1}^{Q} c_q f_q = \sum_{q=1}^{Q} c_q \sin\left\{ \tfrac{q\pi\rho_0}{w} \left(\phi - \tfrac{w}{2\rho_0} \right) \right\}, \text{ for TE excitation.} \tag{4.111}$$

In that case, the corresponding matrix elements of the MM solution are accelerated as follows:

$$
\begin{aligned}
A_{pq} &= \sum_{m=-\infty}^{\infty} Z_{\phi\phi} < f_q, \psi_m^*(\phi) >< f_p, \psi_m(\phi) > \\
&= \sum_{m=-\infty}^{\infty} \left(Z_{\phi\phi} - Z_{\phi\phi_a} \right) < f_q, \psi_m^*(\phi) >< f_p, \psi_m(\phi) > + \sum_{m=-\infty}^{\infty} Z_{\phi\phi_a} < f_q, \psi_m^*(\phi) >< f_p, \psi_m(\phi) > \\
&= \sum_{m=-\infty}^{\infty} \left(Z_{\phi\phi} - Z_{\phi\phi_a} \right) < f_q, \psi_m^*(\phi) >< f_p, \psi_m(\phi) > + I_{TE}, \qquad (4.112)
\end{aligned}
$$

where

$$
\begin{aligned}
&< f_q, \psi_m^*(\phi) >< f_p, \psi_m(\phi) > \\
&= \left\{ \int_{-\frac{w}{2\rho_0}}^{\frac{w}{2\rho_0}} \sin\left\{ \tfrac{q\pi\rho_0}{w} \left(\phi - \tfrac{w}{2\rho_0} \right) \right\} \frac{\left(e^{-jv_m\phi} \right)^*}{\sqrt{T_\phi}} d\phi \right\} \left\{ \int_{-\frac{w}{2\rho_0}}^{\frac{w}{2\rho_0}} \sin\left\{ \tfrac{p\pi\rho_0}{w} \left(\phi - \tfrac{w}{2\rho_0} \right) \right\} \frac{e^{-jv_m\phi}}{\sqrt{T_\phi}} d\phi \right\} \\
&= \frac{\frac{q\pi\rho_0}{w} \left(e^{j\frac{w}{2\rho_0}v_m} - (-1)^q e^{-j\frac{w}{2\rho_0}v_m} \right)}{\sqrt{T_\phi} \left(v_m^2 - \left(\frac{q\pi\rho_0}{w} \right)^2 \right)} \frac{\frac{p\pi\rho_0}{w} \left(e^{-j\frac{w}{2\rho_0}v_m} - (-1)^p e^{j\frac{w}{2\rho_0}v_m} \right)}{\sqrt{T_\phi} \left(v_m^2 - \left(\frac{p\pi\rho_0}{w} \right)^2 \right)} \\
&= \frac{\left(1 + (-1)^{p+q} - (-1)^p e^{j\frac{w}{\rho_0}v_m} - (-1)^q e^{-j\frac{w}{\rho_0}v_m} \right) qp \left(\frac{\pi\rho_0}{w} \right)^2}{T_\phi \left(v_m^2 - \left(\frac{q\pi\rho_0}{w} \right)^2 \right) \left(v_m^2 - \left(\frac{p\pi\rho_0}{w} \right)^2 \right)}, \qquad (4.113)
\end{aligned}
$$

and the function I_{TE} is given in terms of the asymptotic form $Z_{\phi\phi_a}$ in (4.80)

$$
\begin{aligned}
I_{TE} &= \sum_{m=-\infty}^{\infty} Z_{\phi\phi_a} < f_q, \psi_m^*(\phi) >< f_p, \psi_m(\phi) > \\
&= \sum_{m=-\infty}^{\infty} \frac{j\omega\mu_0}{2k_0^2} \frac{\left| v_m \right|}{\rho_0} < f_q, \psi_m^*(\phi) >< f_p, \psi_m(\phi) > \\
&= \frac{j\omega\mu_0}{2T_\phi k_0^2 \rho_0} qp \left(\frac{\pi\rho_0}{w} \right)^2 \sum_{m=-\infty}^{\infty} \frac{\left(1 + (-1)^{p+q} - (-1)^p e^{j\frac{w}{\rho_0}v_m} - (-1)^q e^{-j\frac{w}{\rho_0}v_m} \right) \left| v_m \right|}{\left(v_m^2 - \left(\frac{q\pi\rho_0}{w} \right)^2 \right) \left(v_m^2 - \left(\frac{p\pi\rho_0}{w} \right)^2 \right)}. \qquad (4.114)
\end{aligned}
$$

Note that, both the functions I_{TM} and I_{TE} are given in terms of an infinite sum, which can be decomposed into various infinite sums of the form

$$
\sum_{m=1}^{\infty} e^{i\alpha(v_0 + m2\pi/T_\phi)} f_m \text{ or } \sum_{m=-1}^{-\infty} e^{i\alpha(v_0 + m2\pi/T_\phi)} f_m, \qquad (4.115)
$$

where

$$f_m = \frac{\left|(v_0 + m2\pi / T_\phi)\right|}{\left((v_0 + m2\pi / T_\phi)^2 - \left(\frac{q\pi\rho_0}{w}\right)^2\right)\left((v_0 + m2\pi / T_\phi)^2 - \left(\frac{p\pi\rho_0}{w}\right)^2\right)} . \tag{4.116}$$

A convergence acceleration method for infinite sums of this type is given in Appendix A. So, the infinite sums are calculated as described in the appendix.

5. NUMERICAL RESULTS

Numerical results given in this chapter are obtained by using entire domain basis functions in MM solutions. The currents on the narrow rectangular strips or the electric fields on the slots are expanded into seven basis functions. The resulting slowly convergent infinite sums are accelerated as described in the previous chapters. For cylindrical structures involving infinitely long strips, the problems become one dimensional and the MM solutions of the currents are obtained as described in Section 4.3.

An important parameter in scattering studies is the electromagnetic scattering by a target which is usually represented by its radar cross section (RCS). The RCS is defined as “the area intercepting the amount of power that, when scattered isotropically, produces at the receiver a density that is equal to the density scattered by the actual target” [23]. Another important parameter for the cylindrical structures is the electromagnetic field couplings into the cylindrical structures. The coupling is defined as the total power measured at the center of a cylindrical structure when a plane wave is incident on the structure. So, the couplings and the RCS are determined for several types of cylindrical structures and the numerical results are plotted versus the frequency or the observation angle in the circumferential direction.

5.1. Comparisons with the results found in the literature

To test the accuracy and validity of our methods and techniques, a cylindrical structure that was previously analyzed in the literature [10] is reconsidered. In [10], a cylindrical structure consisting of infinitely long strips oriented in *z* direction is analyzed by using sub-domain basis functions together with a conjugate gradient fast Fourier transform method in MM solutions. But here, we also include a dielectric shell inside the cylindrical structure and use entire domain basis functions in MM solutions. Since the structure is uniform in *z* direction, the induced currents and the scattered fields can be assumed to be uniform in *z* direction. The resulting infinite

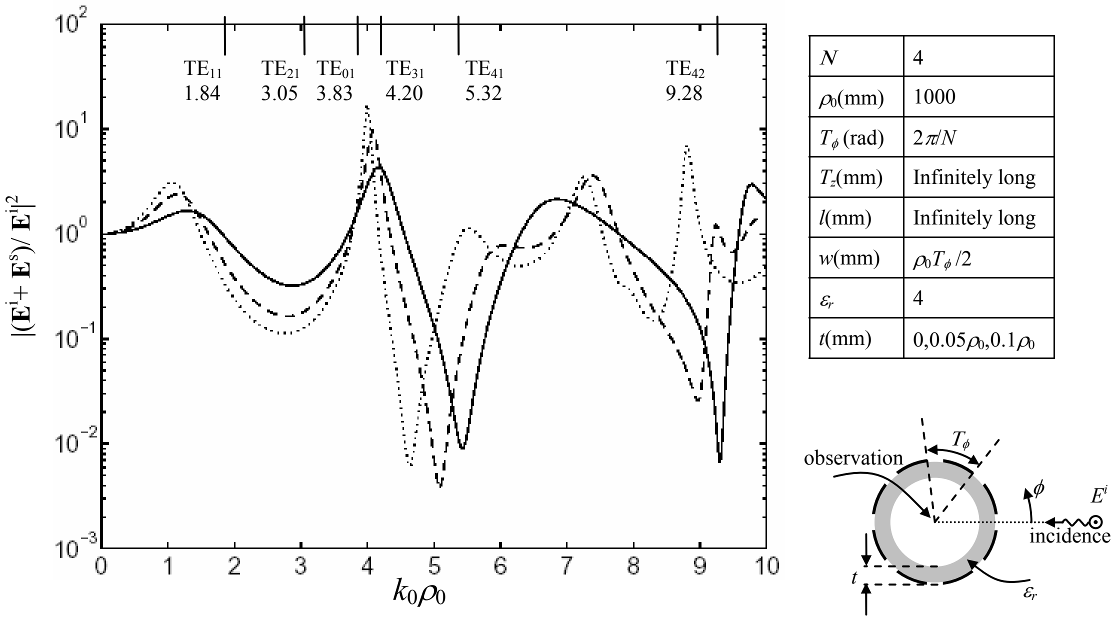

N	4
ρ_0(mm)	1000
T_ϕ (rad)	$2\pi/N$
T_z(mm)	Infinitely long
l(mm)	Infinitely long
w(mm)	$\rho_0 T_\phi/2$
ε_r	4
t(mm)	$0, 0.05\rho_0, 0.1\rho_0$

Figure 5.1 The field couplings at the origin versus the electrical length of the radius for infinitely long strips located on a dielectric shell. A TE plane wave is normally incident ($\phi^{inc}=0^0$) and the scattered fields are computed at the origin ($\rho=0$) of the cylindrical structure. The curve for $t=0$ case matches to the result given by [10].

—— $t=0$, - - - - $t=0.05\rho_0$, ⋯⋯ $t=0.1\rho_0$.

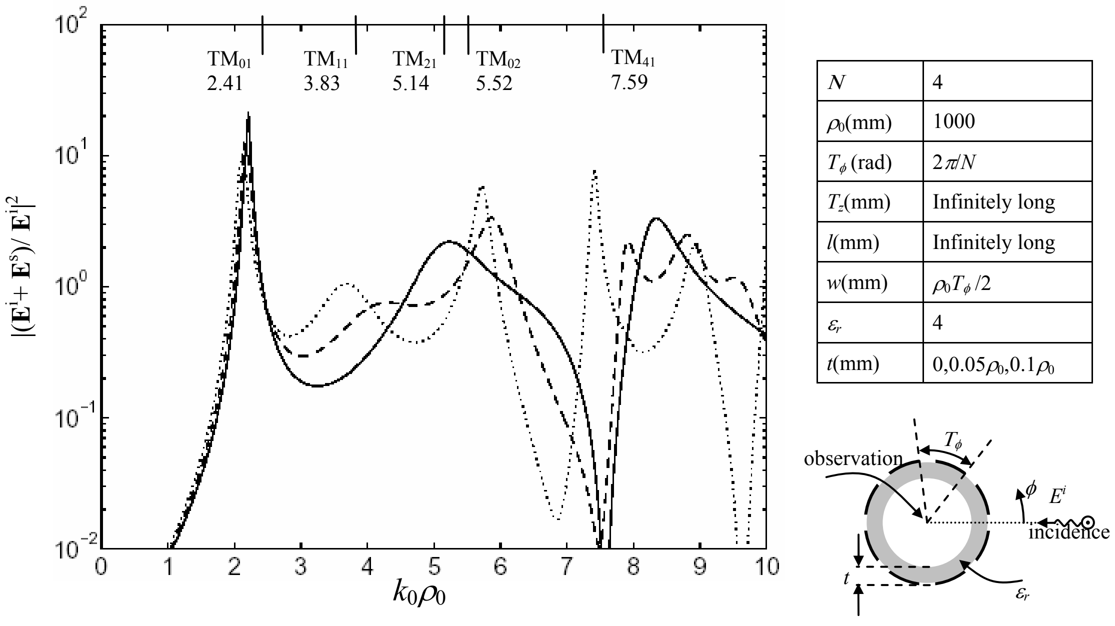

N	4
ρ_0(mm)	1000
T_ϕ (rad)	$2\pi/N$
T_z(mm)	Infinitely long
l(mm)	Infinitely long
w(mm)	$\rho_0 T_\phi/2$
ε_r	4
t(mm)	$0, 0.05\rho_0, 0.1\rho_0$

Figure 5.2 The field couplings at the origin versus the electrical length of the radius for infinitely long strips located on a dielectric shell. A TM plane wave is normally incident ($\phi^{inc}=0^0$) and the scattered fields are computed at the origin ($\rho=0$) of the cylindrical structure. The curve for $t=0$ case matches to the result given by [10].

—— $t=0$, - - - - $t=0.05\rho_0$, ⋯⋯ $t=0.1\rho_0$.

sums in the MM solutions are accelerated by using the expressions (4.104)-(4.116) and the electromagnetic field couplings (the total fields at ρ=0) are determined as described in Section 4.3.

For the results given in Figure 5.1 (TE excitation case) and Figure 5.2 (TM excitation case), it is assumed that four strips (N=4) are located on the outer surface of a dielectric shell having radius ρ_0=1000mm. The strip widths are chosen such that the angular extend of a strip equals to one half of the periodicity of a unit cell, that is $w/\rho_0 = 0.5T_\phi$, where T_ϕ denotes the periodicity of the structure in ϕ direction, T_ϕ=$2\pi/N$=$\pi/2$. The results are obtained by using nine basis functions in the MM solutions. For a TE excitation case, the couplings are plotted versus $k_0\rho_0$ (the electrical length of the radius) as in Figure 5.1. The plot given for the case t=0 corresponds to a free-standing strips structure, which is considered in [10] and the agreement between them is excellent. In that plot, resonances are detected at $k_0\rho_0$≅5.32 and $k_0\rho_0$≅9.28 where the coupling almost vanishes. Note that those resonances occur at the cut-off frequencies of the circular waveguide modes TE_{41} and TE_{42}, respectively. As the dielectric shell thickness (t) is varied from t=0 to t=0.1ρ_0, it is seen from the plots that the resonances are moved toward left. If a TM excitation case is considered, the couplings become as shown in Figure 5.2. As in the previous figure, the plot for the case t=0 corresponds to a result given in [10] and the agreements between them is excellent. A resonance that is corresponding to cut-off frequency of TM_{41} mode is detected at $k_0\rho_0$≅7.59 where the coupling vanishes. Also, the coupling makes a sharp peak at $k_0\rho_0$≅2.2 and reaches to a value 20.3 in the vicinity of the cut-off frequency of TM_{01} mode. While the shell thickness (t) increases, the resonances are shifted toward left on the figure. Furthermore, the plots become more oscillatory and extra resonances are observed.

When thickness (t) and radius (ρ_0) of the dielectric shell are fixed (t=0.05ρ_0 and ρ_0=1000mm) but the number of strips (N) around the shell is varied, the numerical results are obtained as shown in Figure 5.3 and Figure 5.4. The other parameters of the structure are as given in the inset and the plots are given for a TE excitation case. It is assumed that the angular extend of a strip equals to one half of the periodicity of a unit cell, that is $w/\rho_0 = \frac{1}{2}2\pi / N = \pi / N$. When N is varied from N=4 to N=32, the

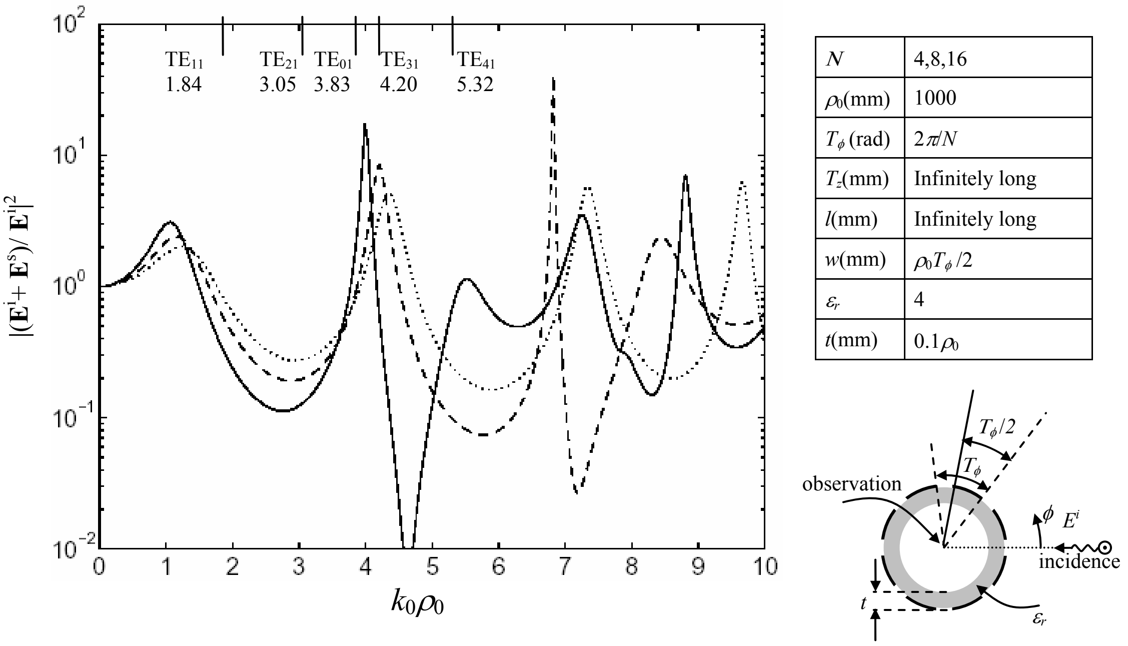

N	4,8,16
ρ_0(mm)	1000
T_ϕ (rad)	$2\pi/N$
T_z(mm)	Infinitely long
l(mm)	Infinitely long
w(mm)	$\rho_0 T_\phi/2$
ε_r	4
t(mm)	$0.1\rho_0$

Figure 5.3 The field couplings at the origin versus the electrical length of the radius ($k_0\rho_0$) for infinitely long strips located on a dielectric shell. The number of elements (N) in the circumferential direction is varied. The cylinder radius (ρ_0) is kept constant. A TE plane wave is normally incident ($\phi^{inc}=0^0$) and the scattered fields are computed at the origin ($\rho=0$) of the cylindrical structure.

—— N=4, - - - - N=8, ······ N=16.

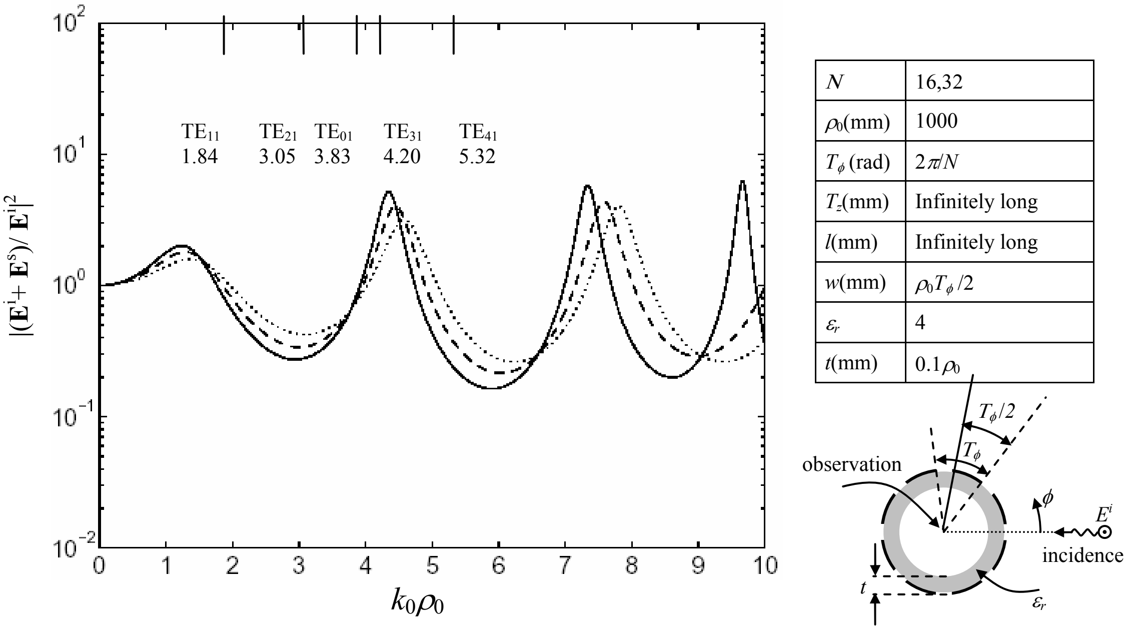

N	16,32
ρ_0(mm)	1000
T_ϕ (rad)	$2\pi/N$
T_z(mm)	Infinitely long
l(mm)	Infinitely long
w(mm)	$\rho_0 T_\phi/2$
ε_r	4
t(mm)	$0.1\rho_0$

Figure 5.4 The field couplings of the structure considered in Figure 5.3 when the number of elements (N) in the circumferential direction is further increased.

—— N=16, - - - - N=32, ······ without strips.

strip width (w) decreases since the radius is fixed (ρ_0=1000mm). That's why; one can predict that the magnitudes of ϕ-directed currents decrease as N is increased. This prediction is verified by the plots given in the two figures, which reveal that the strips become less prominent as N is increased. Specifically, the plot corresponding to the case N=32 in Figure 5.4 is in close proximity to a plot corresponding to the non-existence of strips.

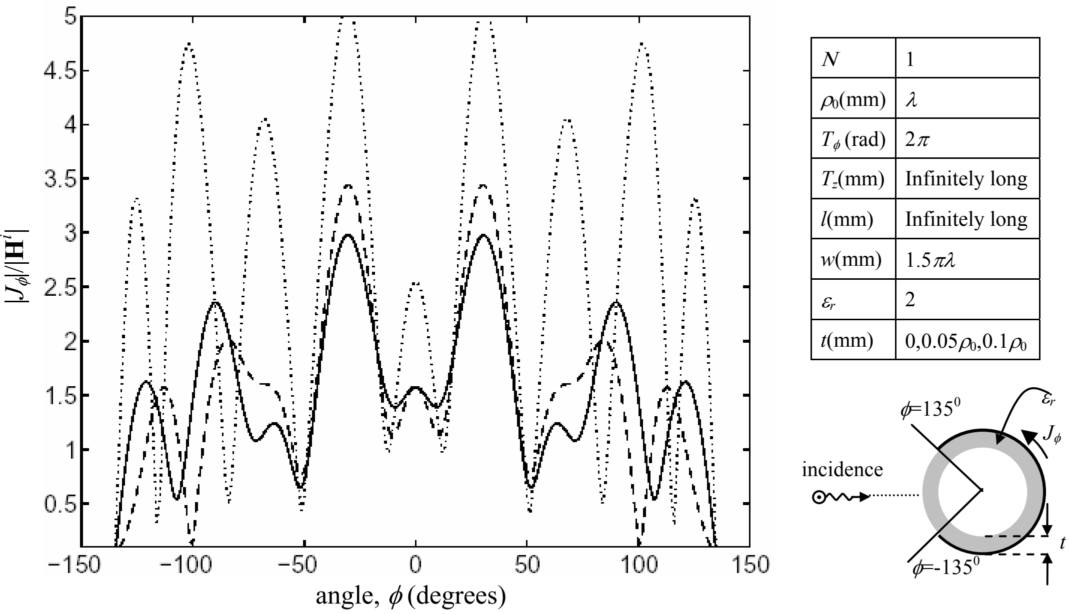

N	1
ρ_0(mm)	λ
T_ϕ (rad)	2π
T_z(mm)	Infinitely long
l(mm)	Infinitely long
w(mm)	$1.5\pi\lambda$
ε_r	2
t(mm)	0,0.05ρ_0,0.1ρ_0

Figure 5.5 The magnitude of the currents induced on the conducting wall of a cylindrical cavity that is located on a dielectric shell. The slit region subtends an angle of $\pi/2$ and other parameters are as given in the inset. A TE plane wave is normally incident (ϕ^{inc}=180^0) on the cylindrical structure. The curve for t=0 case matches to the result given by [10].

—— t=0, - - - - t=0.05ρ_0, ······ t=0.1ρ_0.

In Figure 5.5, the magnitude of currents induced on the conducting wall of a cylindrical cavity is given. On the cylinder surface, a slit subtends an arc length $0.5\pi\lambda$ and the conducting wall subtends an arc length w=$1.5\pi\lambda$, where λ denotes the wavelength. For a TE excitation case, the MM solutions of the induced currents are obtained by using the expressions (4.111)- (4.114). Since the arc length of the conductor is rather large in terms of the wavelength (w=$1.5\pi\lambda$), accurate results are achieved after expanding the currents into 15 sinusoidal basis functions. When the number of basis functions is further increased, the current profile is not influenced significantly. Note that the plot for the case t=0 corresponds to non-existence the dielectric shell, which is considered in [10] and the agreement between the plots is excellent. As the thickness is increased, the currents become more oscillatory and also are amplified appreciably.

5.2. Numerical results for free-standing axial strips

In Figure 5.6, RCS of free-standing and infinitely long strips are plotted versus frequency. The radius and the width of strips are fixed but, the number of elements (N) in the circumferential direction is varied as seen in the inset. It is assumed that a TM polarized plane wave is normally incident ($\phi^{inc} = 0$) on the cylindrical structure and the scattered fields are observed in the back side ($\phi = 180^0$) of the structure. The results show that, as N increases, the scattered field magnitudes increase in average. The small ripples on the plots occur very close to the TM cut-off frequencies of circular waveguides as labeled in the figure.

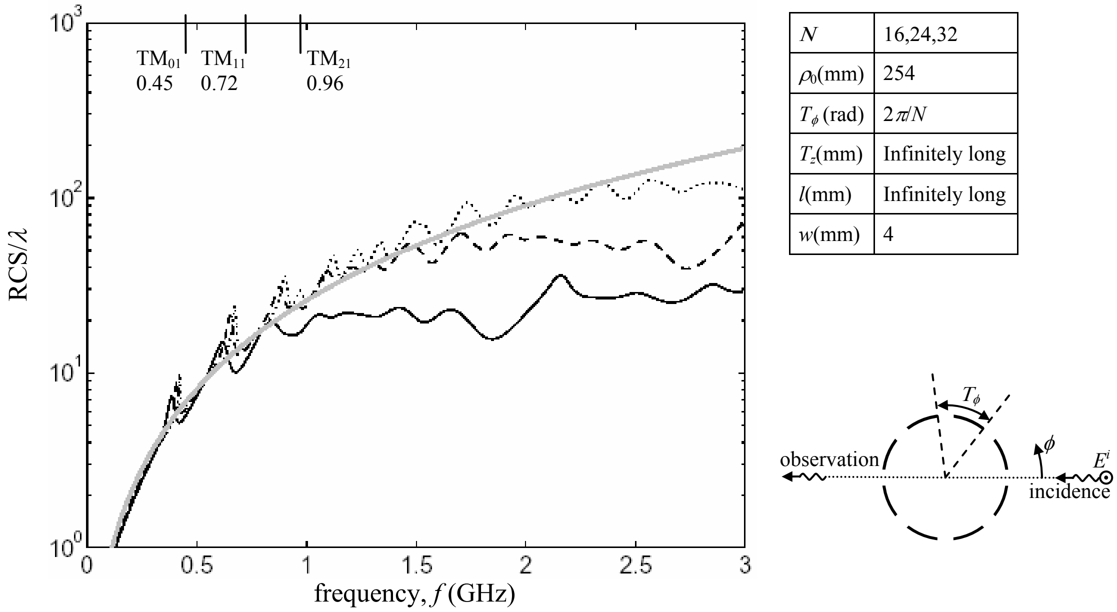

N	16,24,32
ρ_0(mm)	254
T_ϕ (rad)	$2\pi/N$
T_z(mm)	Infinitely long
l(mm)	Infinitely long
w(mm)	4

Figure 5.6 RCS versus frequency for free-standing and infinitely long strips. The number of elements (N) in the circumferential direction is varied. A TM plane wave is normally incident (ϕ^{inc}=0^0) and the scattered fields are computed in the back side (ϕ=180^0) of the structure.

—— N=16, - - - - N=24, ······ N=32, ▬ Conducting circular cylinder.

In Figure 5.7, RCS of the cylindrical structure considered in the previous figure are plotted versus frequency for the case where the observations are made in the front side ($\phi = 0^0$) of the cylindrical structure. As N increases, the scattered field magnitudes increase. The small ripples at the lower frequencies occur very close to the TM cut-off frequencies of circular waveguides. We see from the figure that the scattered wave amplitudes in the front side of the structure are very small compared to the fields at the back side of the cylinder. See plots in Figure 5.6 and Figure 5.7. Furthermore, there are too many fluctuations with respect to frequency. These effects are reasonable since the currents induced on the strips should have some small phase progressions in the propagation direction of the incident plane wave. In that case, the fields radiated from those current will be in-phase in the back side of the structure. However this does not happen in the front side of the cylindrical structure and the field magnitudes rapidly vary due to the cancellations.

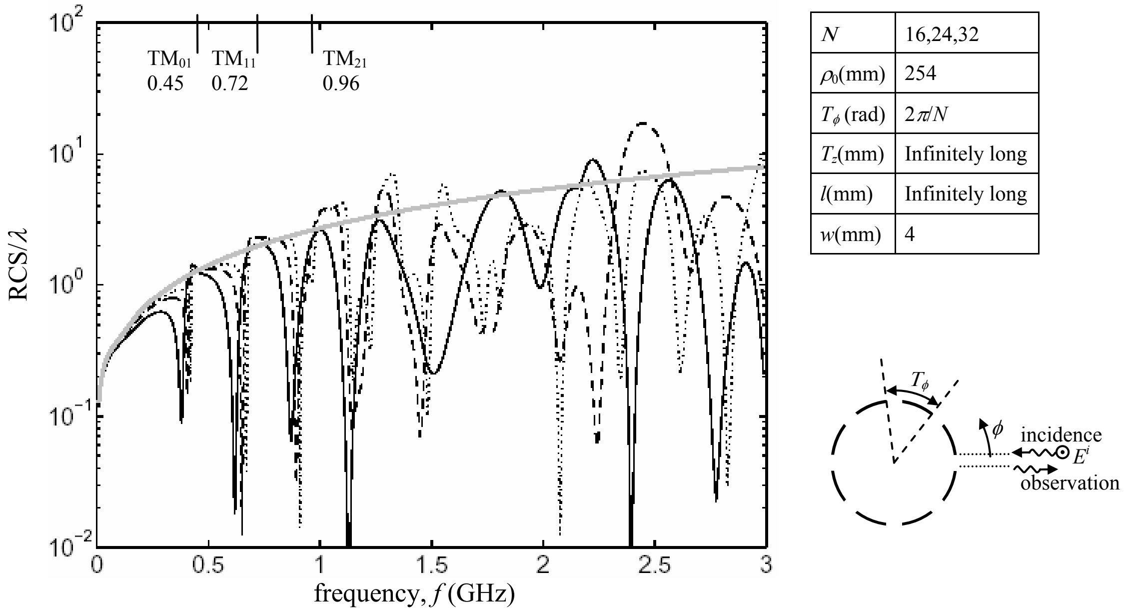

N	16,24,32
ρ_0(mm)	254
T_ϕ (rad)	$2\pi/N$
T_z(mm)	Infinitely long
l(mm)	Infinitely long
w(mm)	4

Figure 5.7 RCS of the structure considered in Figure 5.6 when the scattered fields are computed in the front side (ϕ=0^0).

—— N=16, - - - - N=24, …… N=32, —— Conducting circular cylinder.

Figure 5.8 shows the variation of the RCS versus frequency of a cylindrical structure having finite length strips. The number of strips in the circumferential direction is fixed to N=32 and the strips are assumed to be free-standing. The plots are given for various lengths of the strips. A TM polarized plane wave is assumed to be normally incident ($\phi^{inc}=0^0$) on the cylindrical structure and the scattered fields are observed in the back side ($\phi=180^0$) of the structure. As l decreases, the magnitudes of the induced currents decrease as well and that causes reductions on the scattered field amplitudes.

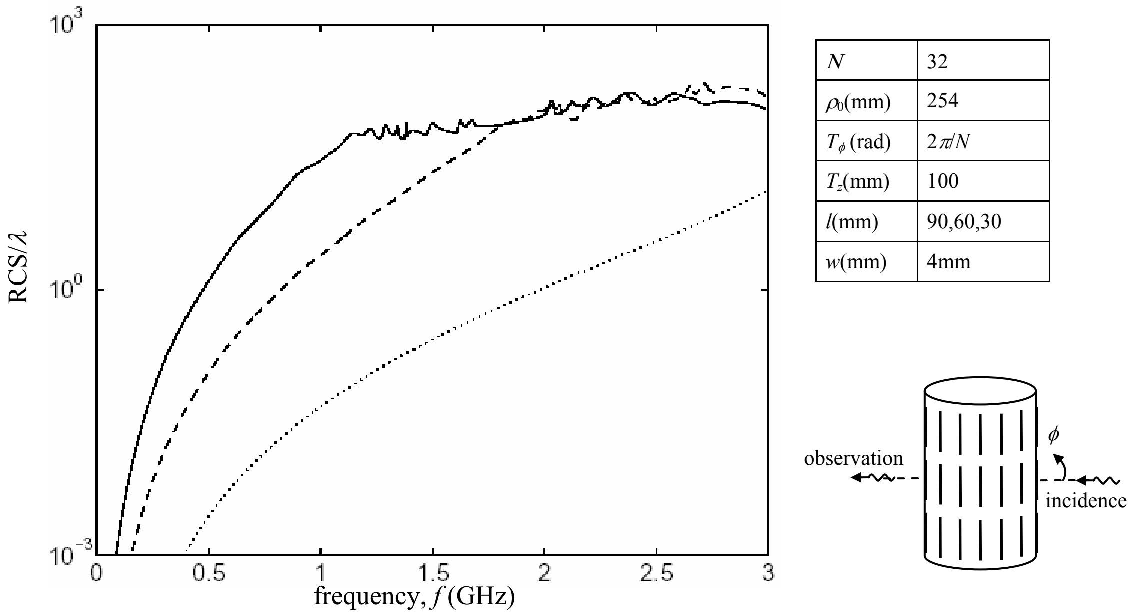

N	32
ρ_0(mm)	254
T_ϕ (rad)	$2\pi/N$
T_z(mm)	100
l(mm)	90,60,30
w(mm)	4mm

Figure 5.8 RCS versus frequency for free-standing rectangular strips. The length of strips (l) is varied and other parameters are as shown in the inset. A TM plane wave is normally incident ($\phi^{inc}=0^0$) and the scattered fields are computed in the back side ($\phi=180^0$) of the cylindrical structure.

—— l=90mm, - - - - l=60mm, ······ l=30mm.

In Figure 5.9, the RCS of the cylindrical structure considered in Figure 5.8 are plotted versus frequency but this time, the observations are made in the front side ($\phi=0^0$) of the structure. The figure shows that the scattered wave amplitudes in the front side of the structure are very small and fluctuating when compared with those in the back side given in the previous figure. The small ripples at the lower frequencies occur very close to the TM cut-off frequencies of circular waveguides.

In Figure 5.10, the electromagnetic field couplings into a cylindrical structure made up of free-standing strips are plotted versus frequency. The length (l) of strips is varied. The parameters of the structure assumed are given in the inset. A TM polarized plane wave is assumed to be normally incident ($\phi^{inc}=0^0$) on the cylindrical structure and the fields are computed at the origin ($\rho=0$) of the cylindrical structure.

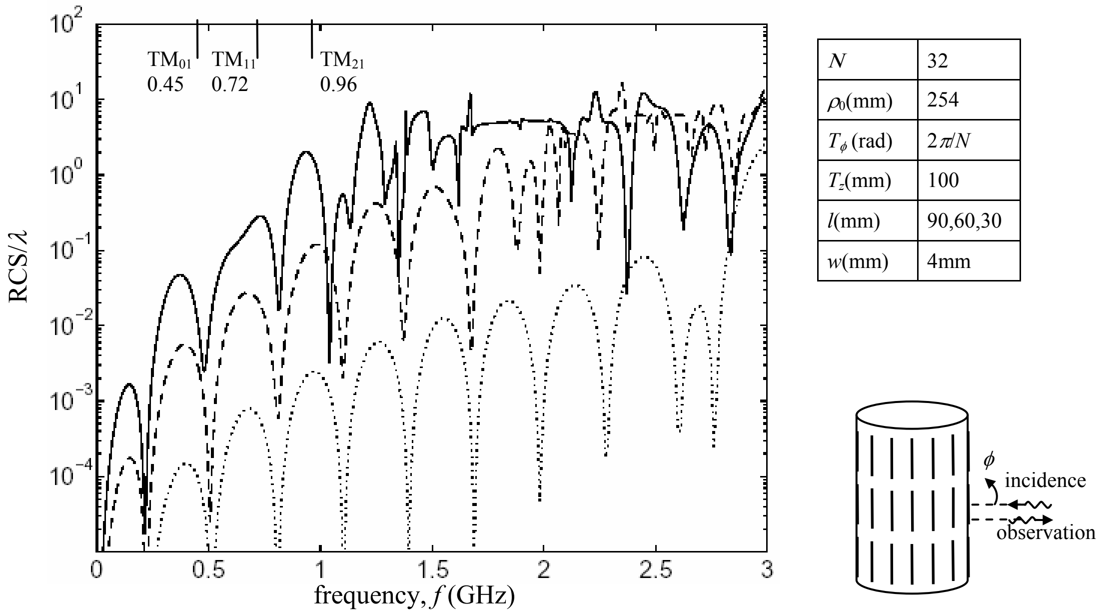

N	32
ρ_0(mm)	254
T_ϕ (rad)	$2\pi/N$
T_z(mm)	100
l(mm)	90,60,30
w(mm)	4mm

Figure 5.9 RCS of the structure considered in Figure 5.8 when the scattered fields are computed in the front side (ϕ=0^0).

—— l=90mm, - - - - l=60mm, ⋯⋯ l=30mm.

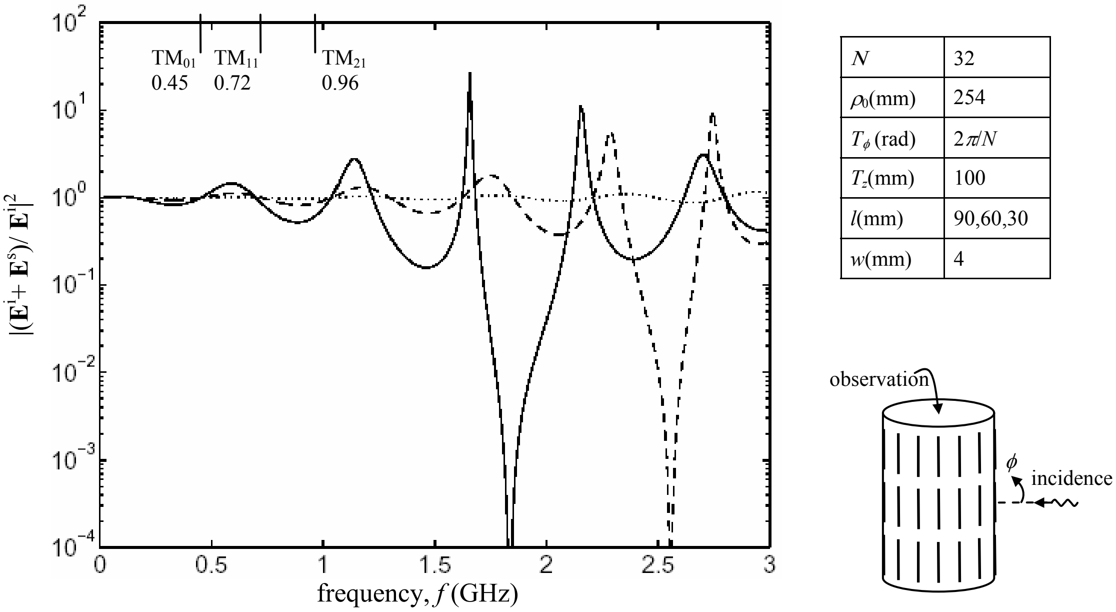

N	32
ρ_0(mm)	254
T_ϕ (rad)	$2\pi/N$
T_z(mm)	100
l(mm)	90,60,30
w(mm)	4

Figure 5.10 The field couplings at the origin versus frequency for free-standing rectangular strips. The length of strips (l) is varied and other parameters are as shown in the inset. A TM plane wave is normally incident (ϕ^{inc}=0^0) and the scattered fields are computed at the origin (ρ=0) of the cylindrical structure.

—— l=90mm, - - - - l=60mm, ⋯⋯ l=30mm.

When *l*=90mm, the plot reveals that a resonance appears at 1.82GHz and the coupling shows a null. The total field inside the cylindrical structure almost vanishes at that frequency. This is attributed to the fact that the fields of the incident plane wave are cancelled by the fields due to the surface currents on the strips. For the case *l*=60mm, the same phenomena is observed at a higher frequency, 2.55GHz. If the length is further decreased, namely for the case *l*=30mm, a null in the field is not detected in the frequency range of interest (from 0 to 3GHz). However it may be possible to have a null at a higher frequency. “For l=30mm case, it is recognized that the structure becomes totally transparent at low frequencies”. Another interesting result observed from the plots is that the couplings equal unity at several frequencies. When the coupling equals unity, it means that the fields due to the surface currents on the strips cancel themselves and only the incident plane wave is detected at the origin. It is seen from the figure that the corresponding frequencies of this phenomenon are very close to the TM cut-off frequencies of circular waveguides. This phenomenon is also discussed in [19].

5.3. Numerical results for conducting cylinders perforated with axial slots

In Figure 5.11, RCS of a conducting circular cylinder perforated periodically with rectangular slots are given. This cylindrical structure is the dual of the structure where strips are freely standing. The length (*l*) of the slots on the conducting cylinder is varied. The assumed parameters of the structure are as given in the inset. It is assumed that a TE polarized plane wave is normally incident ($\phi^{inc}=0^0$) on to the cylindrical structure and the scattered fields are observed in the back side ($\phi=180^0$) of the cylinder. When *l*=90mm the plot reveals that a resonance occurs at 1.82GHz and the RCS show a null. Close to that frequency the structure becomes almost invisible at that frequency. This is due to the fact that the far fields radiated by the “magnetic currents” flowing on the slotted regions of the cylinder are cancelled by the fields due to the “electric currents” flowing on the conducting parts of the cylinder. Such a property may be very useful in radar applications. However, the same effect is not observed when *l*=60mm. However a dip is observed at a higher frequency, at 2.5 GHz. The small ripples at the lower frequencies occur very close to TE cut-off frequencies of circular waveguides, which are labeled in the figure. If the slot length is further decreased to *l*=30mm, the resonance disappears (or at least it is shifted toward higher frequencies) and the corresponding curve of this case becomes indistinguishable from the curve of a smooth conducting circular cylinder.

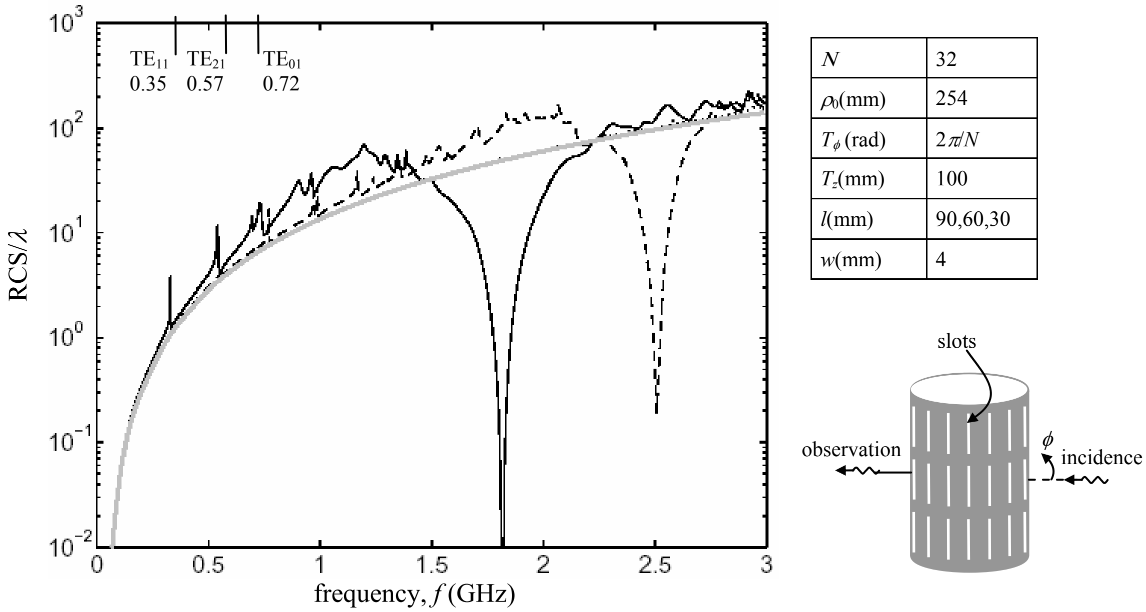

N	32
ρ_0(mm)	254
T_ϕ (rad)	$2\pi/N$
T_z(mm)	100
l(mm)	90,60,30
w(mm)	4

Figure 5.11 RCS versus frequency for a conducting circular cylinder perforated periodically with rectangular slots. The length of slots (l) is varied and other parameters are as shown in the inset. A TE plane wave is normally incident ($\phi^{inc}=0^0$) and the scattered fields are computed in the back side ($\phi=180^0$) of the cylindrical structure.

—— l=90mm, ---- l=60mm, ······ l=30mm, ▬ l=0 (Conducting circular cylinder).

In Figure 5.12, the RCS are determined in the front side ($\phi=0^0$) of the slotted conducting cylinder. The results are plotted for various lengths of slots. The incident plane wave and the other parameters of the cylindrical structure are the same as in the previous figure. The results show that the scattered wave amplitudes in the front side of the structure are very small and fluctuating when compared with those in the back side given in the previous figure. It is since the aperture fields on the slotted regions have small phase progressions in the propagation direction of the incident plane wave. In that case, the fields radiated from the slotted regions will be in-phase in the back side of the structure. However this does not happen in the front side of the cylindrical structure and the field magnitudes become smaller due to the cancellations of the scattered fields from the slotted regions. A similar phenomenon was discussed for the cylindrical structure of Figure 5.7. The small ripples at the lower frequencies occur very close to TE cut-off frequencies of circular waveguides, which are labeled in the Figure. As the slot length (*l*) decreases, the “magnetic current” magnitudes on the slotted regions reduce and that causes reductions on the scattered field amplitudes. That’s why, the plot for *l*=30mm case is almost indistinguishable from the plot for a smooth conducting circular cylinder. This problem is also considered in [20].

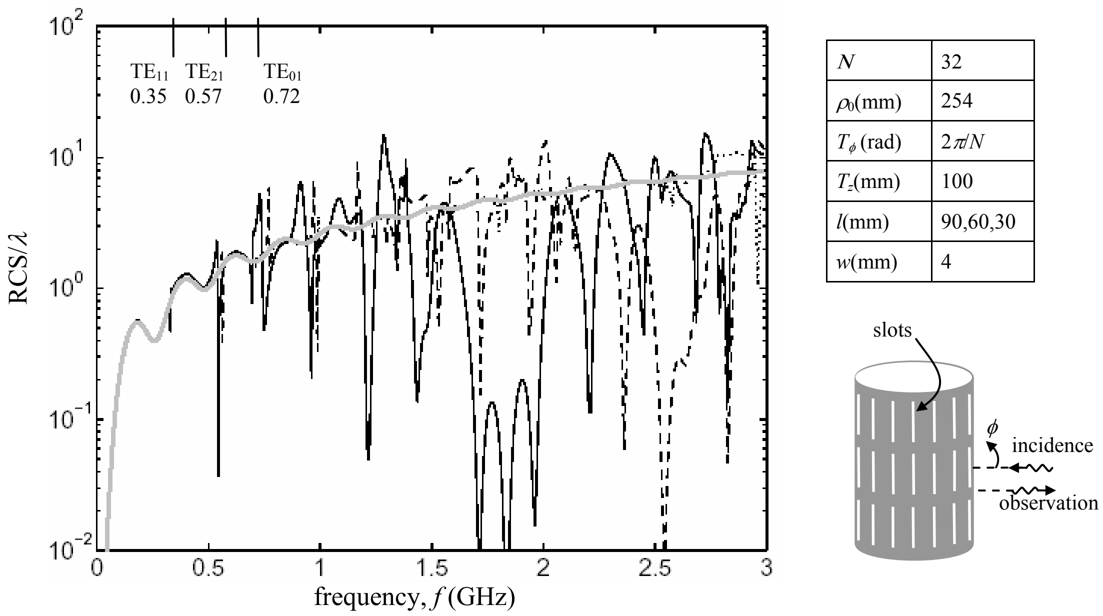

N	32
ρ_0(mm)	254
T_ϕ (rad)	$2\pi/N$
T_z(mm)	100
l(mm)	90,60,30
w(mm)	4

Figure 5.12 RCS of the structure considered in Figure 5.11 when the scattered fields are computed in the front side (ϕ=0^0).

—— *l*=90mm, - - - - *l*=60mm, ······ *l*=30mm, ▬ *l*=0 (Conducting circular cylinder).

The numerical results for electromagnetic field penetrations (couplings) into the slotted conducting cylinder are given in Figure 5.13. The incident plane wave and the other parameters of the cylindrical structure are the same as in the previous figures but here the observations are made at the origin (ρ=0). The numerical results are plotted for various slot lengths (*l*). When *l*=90mm, the corresponding plot reveals that a resonance occurs at a frequency 1.65GHz, where the coupling curve makes a sharp peak. This is attributed to the internal resonances in the cylindrical structure. Note that the resonant frequency is very close to the cut-off frequency of TE_{01} mode and similar resonances also occur at higher frequencies. As the slot length is varied, the resonant frequencies do not change significantly but the peaks become sharper. When the slot length is very small (namely for the case *l*=30mm), the coupled field amplitudes are extremely weak on out-of-resonant-frequencies. It is concluded from the results that the resonances in cylindrical structures are not dependent on the length of slots but they occur near the cut-off frequencies of circular waveguide modes. Hence, the resonant frequencies are dependent on the curvature of the cylindrical surface. On the other hand, the resonant frequencies of planar structures involving periodically located slots are dependent on the length of slots.

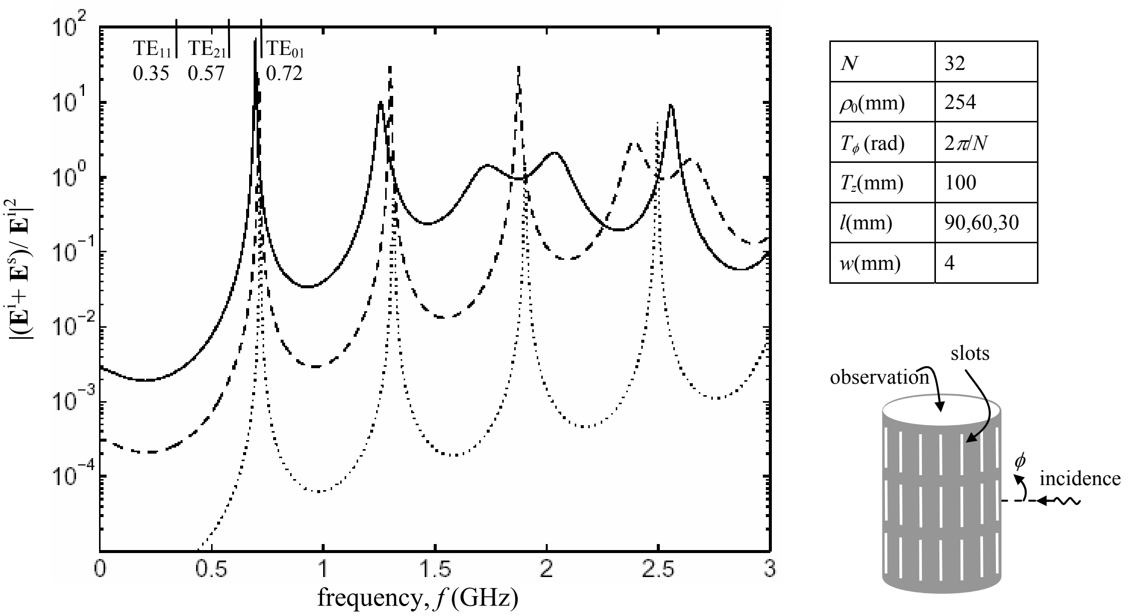

N	32
ρ_0(mm)	254
T_ϕ (rad)	$2\pi/N$
T_z(mm)	100
l(mm)	90,60,30
w(mm)	4

Figure 5.13 The field couplings at the origin versus frequency for a conducting circular cylinder perforated periodically with rectangular slots. The length of strips (*l*) is varied. A TE plane wave is normally incident ($\phi^{inc}=0^0$) and the scattered fields are computed at the origin (ρ=0) of the cylindrical structure.

—— *l*=90mm, - - - - *l*=60mm, ······ *l*=30mm.

5.4. Numerical results for the axial strips backed by a dielectric shell

Figure 5.14 gives the RCS of a dielectric shell covered periodically with infinitely long strips. The parameters assumed for the structure are given in the inset. The relative dielectric constant of the shell is denoted by ε_r. The plots are given for varying *N* values, where *N* denotes the number of strips around the cylinder. A TM polarized plane wave is normally incident ($\phi^{inc}=0^0$) on the structure and the observations are made in the back side (ϕ=180^0). For N=16, a weak resonance occurs near 1.5GHz but as N increases, the resonant frequency shifts toward higher frequencies and the resonances become deeper. At a resonant frequency, the fields due to the currents on the strip surfaces are cancelled by the fields due to the polarization currents inside the dielectric and so null fields are observed. When too much strips are placed on the dielectric shell (as in the case N=64), a resonance is not detected in the given frequency range. Possibly a resonance occurs at a higher frequency. The small ripples at the lower frequencies are due to TM cut-off frequencies of circular waveguide modes.

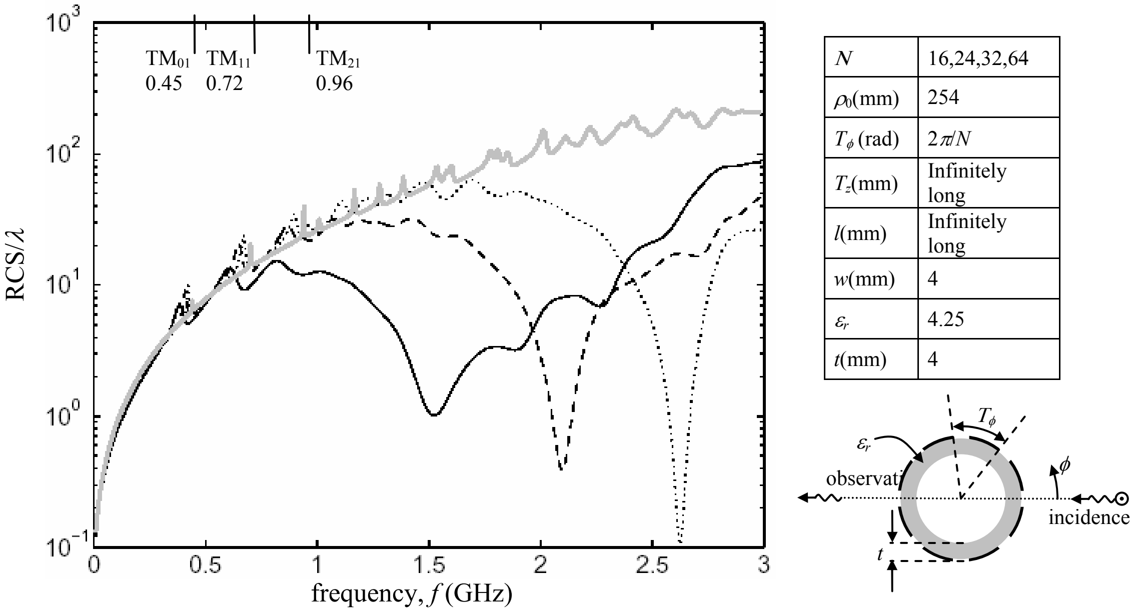

N	16,24,32,64
ρ_0(mm)	254
T_ϕ (rad)	$2\pi/N$
T_z(mm)	Infinitely long
l(mm)	Infinitely long
w(mm)	4
ε_r	4.25
t(mm)	4

Figure 5.14 RCS versus frequency for infinitely long strips located on a dielectric shell. The number of elements (N) in the circumferential direction is varied. A TM plane wave is normally incident (ϕ^{inc}=0^0) and the scattered fields are computed in the back side (ϕ=180^0) of the cylindrical structure.

—— N=16, - - - - N=24, ······ N=32, ▬ N=64.

The effects of the dielectric shell thickness (t) on the scattering characteristics of the cylindrical structure are visualized in Figure 5.15. The parameters of the problem are given in the inset. When obtaining the numerical results, the number of infinitely long strips is taken as N=32 but the shell thickness (t) is varied. As in the previous figure, a TM polarized plane wave is normally incident (ϕ^{inc}=0^0) on the cylindrical structure and the scattered fields are computed in the back side (ϕ=180^0) of the structure. The results show that the thickness of the dielectric shell affects the resonant frequencies at which the scattered field amplitudes vanish. The case *t*=0 in the figure corresponds to a plot given in Figure 5.6. As the thickness of the dielectric shell increases, a resonance occurs at a high frequency and move toward the lower frequencies. Specifically for the case *t*=4mm, a resonance occurs at 2.65GHz and the structure becomes almost invisible at that frequency. At lower frequencies, all plots are indistinguishable from each other. So the numerical results have shown that the thickness of the dielectric shell has no effect on the scattered field magnitudes at lower frequencies. The small ripples on the plots are close to the TM cut-off frequencies of circular waveguide modes.

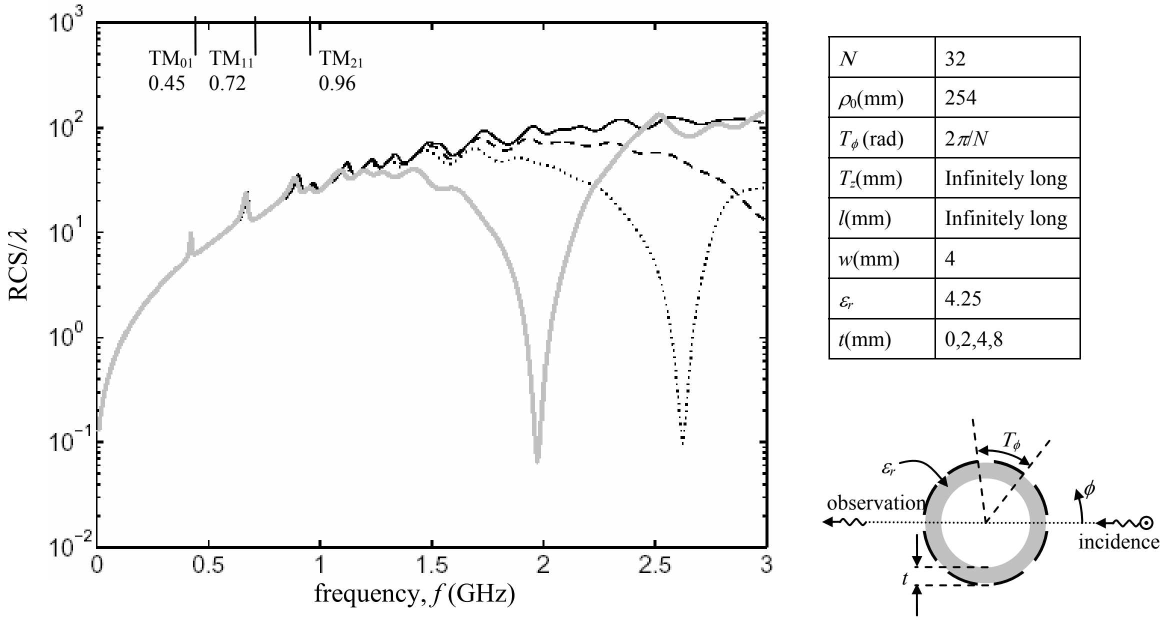

N	32
ρ_0(mm)	254
T_ϕ (rad)	$2\pi/N$
T_z(mm)	Infinitely long
l(mm)	Infinitely long
w(mm)	4
ε_r	4.25
t(mm)	0,2,4,8

Figure 5.15 RCS versus frequency for infinitely long strips located on a dielectric shell. The dielectric thickness (t) is varied and other parameters are as shown in the inset. A TM plane wave is normally incident ($\phi^{inc}=0^0$) and the scattered fields are computed in the back side ($\phi=180^0$) of the cylindrical structure.

—— t=0, - - - - t=2mm, ······ t=4mm, ▬ t=8mm.

In Figure 5.16, the plots are given for a case *t*=4mm but, the relative dielectric constant (ε_r) of the dielectric shell is varied. It is assumed that a TM polarized plane wave is normally incident ($\phi^{inc}=0^0$) on the cylindrical structure involving infinitely long strips and the RCS are determined in the back side ($\phi=180^0$) of the structure. Other parameters are as given in the inset. When the relative dielectric constant of the shell (ε_r) is greater than unity, the polarization currents in the dielectric makes additional radiation into the free-space and at a resonant frequency those fields cancel the fields radiated from the currents on the strips. The results show that the resonant frequencies are dependent on ε_r; as it increases, the resonances are shifted toward lower frequencies and become deeper. Specifically for ε_r =8.5, a resonance occurs at 1.8GHz and the structure becomes almost invisible. However at low frequencies, all plots are almost indistinguishable and it means the dielectric material has no influence at those frequencies. That has also been recognized from the plots given in the previous figures. The small ripples at the lower frequencies are close to the TM cut-off frequencies of circular waveguide modes.

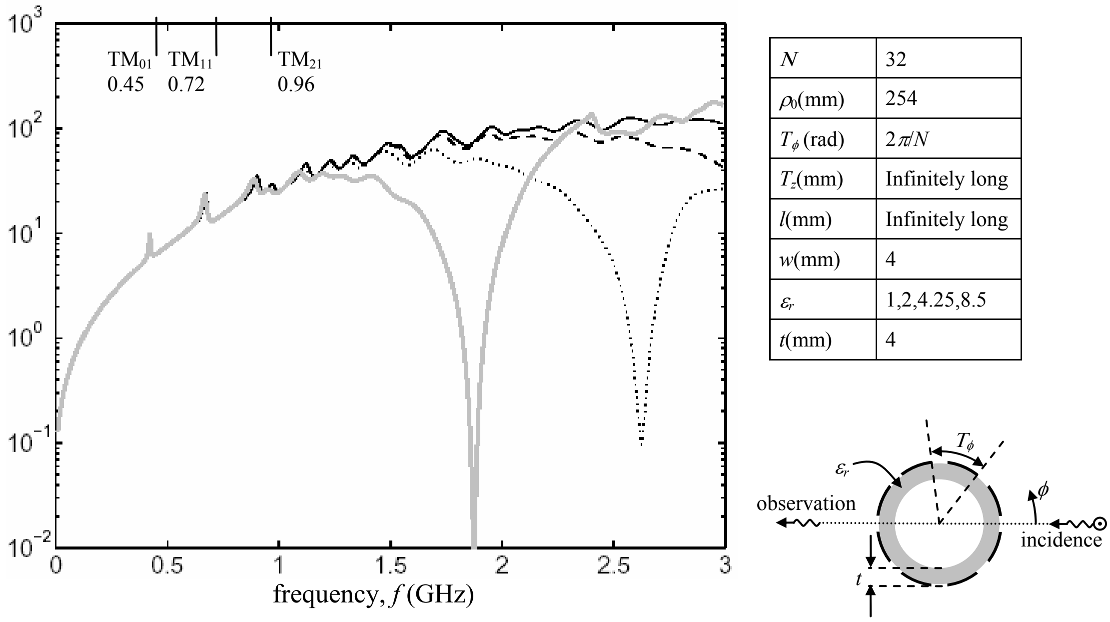

N	32
ρ_0(mm)	254
T_ϕ (rad)	$2\pi/N$
T_z(mm)	Infinitely long
l(mm)	Infinitely long
w(mm)	4
ε_r	1,2,4.25,8.5
t(mm)	4

Figure 5.16 RCS versus frequency for infinitely long strips located on a dielectric shell. The relative dielectric constant (ε_r) is varied and other parameters are as shown in the inset. A TM plane wave is normally incident ($\phi^{inc}=0^0$) and the scattered fields are computed in the back side ($\phi=180^0$) of the cylindrical structure.

—— ε_r =1, - - - - ε_r =2, ······ ε_r =4.25, —— ε_r =8.5.

The numerical results given in Figure 5.17 and Figure 5.18 are obtained for a case when the axial strips are of finite length. The RCS are plotted versus frequency for different values of the dielectric shell thickness (t). As in the previous figures, the cylindrical structure is illuminated by a normally incident TM polarized plane wave.

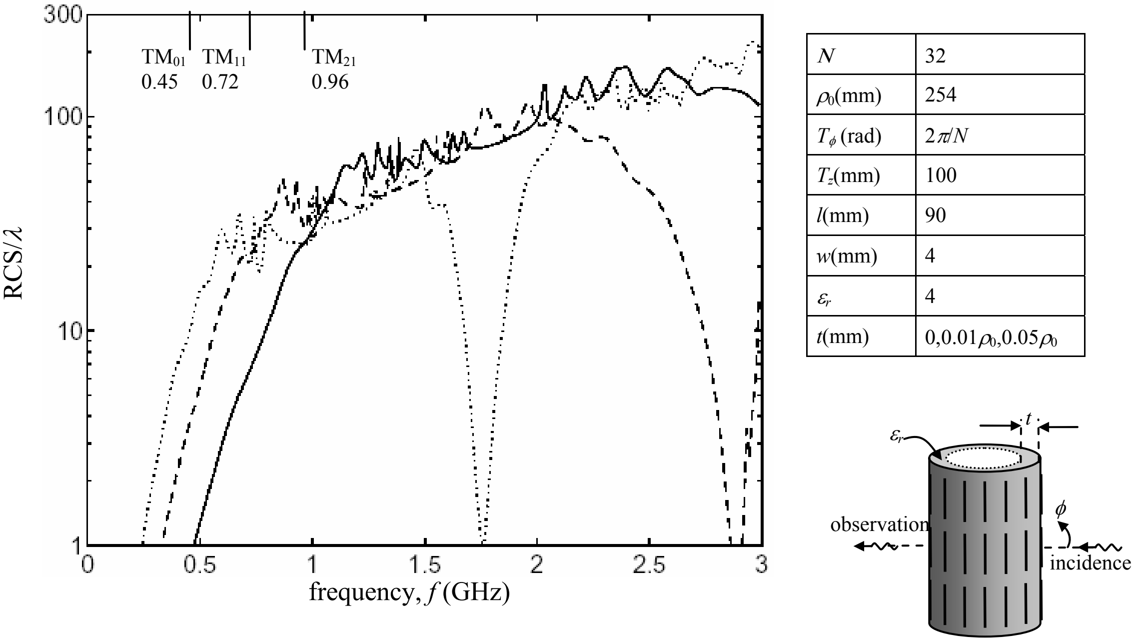

N	32
ρ_0(mm)	254
T_ϕ (rad)	$2\pi/N$
T_z(mm)	100
l(mm)	90
w(mm)	4
ε_r	4
t(mm)	$0, 0.01\rho_0, 0.05\rho_0$

Figure 5.17 RCS versus frequency for rectangular strips located on a dielectric shell. The dielectric thickness (t) is varied. A TM plane wave is normally incident ($\phi^{inc}=0^0$) and the scattered fields are computed in the back side ($\phi=180^0$) of the cylindrical structure.

—— $t=0$, - - - - $t=0.01\rho_0$, ⋯⋯ $t=0.05\rho_0$.

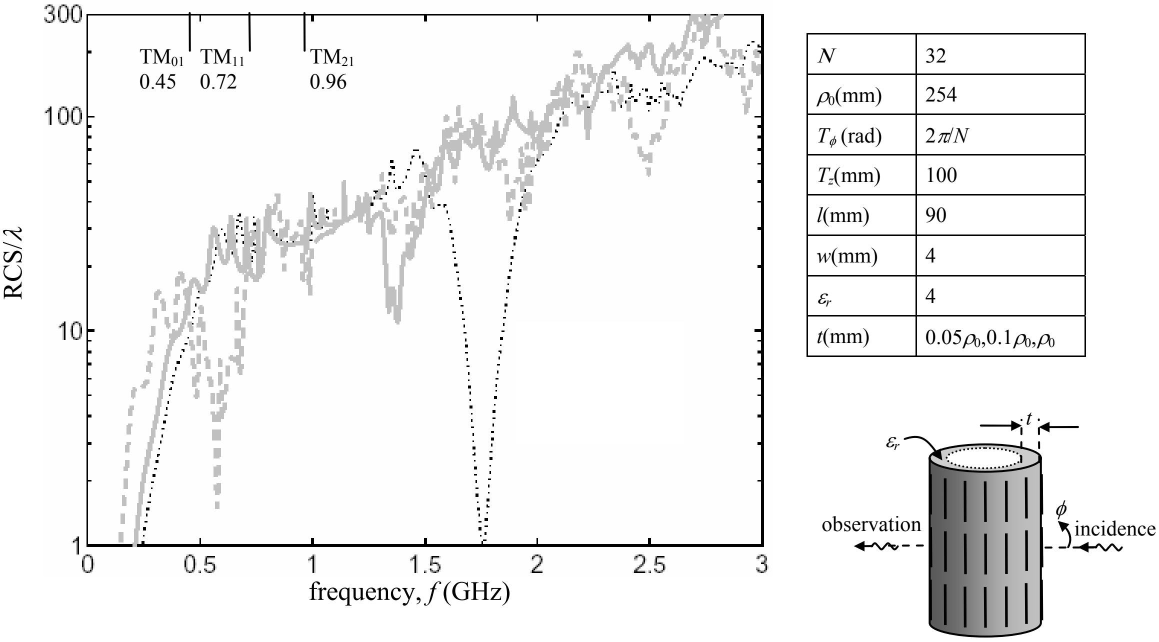

N	32
ρ_0(mm)	254
T_ϕ (rad)	$2\pi/N$
T_z(mm)	100
l(mm)	90
w(mm)	4
ε_r	4
t(mm)	$0.05\rho_0, 0.1\rho_0, \rho_0$

Figure 5.18 RCS of the structure considered in Figure 5.17 when the dielectric thickness (t) is further increased.

⋯⋯ $t=0.05\rho_0$, —— $t=0.1\rho_0$, - - - - $t=\rho_0$.

The scattered fields are computed in the back side (ϕ=180^0) of the structure. If the thickness of the dielectric shell is varied from 0 to 0.05ρ_0 as in Figure 5.17, the resonances become deeper and the resonant frequencies are shifted toward the lower frequencies. Specifically for t=0.05ρ_0 a resonance occurs at 1.76 GHz and the structure becomes almost invisible at that frequency. The resonances are due to the cancellations between the fields radiated from two different types of currents that are induced on the cylindrical structure: one is the polarization currents inside the dielectric shell and the other is the surface currents on the conducting strips. When the dielectric thickness is further increased, the resonances become weaker as shown by the plots in Figure 5.18. The plot for t=ρ_0 corresponds to a case when the inside of the cylindrical surface is completely filled with the dielectric material.

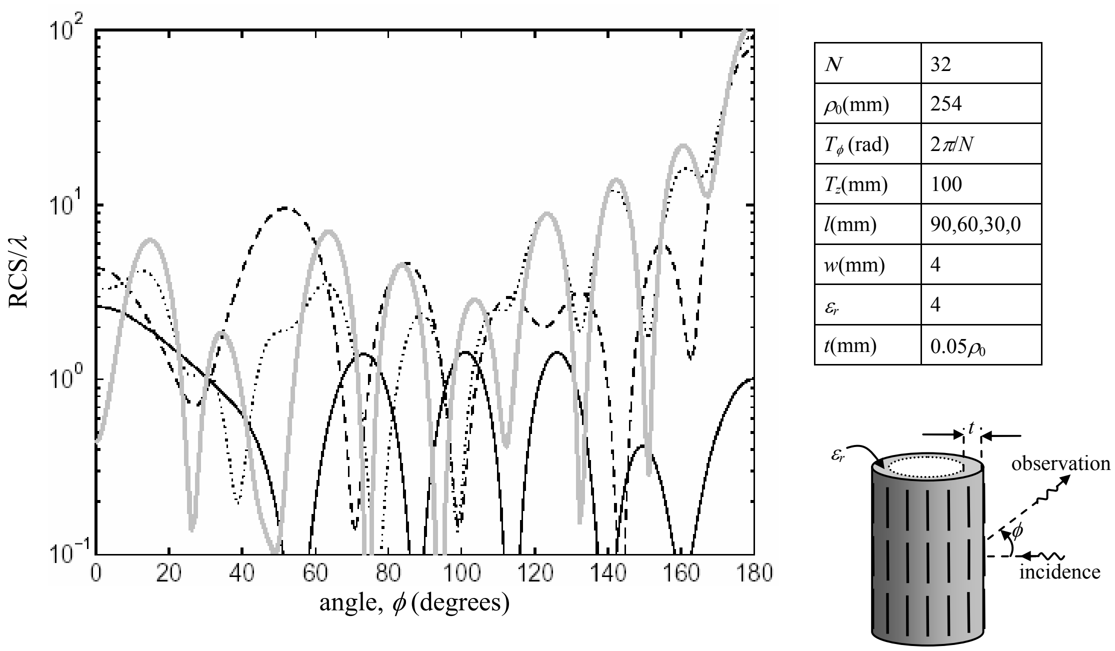

N	32
ρ_0(mm)	254
T_ϕ (rad)	$2\pi/N$
T_z(mm)	100
l(mm)	90,60,30,0
w(mm)	4
ε_r	4
t(mm)	0.05ρ_0

Figure 5.19 RCS versus observation angle (ϕ) for rectangular strips located on a dielectric shell. The length of strips (l) is varied and other parameters are as shown in the inset. A TM plane wave is normally incident (ϕ^{inc}=0^0) and the scattered fields are computed at the resonant frequency (f=1.76GHz) of Figure 5.18.

—— l=90mm, - - - - l=60mm, ······ l=30mm, —— l=0.

The RCS versus observation angle (ϕ) are plotted in Figure 5.19 for the case of t=0.05ρ_0, f=1.76 GHz. The other parameters of the cylindrical structure are given in the inset. The assumed parameters correspond to the case where the strong resonance in Figure 5.18 occurred at 1.76GHz. The plots are given for decreasing lengths of strip (l). As l decreases, the total scattered field amplitudes increase in average. However the currents induced on the strips become weaker as l shrinks. So the fields radiated from the strips can not cancel the fields radiated from the polarization currents inside the dielectric shell and the resultant effect is observed as a net increase in RCS. The plot for the case l=0 corresponds to the RCS of a dielectric shell having no strips on its surface. It is interesting to note that the two plots namely for the cases l=0 and l=30mm almost coincide in the shadow region of the cylindrical structure (between 120^0 and 180^0). It is also remarkable that when l=90mm there exists some angles regularly spaced along the ϕ-axis at which the surface becomes almost invisible.

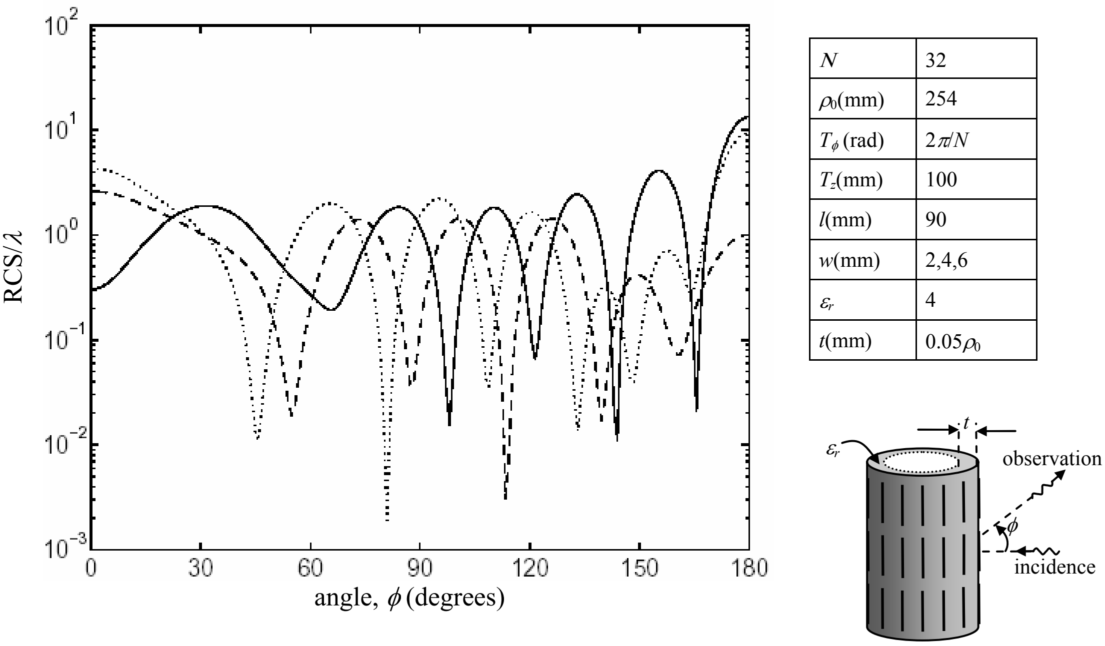

N	32
ρ_0(mm)	254
T_ϕ (rad)	$2\pi/N$
T_z(mm)	100
l(mm)	90
w(mm)	2,4,6
ε_r	4
t(mm)	$0.05\rho_0$

Figure 5.20 RCS versus observation angle (ϕ) for rectangular strips located on a dielectric shell. The width of strips (w) is varied and other parameters are as shown in the inset. A TM plane wave is normally incident ($\phi^{inc}=0^0$) and the scattered fields are computed at the resonant frequency (f=1.76GHz) of Figure 5.18.

—— w=2mm, - - - - w=4mm, …… w=6mm.

In Figure 5.20, the effect of the width on the RCS is investigated. The RCS are plotted versus observation angle ϕ, for the case $t=0.05\rho_0$, f=1.76GHz, and l=90mm. The plot for w=4mm corresponds to the case, where the strong resonance occurs in Figure 5.18. The numerical results reveal that if the strip width is varied (that is: if $w \neq 4$ mm), the scattered field amplitudes increase in average. It is since; a variation in w causes variations on the currents induced on the strips. As a result, the above-mentioned cancellation phenomenon between the fields radiated from the polarization currents inside the dielectric shell and the fields radiated from the strip currents are broken down. Thus the RCS increases if the widths (w) of the strips are decreased or increased.

It is noticed from the numerical results that the dielectric shell thickness (t) also influences the RCS. Plots of the RCS in Figure 5.21 are given versus observation angle ϕ for the case w=4mm, f=1.76GHz, and l=90mm as the shell thickness changes. The parameters are chosen to reflect the resonance at 1.76GHz in Figure 5.18 ($t=0.05\rho_0$). The plots reveal that if the dielectric thickness is varied, the total scattered field amplitudes increase in average. It is since, changes in the dielectric thickness causes variations in the polarization currents inside the dielectric and so the cancellation phenomenon discussed in the preceding figures is broken down. As a result, the RCS increases if the dielectric shell thickness is decreased or increased.

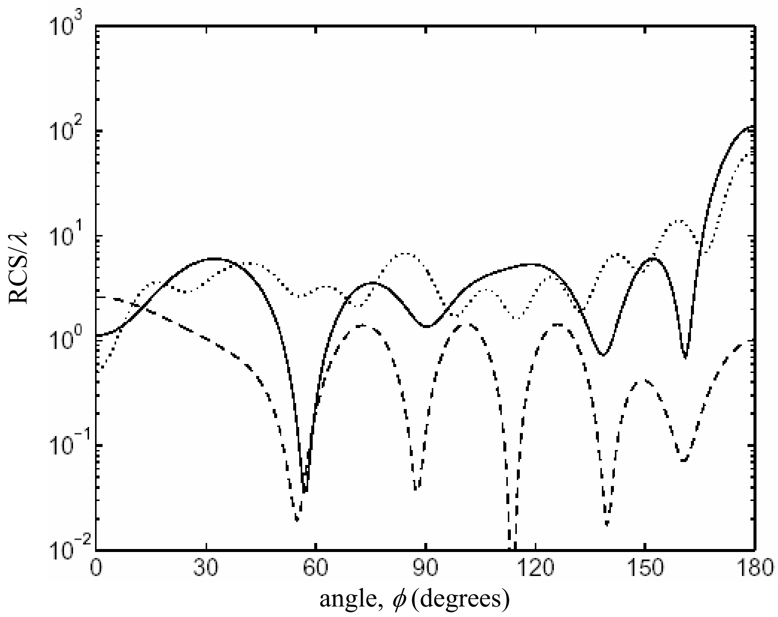

N	32
ρ_0(mm)	254
T_ϕ (rad)	$2\pi/N$
T_z(mm)	100
l(mm)	90
w(mm)	4
ε_r	4
t(mm)	$0.01\rho_0, 0.05\rho_0, 0.1\rho_0$

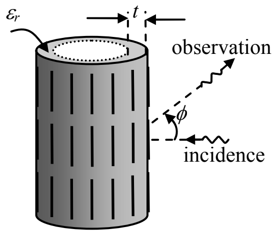

Figure 5.21 RCS versus observation angle (ϕ) for rectangular strips located on a dielectric shell. The dielectric thickness (t) is varied. A TM plane wave is normally incident ($\phi^{inc}=0^0$) and the scattered fields are computed at the resonant frequency (f=1.76GHz) of Figure 5.18.

—— $t=0.01\rho_0$, - - - - $t=0.05\rho_0$, ······ $t=0.1\rho_0$.

The plots given in Figure 5.22 show that the resonant frequencies are changed if the number of strips in the circumferential direction (N) is varied. It is assumed that a

TM polarized plane wave is normally incident ($\phi^{inc}=0^0$) on the cylindrical structure and the scattered fields are computed in the back side ($\phi=180^0$) of structure. No resonances are detected and a smooth curve is obtained when there are no strips. The other plots reveal that as N is increased, the resonant frequencies are shifted from lower to higher frequencies. Specifically for N=32, the resonance occurs at 1.76 GHz and the structure becomes almost invisible at that frequency. However, a clear resonance is not detected when N=8. It is recognized that the fields radiated from the currents on the strips for the case N=8 are so weak that they can not cancel the fields radiated from the polarization currents inside the dielectric shell.

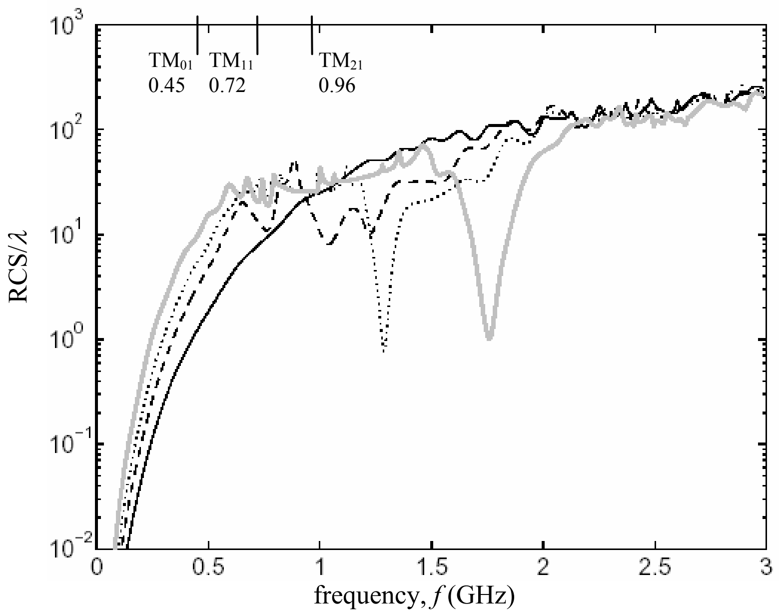

N	0,8,16,32
ρ_0(mm)	254
T_ϕ (rad)	$2\pi/N$
T_z(mm)	100
l(mm)	90
w(mm)	4
ε_r	4
t(mm)	$0.05\rho_0$

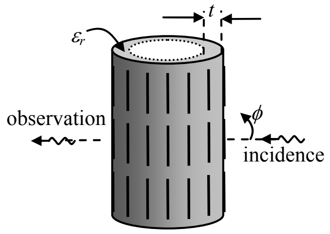

Figure 5.22 RCS versus frequency for rectangular strips located on a dielectric shell. The number of elements (N) in the circumferential direction is varied. A TM plane wave is normally incident ($\phi^{inc}=0^0$) and the scattered fields are computed in the back side ($\phi=180^0$) of the cylindrical structure.

—— without strips, - - - - N=8, ······ N=16, —— N=32.

In Figure 5.23, the effects of small variations in the strip lengths (l) are illustrated. RCS are plotted versus frequency for the case when a TM polarized plane wave is normally incident ($\phi^{inc}=0^0$) on the cylindrical structure and the scattered fields are observed in the back side ($\phi=180^0$) of the structure. The plots reveal that a change in the strip length causes a shift in the resonance frequency: if the strip length is increased, the resonance occurs at a lower frequency. In addition, the scattered field amplitudes are raised at low frequencies.

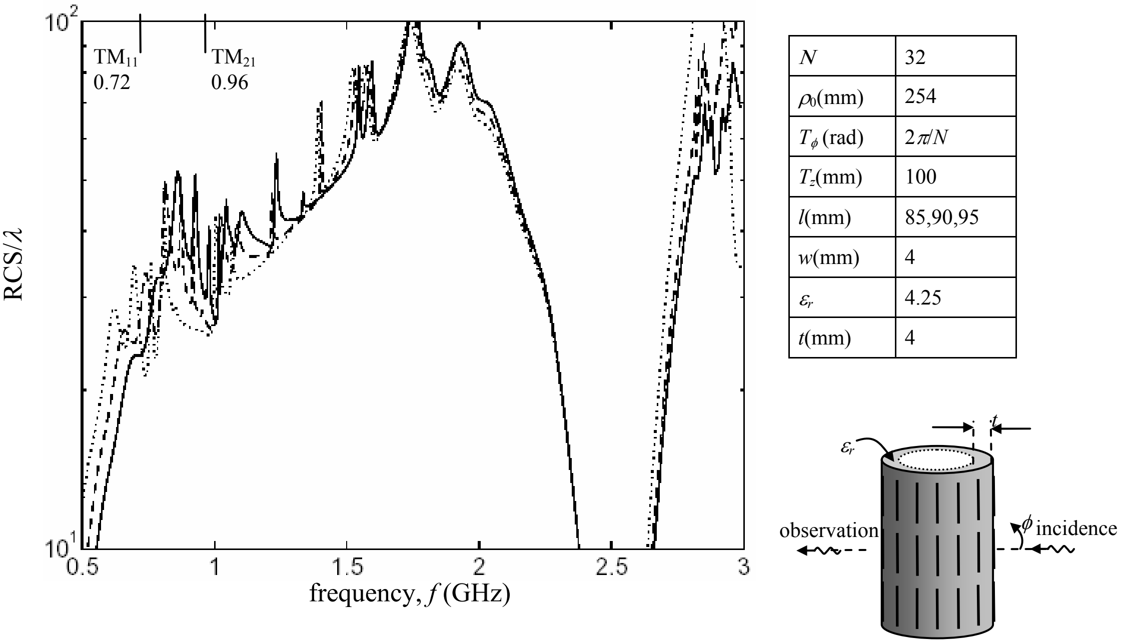

N	32
ρ_0(mm)	254
T_ϕ (rad)	$2\pi/N$
T_z(mm)	100
l(mm)	85,90,95
w(mm)	4
ε_r	4.25
t(mm)	4

Figure 5.23 RCS versus frequency for rectangular strips located on a dielectric shell. The length of strips (l) is varied. A TM plane wave is normally incident (ϕ^{inc}=0^0) and the scattered fields are computed in the back side (ϕ=180^0) of the cylindrical structure.

—— l=85mm, - - - - l=90mm, ······ l=95mm.

Figure 5.24 shows the variation of RCS as the incidence angle (ϕ^{inc}) is varied. The observation angles (ϕ) are measured from the incidence direction of the plane wave such that the directions ϕ=0^0 and ϕ=180^0 respectively correspond to the front side (ϕ^{inc}) and the back side (180^0+ϕ^{inc}) of the cylindrical structure. The number of strips (N) in the circumferential direction is 20 and the frequency is 1.76GHz. The other parameters of the cylindrical structure are as given in the inset. The incidence angle of the plane wave is varied from 0^0 to $0.5T_\phi$, where T_ϕ denotes the periodicity in the circumferential direction: T_ϕ=$2\pi/N$=18^0. For the case ϕ^{inc} =$0.5T_\phi$, the cylindrical structure becomes invisible near the observation angles at ϕ=10^0 and ϕ=70^0. The plots reveal that the scattered field amplitudes in the shadow region of the cylindrical structure are not affected (for ϕ>120^0) as the angle of incidence changes.

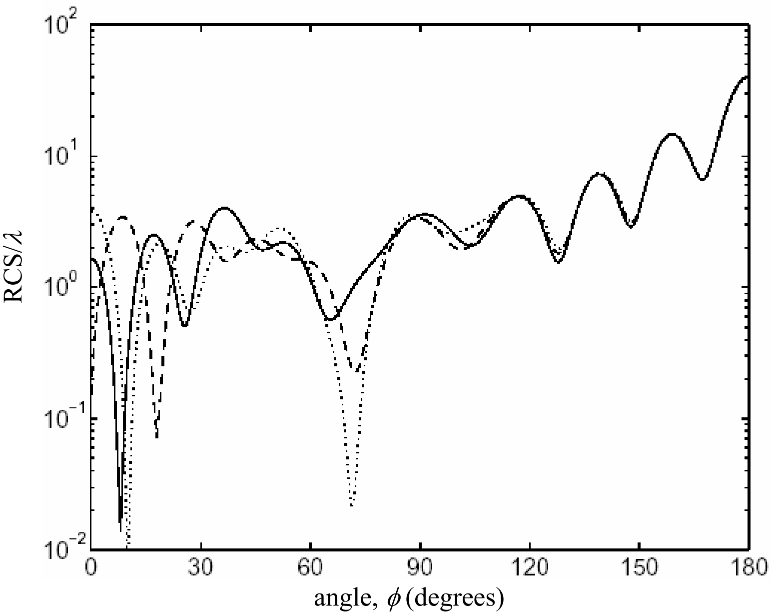

N	20
ρ_0(mm)	254
T_ϕ (rad)	$2\pi/N$
T_z(mm)	100
l(mm)	90
w(mm)	4
ε_r	4
t(mm)	$0.05\rho_0$

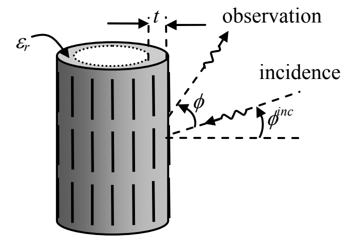

Figure 5.24 RCS versus observation angle (ϕ) for rectangular strips located on a dielectric shell. The circumferential angle of incidence (ϕ^{inc}) is varied. The number of elements (N) in the circumferential direction is 20. The scattered fields are computed at the resonant frequency (f=1.76GHz) of Figure 5.18.

—— $\phi^{inc}=0$, - - - - $\phi^{inc}=0.25T_\phi$, …… $\phi^{inc}=0.5T_\phi$.

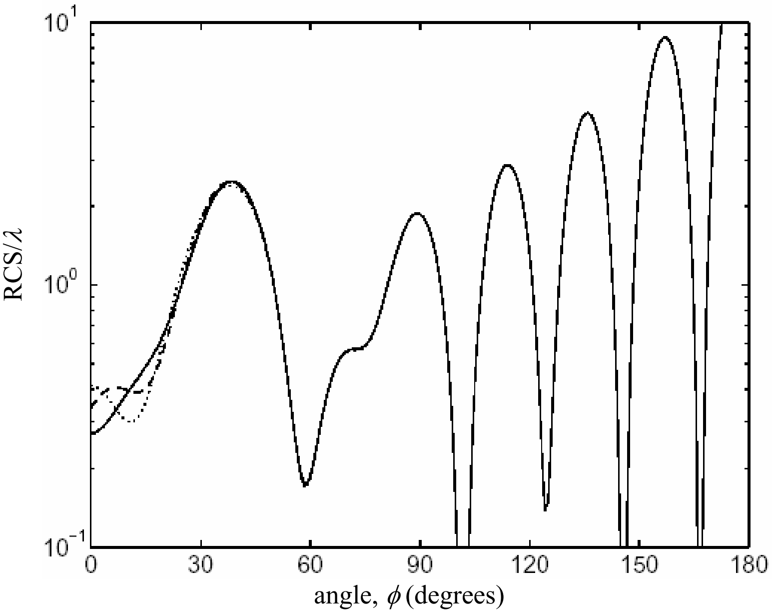

N	26
ρ_0(mm)	254
T_ϕ (rad)	$2\pi/N$
T_z(mm)	100
l(mm)	90
w(mm)	4
ε_r	4
t(mm)	$0.05\rho_0$

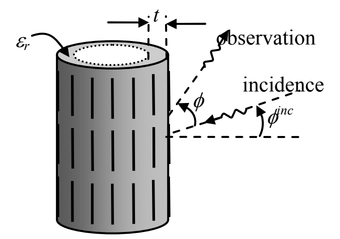

Figure 5.25 RCS of the structure considered in Figure 5.24 when the number of elements in the circumferential direction is increased (N=26).

—— $\phi^{inc}=0$, - - - - $\phi^{inc}=0.25T_\phi$, …… $\phi^{inc}=0.5\,T_\phi$.

In the case of oblique incidence numerical investigations have revealed that if the number of strips in the circumferential (N) direction is large enough (such as if N>26), the incidence angle (ϕ^{inc}) becomes insignificant. This is demonstrated in Figure 5.25, where N=26 and the frequency is 1.76GHz. The radius of the structure is (ρ_0=254mm). The plots show that the scattered fields are not affected with the variations in the incidence angle.

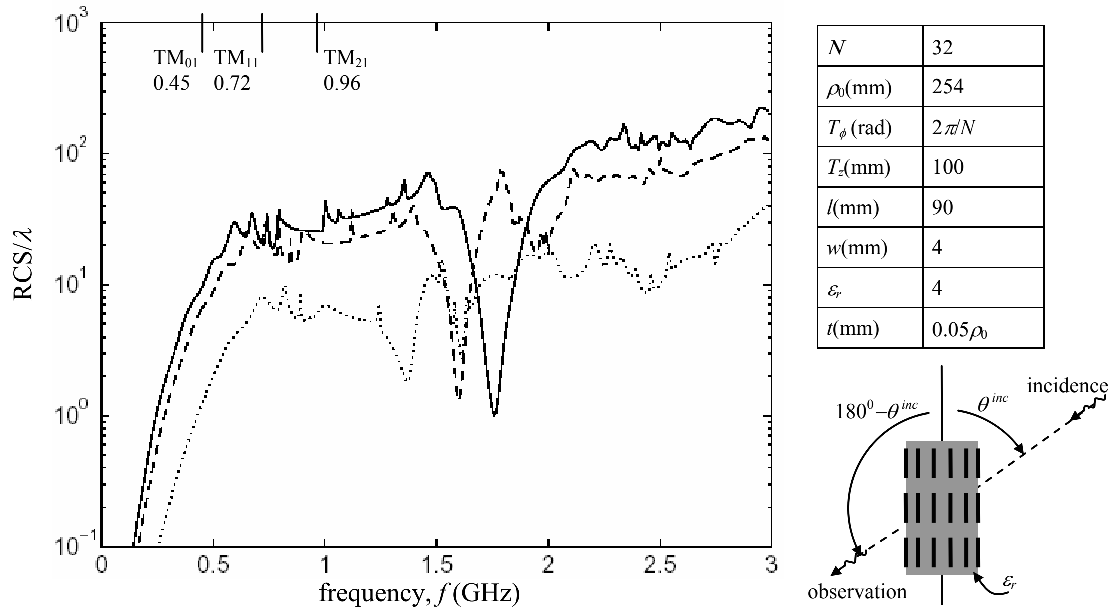

N	32
ρ_0(mm)	254
T_ϕ (rad)	$2\pi/N$
T_z(mm)	100
l(mm)	90
w(mm)	4
ε_r	4
t(mm)	$0.05\rho_0$

Figure 5.26 RCS versus frequency for rectangular strips located on a dielectric shell. The elevation angle of incidence (θ^{inc}) is varied. The scattered fields are computed in the back side (θ=180^0−θ^{inc}; ϕ=180^0) of the cylindrical structure.

—— θ^{inc} =90^0, - - - - θ^{inc} =60^0, ⋯⋯ θ^{inc} =30^0.

In the figures given so far, plane waves are assumed to be incident on the cylindrical structures in directions perpendicular to the z axis (on x-y plane) and the scattered fields are observed on the same plane. Those directions correspond to an elevation angle 90^0 for both the incident waves and the scattered waves. Variation of RCS versus incidence angle (θ^{inc}) is given in Figure 5.26. The observation angles (θ) in that cases are aligned at θ=180^0−θ^{inc}. Moreover the scattered fields are computed in the back side of the cylindrical structure (ϕ=180^0). The data of the problem is given in the inset. The plots reveal that if the angle θ is decreased, the resonance at the frequency 1.76GHz shifts toward lower frequencies. Furthermore, the scattered fields' amplitudes are typically decreased in the frequency range from 0 to 3GHz.

Such an assessment is also detected in Figure 5.27, where the RCS are computed in the front side (ϕ=0^0) of the same structure. The plots in that figure are very oscillatory on the high frequency portion.

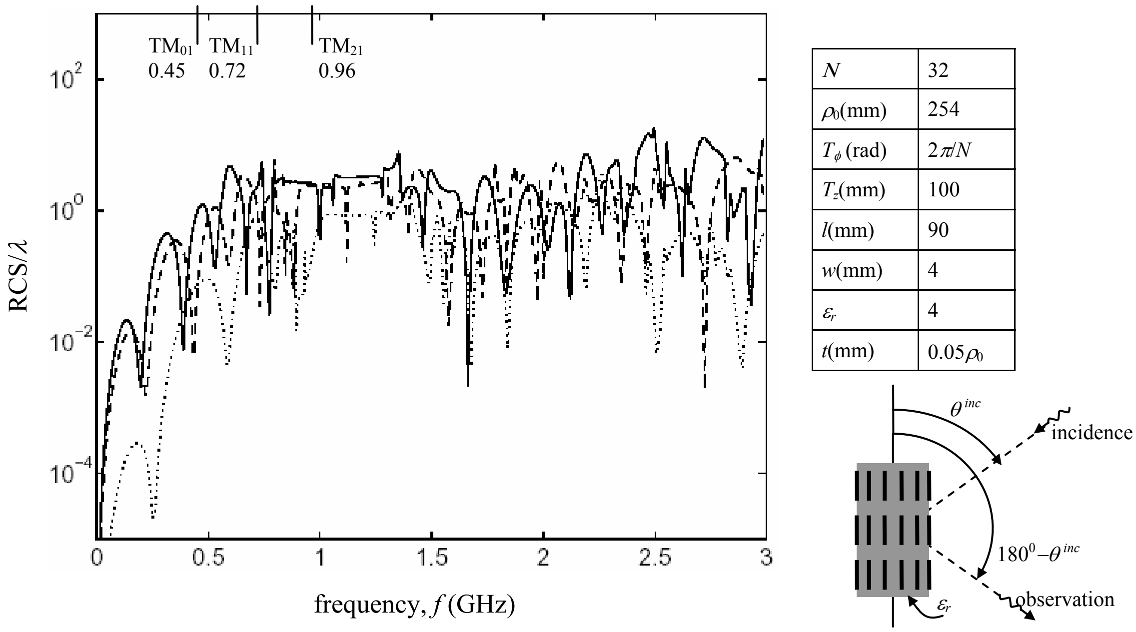

N	32
ρ_0(mm)	254
T_ϕ (rad)	$2\pi/N$
T_z(mm)	100
l(mm)	90
w(mm)	4
ε_r	4
t(mm)	$0.05\rho_0$

Figure 5.27 RCS of the structure considered in Figure 5.26 when scattered fields are computed in the front side (θ=180^0–θ^{inc}; ϕ= 0^0) of the cylindrical structure.
—— θ^{inc} =90 degrees, - - - - θ^{inc} =60 degrees, …… θ^{inc} =30 degrees.

The numerical results on the electromagnetic field penetrations (the couplings) into a dielectric shell covered with the strips are given in Figure 5.28. It is assumed that a TM polarized plane wave is normally incident (θ^{inc}=90^0; ϕ^{inc}=0^0) on the cylindrical structure and the scattered fields are computed at the origin (ρ=0) of the structure. The dielectric thickness (t) is varied and the other parameters of the structure are as given in the inset. Note that the t=0 corresponds to the free-standing strips case, which was previously considered (namely, it corresponds to a plot given in Figure 5.10). When t=0, the fields inside the cylindrical structure almost vanishes at a resonant frequency 1.82GHz. It is recognized that the incident fields and the scattered fields cancel themselves at that frequency. As the shell thickness is increased the resonance at 1.82GHz disappears and the plots become smoother. However, very sharp ripples are detected in the vicinity of 1GHz. Those ripples may be due to the TM cut-off frequencies of circular waveguide modes. Note that, the two cut-off frequencies (at 0.96GHz and 1.04GHz) corresponding to the modes TM$_{21}$ and

TM_{02} are very close to each other and so the remarkable ripples are possibly due to that proximity.

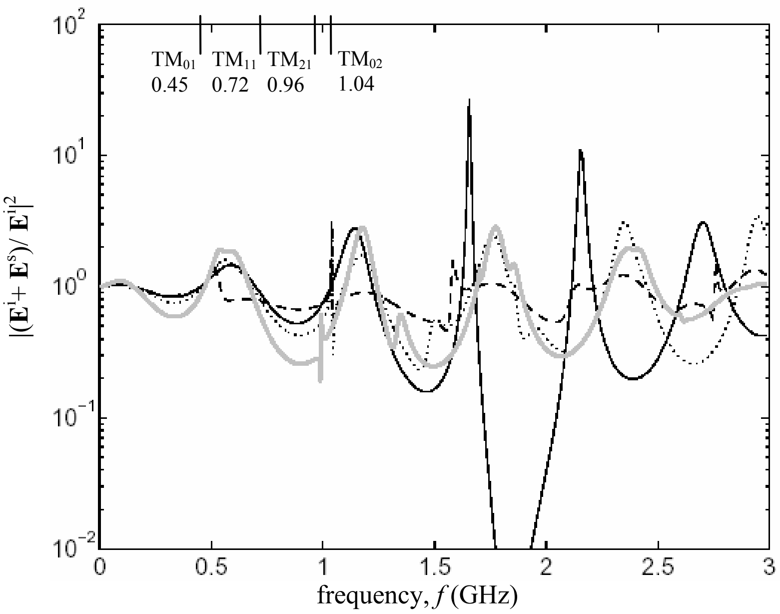

N	32
ρ_0(mm)	254
T_ϕ (rad)	$2\pi/N$
T_z(mm)	100
l(mm)	90
w(mm)	4
ε_r	4
t(mm)	$0, 0.01\rho_0, 0.05\rho_0, 0.1\rho_0$

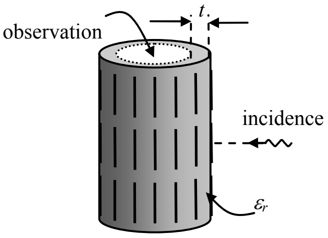

Figure 5.28 The field couplings at the origin versus frequency for rectangular strips located on a dielectric shell. The dielectric thickness (t) is varied. A TM plane wave is normally incident ($\phi^{inc}=0^0$) and the scattered fields are computed at the origin ($\rho=0$) of the cylindrical structure.

—— $t=0$, - - - - $t=0.01\rho_0$, ······ $t=0.05\rho_0$, —— $t=0.1\rho_0$.

When the elevation angle of the incident wave (θ^{inc}) is varied, the couplings are plotted as shown in Figure 5.29. The shell thickness is fixed ($t=0.05\rho_0$) and the scattered fields are computed at the origin ($\rho=0$) of the structure. The other parameters of the structure are the same as in the previous figure. While the incidence angle varies from $\theta^{inc}=90^0$ to $\theta^{inc}=60^0$, the sharp ripples are shifted toward higher frequencies. But if the incidence angle is further decreased (namely for $\theta^{inc}=30^0$ case), the coupling approaches unity and the sharp spikes are not detected.

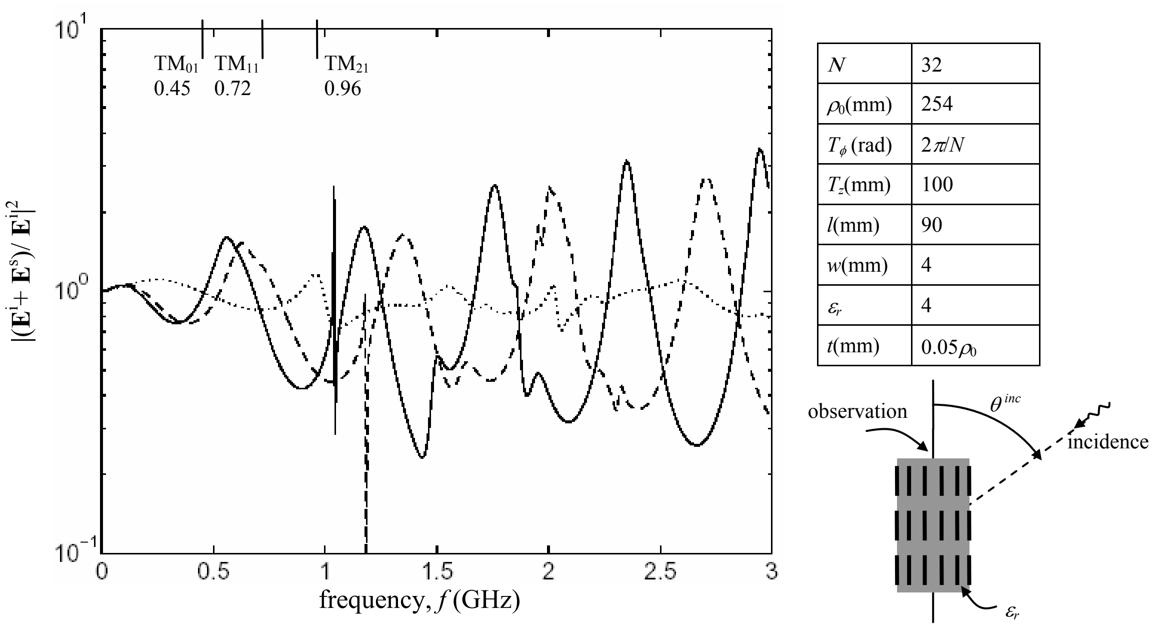

N	32
ρ_0(mm)	254
T_ϕ (rad)	$2\pi/N$
T_z(mm)	100
l(mm)	90
w(mm)	4
ε_r	4
t(mm)	$0.05\rho_0$

Figure 5.29 The field couplings at the origin versus frequency for rectangular strips located on a dielectric shell. The elevation angle of incidence (θ^{inc}) is varied. The scattered fields are computed at the origin (ρ=0) of the cylindrical structure.

—— θ^{inc}=90 degrees, - - - - θ^{inc}=60 degrees, …… θ^{inc}=30 degrees.

6. CONCLUSION

6.1. Conclusions on the numerical result

Numerical results are obtained by using entire domain basis functions in MM solutions. The resulting slowly convergent infinite sums are accelerated. An important parameter in scattering studies is the electromagnetic scattering by a target which is usually represented by its radar cross section (RCS). The RCS is defined as "the area intercepting the amount of power that, when scattered isotropically, produces at the receiver a density that is equal to the density scattered by the actual target" [23]. Another important parameter for the cylindrical structures is the electromagnetic field couplings into the cylindrical structures. The coupling is defined as the total power measured at the center of a cylindrical structure when a plane wave is incident on the structure. So, the couplings and the RCS are determined for several types of cylindrical structures and the numerical results are given in Chapter 5. The numerical analyses have shown that:

In free-standing rectangular strips structures, the scattered field magnitudes are seen to be dependent on the surface periodicities and the strip dimensions. As the strip length decreases, the magnitudes of the induced currents decrease as well and that causes reductions on the scattered field amplitudes. Some weak resonances are detected near the TM cut-off frequencies of circular waveguide modes. Amplitudes of the scattered fields in the front side of the structure are seen to be very small and fluctuating when compared with those in the back side.

For cylindrical structures involving a conducting cylinder perforated by the rectangular slots, resonances are detected at some specific frequencies. Close to such a frequency the structure becomes almost invisible. A resonance occurs when the far fields radiated by the "magnetic currents" flowing on the slotted regions of the cylinder are cancelled by the fields due to the "electric currents" flowing on the conducting parts of the cylinder. Such a property of the slotted cylinder may be very useful in radar applications. Amplitudes of the scattered fields in the front side of the structure are seen to be very small and fluctuating when compared with those in the back side. The resonant frequencies depend on the slot length and the curvature of the cylindrical surface. On the other hand, the resonant frequencies of planar structures involving periodically located slots are dependent on the length of slots.

The numerical analysis on dielectric shell structures that are covered periodically with the rectangular strips have shown that the scattered filed amplitudes vanish at some resonant frequencies. The resonances occur when the fields due to the currents on the strip surfaces are cancelled by the fields due to the polarization currents inside the dielectric. By the way null fields are observed at a resonant frequency. The resonant frequencies are seen to be dependent on many parameters of the structure such as the dielectric constant of the shell, the shell thickness, the strip dimensions, the incident angle of an exciting wave etc. As the dielectric constant of the shell increase, the resonances are shifted toward lower frequencies. But if the strip length is decreased, the resonances are shifted toward lower frequencies. It is also seen that if the number of strips in the circumferential (N) direction is large enough (such as if $N>26$), the scattered fields are not affected from the variations of the circumferential angle of incidence.

6.2. Future Work

In this study, we considered a simple dielectric shell inside a cylindrical structure. However, the formulations given in this dissertation can be easily extended to analyze multiple concentric shells made up of different dielectric materials. Furthermore, the problems involving lossy dielectrics or anisotropic materials such as a chiral material can also be investigated after some modifications in the formulation.

Numerical results require computations of slowly convergent infinite sums as discussed in this study. Here the acceleration method is applied to the formulation involving narrow rectangular strips. As a future work one should attempt to apply the acceleration techniques to other geometries such as conducting patches.

APPENDIX A. THE CONVERGENCE ACCELERATION OF SLOWLY CONVERGENT INFINITE SUMS INVOLVING OSCILLATING TERMS

In this appendix, an acceleration technique based on a Kummer's transformation method is developed for some kind of slowly convergent sums. An infinite sum is decomposed into two parts; one part being rapidly convergent and the other part being slowly convergent. Then the sum in the slowly convergent part is expressed as integrals of some auxiliary functions and subsequently they are written in terms of polynomials whose coefficients are given by the zeta functions. The given method is very general and does not involve too much analytic effort. A numerical example is provided to illustrate the usage and the efficiency of the method.

The MM solutions of Chapter 3 yield slowly convergent infinite sums of the form

$$I = \frac{jw^2}{\pi N \rho_0^2 T_\phi} \sum_{m=-\infty}^{\infty} \frac{\sin^2\big((r+m)\pi w/b\big)}{(\pi w/b)^2 \, |\, r+m\,|^3}, \; -1 < r < 1, \tag{A.1}$$

where $r = v_0 / N$. The constants N, v_0 , b, w, ρ_0, and T_ϕ are as seen in the unit cell of the problem in Figure 3.1.b. Direct computations has shown that the series in (A.1) converges slowly for small values of $\pi w/b$. Particularly, in the limiting case $\pi w / b \to 0$, the series is divergent. However, the sum can be decomposed into rapidly convergent sums by applying a Kummer's acceleration method as in [18, 21]. In this manuscript, we consider more general sums and develop a computation scheme. At the end, computations of the sum in (A.1) are provided in a numerical example.

The method that will be given is a generalization of a method discussed by Flojolet et. al. [26]. According to [26] one can write

$$\sum_{n=1}^{\infty} f_n = \sum_{n=1}^{\infty} \left(f_n - \sum_{m=2}^{M} c_m (1/n)^m \right) + \sum_{m=2}^{M} c_m \zeta(m), \tag{A.2}$$

where $\zeta(m)$ denote the values of the zeta function at the integers, c_m denote the power series coefficient of f_n when it is expanded into inverse powers of n. The coefficients f_n in the original sum (A.2) is assumed to be such that $f_n \to 0$ and $nf_n \to 0$ as $n \to \infty$. The series on the left hand side of (A.2) may or may not be slowly convergent but, the one on the right hand side is, evidently, a rapidly convergent series. Such an expression is very useful for the computation once the values of the zeta function are available from a table. However, the difficulties may be encountered in finding the power series coefficient of f_n.

As in [21], we extend this method to the sums of the form

$$S(\alpha) = \sum_{n=1}^{\infty} e^{in\alpha} f_n \,, \tag{A.3}$$

where α denotes a real variable $f_n \to 0$ as $n \to \infty$. The sum in (A.1) can be expressed in terms of the sums of the form (A.3) as follows

$$\begin{aligned}
&\sum_{m=-\infty}^{\infty} \frac{\sin^2\left((r+m)\pi w/b\right)}{(\pi w/b)^2\,|r+m|^3} \\
&= \frac{\sin^2\left(r\pi w/b\right)}{(\pi w/b)^2\,|r|^3} + \sum_{n=1}^{\infty} \frac{\sin^2\left((r+n)\pi w/b\right)}{(\pi w/b)^2\,|r+n|^3} + \sum_{n=1}^{\infty} \frac{\sin^2\left((r-n)\pi w/b\right)}{(\pi w/b)^2\,|r-n|^3} \\
&= \frac{\sin^2\left(r\pi w/b\right)}{(\pi w/b)^2\,|r|^3} + \sum_{n=1}^{\infty} \frac{\sin^2\left((n+r)\pi w/b\right)}{(\pi w/b)^2 (n+r)^3} + \sum_{n=1}^{\infty} \frac{\sin^2\left((n-r)\pi w/b\right)}{(\pi w/b)^2 (n-r)^3} \\
&= \frac{\sin^2\left(r\pi w/b\right)}{(\pi w/b)^2\,|r|^3} + \frac{2}{(2\pi w/b)^2} \sum_{n=1}^{\infty} \left\{ \frac{1-\cos\left\{(n+r)2\pi w/b\right\}}{(n+r)^3} + \frac{1-\cos\left\{(n-r)2\pi w/b\right\}}{(n-r)^3} \right\} \\
&= \frac{\sin^2\left(r\pi w/b\right)}{(\pi w/b)^2\,|r|^3} + \frac{2}{x^2} \sum_{n=1}^{\infty} \left\{ \frac{1-\cos\left\{(n+r)x\right\}}{(n+r)^3} + \frac{1-\cos\left\{(n-r)x\right\}}{(n-r)^3} \right\} \\
&= \frac{\sin^2\left(r\pi w/b\right)}{(\pi w/b)^2\,|r|^3} + \frac{2}{x^2} \sum_{n=1}^{\infty} \left\{ \frac{1-\operatorname{Re} e^{jrx} e^{jnx}}{(n+r)^3} + \frac{1-\operatorname{Re} e^{-jrx} e^{jnx}}{(n-r)^3} \right\} \\
&= \frac{\sin^2\left(r\pi w/b\right)}{(\pi w/b)^2\,|r|^3} + \frac{2}{x^2} \sum_{n=1}^{\infty} \left\{ \frac{1-\operatorname{Re} e^{jrx} e^{jnx}}{(n+r)^3} - \frac{1-\operatorname{Re} e^{-jrx} e^{jnx}}{(-n+r)^3} \right\} \\
&= \frac{\sin^2\left(r\pi w/b\right)}{(\pi w/b)^2\,|r|^3} + \frac{2}{x^2} \sum_{n=1}^{\infty} \left\{ f_n - \operatorname{Re} e^{jrx} e^{jnx} f_n - f_{-n} + \operatorname{Re} e^{-jrx} e^{jnx} f_{-n} \right\} \\
&= \frac{\sin^2\left(r\pi w/b\right)}{(\pi w/b)^2\,|r|^3} + \frac{2}{x^2} \left\{ \sum_{n=1}^{\infty} f_n - \operatorname{Re} e^{jrx} \sum_{n=1}^{\infty} e^{jnx} f_n - \sum_{n=1}^{\infty} f_{-n} + \operatorname{Re} e^{-jrx} \sum_{n=1}^{\infty} e^{jnx} f_{-n} \right\}
\end{aligned}$$

$$
=\frac{\sin^2\left(r\pi w/b\right)}{(\pi w/b)^2\,|\,r\,|^3}+\frac{2}{x^2}\left\{I^+ + I^-\right\}, \tag{A.4}
$$

where

$$
I^+ = \sum_{n=1}^{\infty} f_n - \operatorname{Re} e^{jrx}\sum_{n=1}^{\infty} e^{jnx} f_n\,, \tag{A.5}
$$

$$
I^- = -\sum_{n=1}^{\infty} f_{-n} + \operatorname{Re} e^{-jrx}\sum_{n=1}^{\infty} e^{jnx} f_{-n}\,, \tag{A.6}
$$

$$
x = 2\pi w/b\,, \tag{A.7}
$$

$$
f_n = \frac{1}{(n+r)^3}\,. \tag{A.8}
$$

In deed, lots of sums can be represented in the form (A.3), for example a Fourier series

$$
N(x) = \frac{a_0}{2} + \sum_{n=1}^{\infty} a_n \cos nx + \sum_{n=1}^{\infty} b_n \sin nx\,, \tag{A.9}
$$

can be re-expressed as

$$
N(x) = \frac{a_0}{2} + \frac{1}{2}\sum_{n=1}^{\infty} e^{inx} f_n + \frac{1}{2}\sum_{n=1}^{\infty} e^{-inx} g_n\ ;\ f_n = a_n - ib_n,\ g_n = a_n + ib_n\,. \tag{A.10}
$$

In order to compute an infinite sum of the form (A.3) easily, a computation scheme is derived. Initially, the sum in (A.3) is decomposed into two parts

$$
S(\alpha) = \sum_{n=1}^{\infty} e^{in\alpha} f_n = R_M(\alpha) + Q_M(\alpha)\,, \tag{A.11}
$$

where

$$
Q_M(\alpha) = \sum_{n=1}^{\infty} e^{in\alpha} \sum_{m=1}^{M} c_m (1/n)^m\,, \tag{A.12}
$$

$$
R_M(\alpha) = \sum_{n=1}^{\infty} e^{in\alpha}\left(f_n - \sum_{m=1}^{M} c_m (1/n)^m \right), \tag{A.13}
$$

and $c_1, c_2, \ldots, c_M$ denote the constant coefficients coming out in a power series expansion

$$f_n = \sum_{m=1}^{\infty} c_m (1/n)^m \text{ as } n \to \infty ; \; c_0 = f_\infty = 0 . \tag{A.14}$$

If $c_0 \neq 0$, a final result for $S(\alpha)$ would involve impulse functions, which can be determined easily by an analytical approach, and that case is not considered here. Note that the function $R_M(\alpha)$ can be computed conveniently because; the expression in (A.13) is rapidly convergent. But, this is not the case for the function $Q_M(\alpha)$. The computation of $Q_M(\alpha)$ can be aided by defining an auxiliary function and establishing a recurrence relation

$$h_1(\alpha) = \sum_{n=1}^{\infty} \frac{1}{n} e^{in\alpha} ; \; h_m(\alpha) = \int_0^{\alpha} h_{m-1}(t) dt ; \; m \geq 2 . \tag{A.15}$$

After that, $Q_M(\alpha)$ is expressed as

$$Q_M(\alpha) = \sum_{m=1}^{M} c_m \sum_{n=1}^{\infty} e^{in\alpha} (1/n)^m = \sum_{m=1}^{M} c_m \left(i^{m-1} h_m(\alpha) + P_m(\alpha) \right), \tag{A.16}$$

where

$$P_m(\alpha) = \sum_{p=0}^{m-2} \frac{(i\alpha)^p}{p!} \zeta(m-p) , \tag{A.17}$$

are polynomials of degree m-2 and ζ denotes a zeta function defined as

$$\zeta(s) = \sum_{n=1}^{\infty} \frac{1}{n^s} ; \; \operatorname{Re} s > 1 , \tag{A.18}$$

whose values at the integers are tabulated in [24]. Also its values at the even integers can be expressed in terms of the Bernoulli numbers, which are considered in Appendix B.

The real and imaginary parts of $h_1(\alpha)$ can be written as [27 – Appendix A.6]

$$h_1(\alpha) = \frac{i}{2}(\pi \operatorname{sgn} \alpha - \alpha) - \frac{1}{2} \ln \alpha^2 + U_1(\alpha) ; \; 0 < |\alpha| < 2\pi , \tag{A.19}$$

where

$$U_1(\alpha) = -\ln\left(\frac{2\sin(\alpha/2)}{\alpha}\right);\ 0 < |\alpha| < 2\pi\,, \tag{A.20}$$

and the Taylor series expansion of $U_1(\alpha)$ is

$$U_1(\alpha) = \sum_{k=1}^{\infty} \frac{\zeta(2k)}{(2\pi)^{2k} k} \alpha^{2k}\ ;\ 0 < |\alpha| < 2\pi\,. \tag{A.21}$$

Substituting (A.21) into (A.19) and then carrying out the recurrence relation defined in (A.15) for each $h_m(\alpha)$, the expression in (A.16) is converted into a numerically convenient form and $S(\alpha)$ is written as

$$S(\alpha) = \sum_{n=1}^{\infty} e^{in\alpha} f_n = \sum_{n=1}^{\infty} e^{in\alpha}\left(f_n - \sum_{m=1}^{M} c_m (1/n)^m\right) + c_1 h_1(\alpha) +$$
$$\sum_{m=2}^{M} c_m \left\{ \frac{(i\alpha)^{m-1}}{(m-1)!}\left(i/2\left(\pi \operatorname{sgn}\alpha - \alpha/m\right) - 1/2 \ln \alpha^2 + H_{m-1}\right) + i^{m-1} U_m(\alpha) + P_m(\alpha) \right\}, \tag{A.22}$$

where $U_m(\alpha)$ denote rapidly convergent sums

$$U_m(\alpha) = \frac{\alpha^{m-1}}{(m-1)!} \sum_{k=1}^{\infty} \frac{\zeta(2k)}{(2\pi)^{2k} k} \frac{(2k)!(m-1)!}{(2k+m-1)!} \alpha^{2k}\ ;\ 0 < |\alpha| < 2\pi\,, \tag{A.23}$$

and H_m are known as harmonic numbers [24]

$$H_m = \sum_{p=1}^{m} \frac{1}{p}\,. \tag{A.24}$$

The constraint $0 < |\alpha| < 2\pi$ in the expressions is due to branch point singularities of the function $h_1(\alpha)$ at $\alpha = 0, \pm 2\pi, \pm 4\pi, \ldots$. But, the identities

$$S(\alpha + 2\pi) = S(\alpha) \text{ and/or } S(\pi + \alpha) = S(-\pi + \alpha)\,, \tag{A.25}$$

can be detected easily from (A.3) and so the computations can be restricted to the interval $-\pi < \alpha \le \pi$ by making an appropriate change of variable. In the case $\alpha = 0$, the series in (A.3) is divergent if $c_1 \ne 0$ else the expression for $S(\alpha)$ reduces to that given in [26],

$$S(0) = \sum_{n=1}^{\infty} f_n = \sum_{n=1}^{\infty}\left(f_n - \sum_{m=2}^{M} c_m (1/n)^m\right) + \sum_{m=2}^{M} c_m \zeta(m)\,. \tag{A.26}$$

Thus, a convenient computation scheme is obtained for the function $S(\alpha)$. The given method can also be found in [21].

When the Fourier sums are considered, the derived expressions may be used separately for the two sums in (A.10), which involve f_n and g_n. However, the whole procedure may yield much simpler expressions for some special cases of f_n and g_n. For example, if $g_n = f_{-n}$ the Kummer's acceleration method gives up an expression:

$$N(x) = {}^{a_0}\!/_2 + {}^{1}\!/_2 \sum_{\substack{n=-\infty \\ n\neq 0}}^{\infty} e^{inx}\left(f_n - \sum_{m=1}^{M} c_m \left({}^{1}\!/_n\right)^m \right) - {}^{1}\!/_2 \sum_{m=1}^{M} c_m \frac{(2\pi i)^m}{m!} B_m\left({}^{x}\!/_{2\pi}\right); 0 \le x \le 2\pi \text{ , (A.27)}$$

or as an alternative, one can let $M \to \infty$ and write

$$N(x) = {}^{a_0}\!/_2 - {}^{1}\!/_2 \sum_{m=1}^{\infty} c_m \frac{(2\pi i)^m}{m!} B_m\left({}^{x}\!/_{2\pi}\right);\ 0 \le x \le 2\pi \text{ ,} \tag{A.28}$$

where $B_m(x)$ denotes an *m-th* Bernoulli polynomial [24]. Here, the expressions are derived by establishing an identity

$$\sum_{\substack{n=-\infty \\ n\neq 0}}^{\infty} \frac{e^{inx}}{n^m} = -\frac{(2\pi i)^m}{m!} B_m\left({}^{x}\!/_{2\pi}\right);\ 0 \le x \le 2\pi \text{ ,} \tag{A.29}$$

from the properties of the Bernoulli polynomials, and then using within the Kummer's acceleration method.

Alternatively, linear transformation methods such as a Levin-type sequence transformation method [28] are applicable to more general sums and generally they result in closed form analytic expressions or asymptotic expansions, which are more useful than the expression (A.22) we derived. However they are a bit sophisticated and may require some knowledge about how to treat the functions in the transformed domain. Our technique has an advantage that: it is computationally oriented and does not require too much analytic effort.

To test the efficiency of the method, the sum in (A.4) is computed for some discrete values of x in the range $-3 \le \log_{10}(x/\pi) \le 0$ with $r = 0.5$. When (A.8) is expanded into inverse powers of *n,* the power series coefficients are

Table A.1 Comparison of the relative errors

$\log_{10}(x/\pi)$	I_{limit}	Relative error – direct summation	Relative error- M=10, $n_{\max}$=50, $k_{\max}$=10.
-3.0	6.649320131169	$1.51*10^{-4}$	$1.24*10^{-11}$
-2.5	5.498030977387	$1.81*10^{-5}$	$3.39*10^{-13}$
-2.0	4.346772357306	$2.33*10^{-6}$	$-4.09*10^{-16}$
-1.5	3.195819043024	$3.17*10^{-7}$	$-1.53*10^{-15}$
-1.0	2.047915630582	$4.95*10^{-8}$	$-1.30*10^{-15}$
-0.5	0.930196772259	$1.09*10^{-8}$	$1.79*10^{-15}$
0.0	0.083974656992	$1.21*10^{-8}$	$2.13*10^{-10}$

$$c_0 = c_1 = c_2 = 0;\ c_m = \tfrac{1}{2}(-r)^{m-3}(m-1)(m-2);\ m \ge 3. \qquad \text{(A.30)}$$

In the numerical validations double precision arithmetic is used and the results are given in Table A.1. To obtain the limiting values, I_{limit}, M is set to 10 and the infinite sums in our method are carried out until no digit change is observed. A relative error criteria defined as $(I_{\lim it} - I)/I_{\lim it}$ is introduced to compare I_{limit} values with the results that are obtained from the direct summations of the original series up to 10^4 terms. Also the last column of the table shows the relative errors resulting from truncations of the infinite sums in our method. When the summations of $R_M(x)$ are carried up to $n_{\max} = 50$ and those of $U_m(x)$ are carried up to $k_{\max} = 10$, with $M = 10$; the relative errors are seen to be extremely small implying that the convergence speeds of the infinite sums are very high. The results in that case are obtained by using only about 650 terms for each x value (a table of the zeta functions at the integers was available).

As the table shows, the relative error in our method increases as x increases. This is due to the truncations of the infinite sums in $U_m(x)$ but, the errors can be avoided by using more terms. For example, the relative error can be reduced significantly (reduces from $2.13*10^{-10}$ to $4.96*10^{-16}$ for $x = \pi$) by setting $k_{\max} = 15$.

According to the derived computation scheme, an infinite sum of the form (A.3) can be computed easily once the values of the zeta function at the integers are available from a table and the power series coefficients of f_n are determined at the beginning. Only difficulty may be in finding the power series coefficients. Alternatively, a linear transformation method could yield more useful expressions but, it would require some analytical effort. However the method given here is computationally oriented and does not involve too much effort.

APPENDIX B. BERNOULLI POLYNOMIALS AND BERNOULLI NUMBERS

In Appendix A, it is shown that some forms of the infinite sums are related with the Bernoulli polynomials. Here, we present those polynomials and give some useful identities. The generating function for the Bernoulli polynomials is given as

$$\frac{te^{xt}}{e^t - 1} = \sum_{n=0}^{\infty} B_n(x) \frac{t^n}{n!}, \tag{B.1}$$

where $B_n(x)$ denote a Bernoulli polynomial of degree n. A few of the Bernoulli polynomials are given as

$$B_0(x) = 1, \tag{B.2}$$

$$B_1(x) = -\tfrac{1}{2} + x, \tag{B.3}$$

$$B_2(x) = \tfrac{1}{6} - x + x^2, \tag{B.4}$$

$$B_3(x) = \tfrac{1}{2}x - \tfrac{3}{2}x^2 + x^3, \tag{B.5}$$

$$B_4(x) = -\tfrac{1}{30}x + x^2 - 2x^3 + x^4, \tag{B.6}$$

and the remaining polynomials, $B_5(x)$, $B_6(x)$, $B_7(x)$, . . . can be found in [24]. There are many interesting properties for these polynomials. Some of those are

$$B_n(mx) = m^{n-1} \sum_{k=0}^{m-1} B_n(x + \tfrac{k}{m}); \; m=1, 2, 3, \ldots \tag{B.7}$$

$$B_n(x+h) = \sum_{k=0}^{n} \frac{n!}{(n-k)!k!} B_k(x) h^{n-k} \; ; \; n=0, 1, 2, 3, \ldots \tag{B.8}$$

$$B_n(\tfrac{1}{2}) = -(1 - 2^{1-n}) B_n(0), \tag{B.9}$$

$$B_n(0) = (-1)^n B_n(1), \tag{B.10}$$

$$\int_0^1 B_n(t)B_m(t)dt = (-1)^{n-1}\frac{m!n!}{(m+n)!}B_{m+n}(0). \tag{B.11}$$

Also the following infinite sums are expressible in terms of the Bernoulli polynomials

$$\sum_{k=1}^{\infty}\frac{\sin 2k\pi x}{k^{2n-1}} = \frac{(-1)^n(2\pi)^{2n-1}}{(2n-1)!2}B_{2n-1}(x);\ n\text{=1, 2, 3, 4, . . ., } x\neq 0, \tag{B.12}$$

$$\sum_{k=1}^{\infty}\frac{\cos 2k\pi x}{k^{2n}} = \frac{(-1)^{n-1}(2\pi)^{2n}}{(2n)!2}B_{2n}(x);\ n\text{=1, 2, 3, 4, . . ., } x\neq 0. \tag{B.13}$$

The Bernoulli numbers are obtained from the special values of the Bernoulli polynomials [24].The Bernoulli numbers are denoted by B_n and are defined as

$$B_n = B_n(0). \tag{B.14}$$

There are many ways to determine the Bernoulli numbers [24]. One practical way is to use a recurrence relation. A recurrence relation for the Bernoulli numbers can be obtained from the identity in (B.8). Letting x=0 and h=1, we obtain a recurrence formula

$$B_n = (-1)^n\sum_{k=0}^{n}\binom{n}{k}B_k;\ n\text{=0, 1, 2, 3, . . .} \tag{B.15}$$

Once B_0 is known, the other Bernoulli numbers B_1, B_2, B_3, . . . can be determined easily by using the recurrence relation (B.15). A few of the Bernoulli numbers are B_0=1, $B_1 = \frac{-1}{2}$, $B_2 = \frac{1}{6}$, $B_3 = 0$, $B_4 = \frac{-1}{30}$. They satisfy the inequality

$$\frac{2(2n)!}{(2\pi)^{2n}} < |B_{2n}| < \frac{2(2n)!}{(2\pi)^{2n}}\frac{2^{2n-1}}{(2^{2n-1}-1)};\ n\text{=1, 2, 3, . . .} \tag{B.16}$$

The Bernoulli numbers are closely related with the values of the zeta functions ζ, which are defined and used in Appendix A. The relation between them is

$$\zeta(2n) = \frac{(-1)^{n-1}(2\pi)^{2n}}{2(2n)!}B_{2n}. \tag{B.17}$$

Once the Bernoulli numbers are computed from the recurrence relation (B.15) and tabulated, the convergence acceleration method discussed in the Appendix A becomes very efficient for numerical computations.

APPENDIX C. ASYMPTOTIC FORMS FOR THE EXPRESSIONS INVOLVING BESSEL FUNCTIONS

Formulations of the problems considered in Chapter 2, Chapter 3, and Chapter 4 all involve cylindrical functions that are called as the Bessel functions. In this appendix, we focus on the behaviors of those functions for the limiting values of their orders and arguments. Specifically, the asymptotic form of a matrix, which is obtained in Chapter 4 is determined.

Let $R_v(z)$ be a solution of the Bessel's differential equation

$$z^2 \frac{d^2 R_v(z)}{dz^2} + z\frac{dR_v(z)}{dz} + (z^2 - v^2)R_v(z) = 0\,, \tag{C.1}$$

where v denotes an integer that is called as the order of the Bessel function. The function $R_v(z)$ may be: a Bessel function of the first kind $J_v(z)$, a Bessel function of the second kind $Y_v(z)$, a Hankel function of the first kind $H_v^{(1)}(z)$, and a Hankel function of the second kind $H_v^{(2)}(z)$. Any two of these functions are linearly independent solutions of the Bessel's differential equation (C.1); so they are related to each other by the expressions

$$H_v^{(1)}(z) = J_v(z) + jY_v(z)\,, \tag{C.2}$$

$$H_v^{(2)}(z) = J_v(z) - jY_v(z)\,, \tag{C.3}$$

and wronskian relations of them are given by

$$J_v(z)Y_v'(z) - J_v'(z)Y_v(z) = \frac{2}{\pi z}\,, \tag{C.4}$$

$$H_v^{(1)}(z)H_v'^{(2)}(z) - H_v'^{(1)}(z)H_v^{(2)}(z) = \frac{-4j}{\pi z}\,, \tag{C.5}$$

$$J_v(z)H_v'^{(2)}(z) - J_v'(z)H_v^{(2)}(z) = \frac{-2j}{\pi z}\,. \tag{C.6}$$

Insight into the behavior of solutions to Bessel's differential equation can be gained by noting their asymptotic forms for the limiting values of their arguments. For large arguments (as $z \to \infty$), the asymptotic forms of the Bessel functions are given in terms of the sinusoidal or exponential functions [24]

$$J_v(z) \cong \sqrt{\frac{2}{\pi z}} \cos\left(z - \tfrac{1}{2} v\pi - \tfrac{1}{4}\pi\right) \text{ as } z \to \infty, \tag{C.7}$$

$$Y_v(z) \cong \sqrt{\frac{2}{\pi z}} \sin\left(z - \tfrac{1}{2} v\pi - \tfrac{1}{4}\pi\right) \text{ as } z \to \infty, \tag{C.8}$$

$$H_v^{(1)}(z) \cong \sqrt{\frac{2}{\pi z}} e^{j\left(z - \frac{1}{2} v\pi - \frac{1}{4}\pi\right)} \text{ as } z \to \infty, \tag{C.9}$$

$$H_v^{(2)}(z) \cong \sqrt{\frac{2}{\pi z}} e^{-j\left(z - \frac{1}{2} v\pi - \frac{1}{4}\pi\right)} \text{ as } z \to \infty. \tag{C.10}$$

It is obvious from these expressions that the functions $J_v(z)$ and $Y_v(z)$ exhibit oscillatory behavior, as do the sinusoidal functions. Hence, these solutions represent cylindrical standing waves. However, $H_v^{(1)}(z)$ and $H_v^{(2)}(z)$ represent traveling waves, as do the exponential functions. They therefore represent cylindrical traveling waves, $H_v^{(1)}(z)$ representing inward-traveling waves and $H_v^{(2)}(z)$ representing outward-traveling waves [22]. This direction of wave travel is as a consequence of the choice of $e^{j\omega t}$ time variation. If it was chosen $e^{-j\omega t}$, then the interpretations of $H_v^{(1)}(z)$ and $H_v^{(2)}(z)$ would be reversed. When the argument z tends to zero, the asymptotic forms of the Bessel functions are given as

$$J_v(z) \cong \frac{(\frac{1}{2} z)^v}{v!} \text{ as } z \to 0, \tag{C.11}$$

$$Y_v(z) \cong -jH_v^{(1)}(z) \cong jH_v^{(2)}(z) \cong -\frac{(v-1)!(\frac{1}{2} z)^{-v}}{\pi} \text{ ; } v \neq 0 \text{; as } z \to 0, \tag{C.12}$$

$$Y_0(z) \cong -jH_0^{(1)}(z) \cong jH_0^{(2)}(z) \cong \frac{2}{\pi} \ln z \text{ as } z \to 0. \tag{C.13}$$

On the other hand if the order of a Bessel function tends to infinity, the function decays or grows exponentially as illustrated in the following equations. It is supposed that $v \to \infty$ and the argument z is fixed. The asymptotic forms in that case are [24]

$$J_v(z) \cong \frac{1}{\sqrt{2\pi v}}\left(\frac{2v}{ez}\right)^{-v} \text{ as } v\to\infty, \tag{C.14}$$

$$Y_v(z) \cong -\sqrt{\frac{2}{\pi v}}\left(\frac{2v}{ez}\right)^{v} \text{ as } v\to\infty, \tag{C.15}$$

$$H_v^{(1)}(z) \cong -j\sqrt{\frac{2}{\pi v}}\left(\frac{2v}{ez}\right)^{v} \text{ as } v\to\infty, \tag{C.16}$$

$$H_v^{(2)}(z) \cong j\sqrt{\frac{2}{\pi v}}\left(\frac{2v}{ez}\right)^{v} \text{ as } v\to\infty. \tag{C.17}$$

When the argument of a Bessel function is imaginary ($z=-j\alpha$), it is conventional to use the modified Bessel functions. The modified Bessel functions are related to the regular Bessel functions by [24]

$$J_v(-j\alpha) = e^{-jv\pi/2} I_v(\alpha), \tag{C.18}$$

$$Y_v(-j\alpha) = -je^{-jv\pi/2} I_v(\alpha) - \frac{2}{\pi} e^{jv\pi/2} K_v(\alpha), \tag{C.19}$$

$$H_v^{(1)}(-j\alpha) = J_v(-j\alpha) + jY_v(-j\alpha) = 2e^{-jv\pi/2} I_v(\alpha) - \frac{2j}{\pi} e^{jv\pi/2} K_v(\alpha), \tag{C.20}$$

$$H_v^{(2)}(-j\alpha) = J_v(-j\alpha) - jY_v(-j\alpha) = \frac{2j}{\pi} e^{jv\pi/2} K_v(\alpha), \tag{C.21}$$

where I_v and K_v are known as modified Bessel functions of the first kind and the second kind, respectively. Asymptotic formulas for the large arguments of the modified Bessel functions are [24]

$$I_v(\alpha) \cong \frac{e^{\alpha}}{\sqrt{2\pi\alpha}} \text{ as } \alpha\to\infty, \tag{C.22}$$

$$K_v(\alpha) \cong \sqrt{\frac{\pi}{2\alpha}} e^{-\alpha} \text{ as } \alpha\to\infty. \tag{C.23}$$

These expressions illustrate the evanescent character of the modified Bessel functions. It is apparent that the modified Bessel functions are used to represent evanescent-type waves. When the argument α tends to zero, the asymptotic forms of the modified Bessel functions are given as

$$I_v(\alpha) \cong \frac{(\frac{1}{2}\alpha)^v}{v!} \text{ as } \alpha \to 0, \tag{C.24}$$

$$K_v(z) \cong \tfrac{1}{2}(v-1)!(\tfrac{1}{2}\alpha)^{-v} \text{ ; } v \neq 0 \text{; as } \alpha \to 0, \tag{C.25}$$

$$K_0(\alpha) \cong -\ln\alpha \text{ as } \alpha \to 0. \tag{C.26}$$

If the argument α is fixed but the order tends to infinity ($v \to \infty$), the corresponding asymptotic forms are

$$I_v(\alpha) \cong \frac{1}{\sqrt{2\pi v}}\left(\frac{2v}{e\alpha}\right)^{-v} \text{ as } v \to \infty, \tag{C.27}$$

$$K_v(\alpha) \cong \sqrt{\frac{\pi}{2v}}\left(\frac{2v}{e\alpha}\right)^{v} \text{ as } v \to \infty. \tag{C.28}$$

In Chapter 4, an integral equation is obtained for a cylindrical dielectric shell covered periodically with conducting patches. The integral equation is given in terms of a 2x2 matrix, whose entries involve various kinds of Bessel functions. Here, an asymptotic form of the matrix is determined by using large order asymptotic forms for the Bessel functions appearing in it. The asymptotic form obtained in this appendix is used in a convergence acceleration technique, which is described in Chapter 4. The matrix is given by the expressions

$$Z_Q = \left\{ Y_{0mn} - h_{0mn}(\rho_0)[e_{0mn}(\rho_0)]^{-1} \right\}^{-1}, \tag{C.29}$$

where

$$Y_{0mn} = \left\{ h^{-}_{1mn}(\rho_0)[e^{-}_{1mn}(\rho_0)]^{-1} + h^{+}_{1mn}(\rho_0)[e^{+}_{1mn}(\rho_0)]^{-1}\zeta_{0mn} \right\} \left\{ I + \zeta_{0mn} \right\}^{-1}, \tag{C.30}$$

$$\zeta_{0mn} = e^{+}_{1mn}(\rho_0)[e^{+}_{1mn}(\rho_1)]^{-1}\zeta_{1mn} e^{-}_{1mn}(\rho_1)[e^{-}_{1mn}(\rho_0)]^{-1}, \tag{C.31}$$

$$\zeta_{1mn} = \left\{ h^{+}_{1mn}(\rho_1)[e^{+}_{1mn}(\rho_1)]^{-1} - h_{2mn}(\rho_1)[e_{2mn}(\rho_1)]^{-1} \right\}^{-1} \\ \left\{ h_{2mn}(\rho_1)[e_{2mn}(\rho_1)]^{-1} - h^{-}_{1mn}(\rho_1)[e^{-}_{1mn}(\rho_1)]^{-1} \right\}, \tag{C.32}$$

e and *h* are as given in (4.30)-(4.37). It can easily be shown that if the dielectric shell were not present, Z_Q would simplify to an expression given in [10] and here we denote it as Z_{Q_0}

$$Z_{Q_0} = \frac{1}{j\omega\varepsilon_0}\frac{j\pi}{2} J_{v_m}(\kappa_{0n}\rho_0) H^{(2)}_{v_m}(\kappa_{0n}\rho_0)$$

$$\begin{bmatrix} -k_0^2\rho_0 \dfrac{J'_{v_m}(\kappa_{0n}\rho_0) H'^{(2)}_{v_m}(\kappa_{0n}\rho_0)}{J_{v_m}(\kappa_{0n}\rho_0) H^{(2)}_{v_m}(\kappa_{0n}\rho_0)} - \dfrac{1}{\rho_0}\left(\dfrac{v_m\beta_n}{\kappa_{0n}}\right)^2 & v_m\beta_n \\ v_m\beta_n & -\kappa_{0n}^2\rho_0 \end{bmatrix}. \quad \text{(C.33)}$$

After that, we show that Z_Q and Z_{Q_0} both have the same asymptotic form as $v_m \to \infty$. The proof starts by considering the large order asymptotic values of Bessel functions. The order of Bessel functions appearing in the matrices are given by

$$v_m = v_0 + 2\pi m / T_\phi . \quad \text{(C.34)}$$

If v_m tends to infinity, the asymptotic forms of the Bessel functions and their derivatives are given by [24]

$$J_{v_m}(\kappa_{in}\rho) \cong \frac{1}{\sqrt{2\pi v_m}}\left(\frac{2v_m}{e\kappa_{in}\rho}\right)^{-v_m} \quad \text{as } v_m \to \infty , \quad \text{(C.35)}$$

$$J'_{v_m}(\kappa_{in}\rho) \cong \frac{e}{2\sqrt{2\pi v_m}}\left(\frac{2v_m}{e\kappa_{in}\rho}\right)^{-v_m+1} \quad \text{as } v_m \to \infty , \quad \text{(C.36)}$$

$$Y_{v_m}(\kappa_{in}\rho) \cong -\sqrt{\frac{2}{\pi v_m}}\left(\frac{2v_m}{e\kappa_{in}\rho}\right)^{v_m} \quad \text{as } v_m \to \infty , \quad \text{(C.37)}$$

$$Y'_{v_m}(\kappa_{in}\rho) \cong \frac{e}{2}\sqrt{\frac{2}{\pi v_m}}\left(\frac{2v_m}{e\kappa_{in}\rho}\right)^{v_m+1} \quad \text{as } v_m \to \infty , \quad \text{(C.38)}$$

$$H^{(2)}_{v_m}(\kappa_{in}\rho) \cong j\sqrt{\frac{2}{\pi v_m}}\left(\frac{2v_m}{e\kappa_{in}\rho}\right)^{v_m} \quad \text{as } v_m \to \infty , \quad \text{(C.39)}$$

$$H'^{(2)}_{v_m}(\kappa_{in}\rho) \cong -j\frac{e}{2}\sqrt{\frac{2}{\pi v_m}}\left(\frac{2v_m}{e\kappa_{in}\rho}\right)^{v_m+1} \quad \text{as } v_m \to \infty . \quad \text{(C.40)}$$

By using these expressions, the asymptotic forms of the matrices $e_{imn}(\rho)$ appearing in (C.29)-, (C.32) for different regions are obtained as

$$e_{2mn}(\rho) \cong \frac{1}{j\omega\varepsilon_0\rho}\frac{1}{\sqrt{2\pi v_m}}\left(\frac{2v_m}{e\kappa_{0n}\rho}\right)^{-v_m}\begin{bmatrix} -v_m\beta_n & j\omega\varepsilon_0 v_m \\ \kappa_{0n}^2\rho & 0 \end{bmatrix} \text{ as } v_m \to \infty , \quad \text{(C.41)}$$

$$e_{1mn}^{-}(\rho) \cong \frac{1}{j\omega\varepsilon_1\rho}\frac{1}{\sqrt{2\pi v_m}}\left(\frac{2v_m}{e\kappa_{1n}\rho}\right)^{-v_m}\begin{bmatrix} -v_m\beta_n & j\omega\varepsilon_1 v_m \\ \kappa_{1n}^2\rho & 0 \end{bmatrix} \text{ as } v_m \to \infty, \quad \text{(C.42)}$$

$$e_{1mn}^{+}(\rho) \cong \frac{-1}{j\omega\varepsilon_1\rho}\sqrt{\frac{2}{\pi v_m}}\left(\frac{2v_m}{e\kappa_{1n}\rho}\right)^{v_m}\begin{bmatrix} -v_m\beta_n & -j\omega\varepsilon_1 v_m \\ \kappa_{1n}^2\rho & 0 \end{bmatrix} \text{ as } v_m \to \infty, \quad \text{(C.43)}$$

$$e_{0mn}(\rho) \cong \frac{j}{j\omega\varepsilon_0\rho}\sqrt{\frac{2}{\pi v_m}}\left(\frac{2v_m}{e\kappa_{0n}\rho}\right)^{v_m}\begin{bmatrix} -v_m\beta_n & -j\omega\varepsilon_0 v_m \\ \kappa_{0n}^2\rho & 0 \end{bmatrix} \text{ as } v_m \to \infty. \quad \text{(C.44)}$$

Similarly, the asymptotic forms of the matrices $h_{imn}(\rho)$ for different regions are obtained as

$$h_{2mn}(\rho) \cong \frac{1}{j\omega\mu_0\rho}\frac{1}{\sqrt{2\pi v_m}}\left(\frac{2v_m}{e\kappa_{0n}\rho}\right)^{-v_m}\begin{bmatrix} 0 & \kappa_{0n}^2\rho \\ j\omega\mu_0 v_m & v_m\beta_n \end{bmatrix} \text{ as } v_m \to \infty, \quad \text{(C.45)}$$

$$h_{1mn}^{-}(\rho) \cong \frac{1}{j\omega\mu_0\rho}\frac{1}{\sqrt{2\pi v_m}}\left(\frac{2v_m}{e\kappa_{1n}\rho}\right)^{-v_m}\begin{bmatrix} 0 & \kappa_{1n}^2\rho \\ j\omega\mu_0 v_m & v_m\beta_n \end{bmatrix} \text{ as } v_m \to \infty, \quad \text{(C.46)}$$

$$h_{1mn}^{-}(\rho) \cong \frac{-1}{j\omega\mu_0\rho}\sqrt{\frac{2}{\pi v_m}}\left(\frac{2v_m}{e\kappa_{1n}\rho}\right)^{v_m}\begin{bmatrix} 0 & \kappa_{1n}^2\rho \\ -j\omega\mu_0 v_m & v_m\beta_n \end{bmatrix} \text{ as } v_m \to \infty, \quad \text{(C.47)}$$

$$h_{0mn}(\rho) \cong \frac{j}{j\omega\mu_0\rho}\sqrt{\frac{2}{\pi v_m}}\left(\frac{2v_m}{e\kappa_{0n}\rho}\right)^{v_m}\begin{bmatrix} 0 & \kappa_{0n}^2\rho \\ -j\omega\mu_0 v_m & v_m\beta_n \end{bmatrix} \text{ as } v_m \to \infty. \quad \text{(C.48)}$$

Then the products $h_{imn}(\rho)[e_{imn}(\rho)]^{-1}$ of the matrices become

$$h_{2mn}(\rho)[e_{2mn}(\rho)]^{-1} \cong \frac{1}{j\omega\mu_0 v_m}\begin{bmatrix} \kappa_{0n}^2\rho & v_m\beta_n \\ v_m\beta_n & \dfrac{-v_m^2}{\rho} \end{bmatrix} \text{ as } v_m \to \infty, \quad \text{(C.49)}$$

$$h_{1mn}^{-}(\rho)[e_{1mn}^{-}(\rho)]^{-1} \cong \frac{1}{j\omega\mu_0 v_m}\begin{bmatrix} \kappa_{1n}^2\rho & v_m\beta_n \\ v_m\beta_n & \dfrac{-v_m^2}{\rho} \end{bmatrix} \text{ as } v_m \to \infty, \quad \text{(C.50)}$$

$$h_{1mn}^{+}(\rho)[e_{1mn}^{+}(\rho)]^{-1} \cong \frac{-1}{j\omega\mu_0 v_m}\begin{bmatrix} \kappa_{1n}^2\rho & v_m\beta_n \\ v_m\beta_n & \dfrac{-v_m^2}{\rho} \end{bmatrix} \cong -h_{1mn}^{-}(\rho)[e_{1mn}^{-}(\rho)]^{-1} \text{ as } v_m \to \infty, \quad \text{(C.51)}$$

$$h_{0mn}(\rho)[e_{0mn}(\rho)]^{-1} \cong \frac{-1}{j\omega\mu_0 v_m}\begin{bmatrix} \kappa_{0n}^2\rho & v_m\beta_n \\ v_m\beta_n & \dfrac{-v_m^2}{\rho} \end{bmatrix} \text{ as } v_m \to \infty . \tag{C.52}$$

By using the asymptotic forms given above, the matrix ζ_{1mn} in (C.32) is determined as follows:

$$\begin{aligned}
\zeta_{1mn} &= \left\{ h_{1mn}^{+}(\rho_1)[e_{1mn}^{+}(\rho_1)]^{-1} - h_{2mn}(\rho_1)[e_{2mn}(\rho_1)]^{-1} \right\}^{-1} \\
&\qquad \left\{ h_{2mn}(\rho_1)[e_{2mn}(\rho_1)]^{-1} - h_{1mn}^{-}(\rho_1)[e_{1mn}^{-}(\rho_1)]^{-1} \right\} \\
&= -\left\{ I - 2\left\{ I + \left\{ h_{1mn}^{-}(\rho_1)[e_{1mn}^{-}(\rho_1)]^{-1} \right\}^{-1} h_{2mn}(\rho_1)[e_{2mn}(\rho_1)]^{-1} \right\}^{-1} \right\} \\
&\cong -\left\{ I - 2\left\{ I + \begin{bmatrix} \dfrac{k_0^2}{k_1^2} & 0 \\ \left(k_0^2 - k_1^2\right)\dfrac{\beta_n\rho_1}{v_m k_1^2} & 1 \end{bmatrix} \right\}^{-1} \right\} \\
&\cong \frac{\left(k_1^2 - k_0^2\right)}{\left(k_1^2 + k_0^2\right)} \begin{bmatrix} 1 & 0 \\ \dfrac{\beta_n\rho_1}{v_m} & 0 \end{bmatrix} \text{ as } v_m \to \infty .
\end{aligned} \tag{C.53}$$

For substituting into the matrix ζ_{0mn} in (C.31), we establish the following asymptotic expressions

$$e_{1mn}^{+}(\rho_0)[e_{1mn}^{+}(\rho_1)]^{-1} \cong \left(\frac{\rho_1}{\rho_0}\right)^{v_m} \begin{bmatrix} \dfrac{\rho_1}{\rho_0} & 0 \\ 0 & 1 \end{bmatrix} \text{ as } v_m \to \infty , \tag{C.54}$$

$$e_{1mn}^{-}(\rho_1)[e_{1mn}^{-}(\rho_0)]^{-1} \cong \left(\frac{\rho_0}{\rho_1}\right)^{v_m} \begin{bmatrix} \dfrac{\rho_0}{\rho_1} & 0 \\ 0 & 1 \end{bmatrix} \text{ as } v_m \to \infty , \tag{C.55}$$

and proceed as:

$$\begin{aligned}
\zeta_{0mn} &= e_{1mn}^{+}(\rho_0)[e_{1mn}^{+}(\rho_1)]^{-1} \zeta_{1mn} e_{1mn}^{-}(\rho_1)[e_{1mn}^{-}(\rho_0)]^{-1} \\
&\cong \left(\frac{\rho_1}{\rho_0}\right)^{v_m} \begin{bmatrix} \dfrac{\rho_1}{\rho_0} & 0 \\ 0 & 1 \end{bmatrix} \frac{\left(k_1^2 - k_0^2\right)}{\left(k_1^2 + k_0^2\right)} \begin{bmatrix} 1 & 0 \\ \dfrac{\beta_n\rho_1}{v_m} & 0 \end{bmatrix} \left(\frac{\rho_0}{\rho_1}\right)^{v_m} \begin{bmatrix} \dfrac{\rho_0}{\rho_1} & 0 \\ 0 & 1 \end{bmatrix} \\
&\cong \frac{\left(k_1^2 - k_0^2\right)}{\left(k_1^2 + k_0^2\right)} \begin{bmatrix} 1 & 0 \\ \dfrac{\beta_n\rho_0}{v_m} & 0 \end{bmatrix} \text{ as } v_m \to \infty .
\end{aligned} \tag{C.56}$$

Subsequently, Y_{0mn} is determined from

$$\begin{aligned} Y_{0mn} &= \left\{ h_{1mn}^{-}(\rho_0)[e_{1mn}^{-}(\rho_0)]^{-1} + h_{1mn}^{+}(\rho_0)[e_{1mn}^{+}(\rho_0)]^{-1}\zeta_{0mn} \right\} \left\{ I + \zeta_{0mn} \right\}^{-1} \\ &\cong h_{1mn}^{-}(\rho_0)[e_{1mn}^{-}(\rho_0)]^{-1} \left\{ I - 2\zeta_{0mn} \left\{ I + \zeta_{0mn} \right\}^{-1} \right\} \\ &\cong \frac{1}{j\omega\mu_0 v_m} \begin{bmatrix} \kappa_{0n}^2 \rho_0 & v_m \beta_n \\ v_m \beta_n & \dfrac{-v_m^2}{\rho_0} \end{bmatrix} \text{ as } v_m \to \infty . \end{aligned} \tag{C.57}$$

Finally, the asymptotic value of the impedance matrix is obtained as

$$Z_Q = \left\{ Y_{0mn} - h_{0mn}(\rho_0)[e_{0mn}(\rho_0)]^{-1} \right\}^{-1} \cong Z_{Q_a} \text{ as } v_m \to \infty , \tag{C.58}$$

where

$$\begin{aligned} Z_{Q_a} &\cong \left\{ \frac{1}{j\omega\mu_0 v_m} \begin{bmatrix} \kappa_{0n}^2 \rho_0 & v_m \beta_n \\ v_m \beta_n & \dfrac{-v_m^2}{\rho_0} \end{bmatrix} - \frac{-1}{j\omega\mu_0 v_m} \begin{bmatrix} \kappa_{0n}^2 \rho_0 & v_m \beta_n \\ v_m \beta_n & \dfrac{-v_m^2}{\rho_0} \end{bmatrix} \right\}^{-1} \\ &\cong \frac{j\omega\mu_0}{2k_0^2 v_m} \begin{bmatrix} \dfrac{v_m^2}{\rho_0} & v_m \beta_n \\ v_m \beta_n & -\kappa_{0n}^2 \rho_0 \end{bmatrix} \text{ as } v_m \to \infty . \end{aligned} \tag{C.59}$$

Next, it will be shown that the asymptotic form of the matrix Z_{Q_0} in (C.33) equals Z_{Q_a} as $v_m \to \infty$. This is proved by obtaining asymptotic expressions for the products Bessel functions,

$$J_{v_m}(\kappa_{0n}\rho) H_{v_m}^{(2)}(\kappa_{0n}\rho) \cong \frac{j}{\pi v_m} \text{ as } v_m \to \infty , \tag{C.60}$$

$$J'_{v_m}(\kappa_{0n}\rho) H'^{(2)}_{v_m}(\kappa_{0n}\rho) \cong \frac{-j v_m}{\pi \left(\kappa_{0n}\rho \right)^2} \; v_m \to \infty . \tag{C.61}$$

Then substituting into (C.33), we obtain

$$Z_{Q_0} \cong \frac{j\omega\mu_0}{2k_0^2 v_m} \begin{bmatrix} \dfrac{v_m^2}{\rho_0} & v_m \beta_n \\ v_m \beta_n & -\kappa_{0n}^2 \rho_0 \end{bmatrix} = Z_{Q_a} \text{ as} \, v_m \to \infty . \tag{C.62}$$

When $v_m \to -\infty$, one can use identities [24]

$$J_{-v}(z) = (-1)^v J_v(z)\,, \tag{C.63}$$

$$Y_{-v}(z) = (-1)^v Y_v(z)\,, \tag{C.64}$$

$$H_{-v}^{(2)}(z) = (-1)^v H_v^{(2)}(z)\,, \tag{C.65}$$

and subsequently show that

$$Z_Q \cong Z_{Q_a} \text{ as } v_m \to -\infty\,, \tag{C.66}$$

$$Z_{Q_0} \cong Z_{Q_a} \text{ as } v_m \to -\infty\,, \tag{C.67}$$

where

$$Z_{Q_a} \cong \frac{-j\omega\mu_0}{2k_0^2 v_m}\begin{bmatrix} \dfrac{v_m^2}{\rho_0} & v_m\beta_n \\ v_m\beta_n & -\kappa_{0n}^2\rho_0 \end{bmatrix} \text{as}\, v_m \to -\infty\,. \tag{C.68}$$

Hence, the proof is completed and it is shown that both Z_Q and Z_{Q_0} have the same asymptotic form

$$Z_Q \cong Z_{Q_a} \text{ as } v_m \to \pm\infty\,, \tag{C.69}$$

$$Z_{Q_0} \cong Z_{Q_a} \text{ as } v_m \to \pm\infty\,, \tag{C.70}$$

where

$$Z_{Q_a} \cong \frac{j\omega\mu_0}{2k_0^2\,|\,v_m\,|}\begin{bmatrix} \dfrac{v_m^2}{\rho_0} & v_m\beta_n \\ v_m\beta_n & -\kappa_{0n}^2\rho_0 \end{bmatrix} \text{as}\, v_m \to \pm\infty\,. \tag{C.71}$$

APPENDIX D. RELATED PUBLICATIONS OF THE AUTHOR

Journal Papers:

1. Ali Uzer and Tuncay Ege. (2003). An improved convergence acceleration method for the strip grating cylindrical surface problem. *Electrical Engineering*, vol **86**, pp. 55-60.

2. Ali Uzer and Tuncay Ege. (2004). Radiation from a current filament located inside a cylindrical frequency selective surface. *ETRI Journal*, vol. **26**, pp. 481-485.

3. Ali Uzer and Tuncay Ege. (2004). Scattering from periodically spaced longitudinal slots on a conducting cylinder. *Electrical Engineering*, (Accepted for publication).

4. Ali Uzer and Tuncay Ege. (2005). On the convergence acceleration of slowly convergent infinite sums involving oscillating terms. *Computing*, (Accepted for publication).

5. Ali Uzer and Tuncay Ege. (2005). Scattering from a dielectric cylindrical shell periodically loaded with metallic patches. *Electronics Letters*, (Accepted for publication).

REFERENCES

[1] Chi. Hou. Chan, and R. Mittra, (1990). On the analysis of frequency selective surfaces using subdomain basis functions, *IEEE Transactions on Antennas and Propagation*, **38**, pp. 40-50.

[2] R. Mittra, C. H. Chan, T. Cwik. (1988). Techniques for analyzing frequency selective surfaces – A review. *Proceedings of IEEE*, **76**, pp. 1593-1614.

[3] H.H. Ohta, K.C. Lang, C.H. Tsao and R. Mittra. (1982). Frequency selective surface for satellite communications antenna applications, *IEEE AP Symposium Digest*, pp. 475-478.

[4] R. B. Keiburtz, and A. Ishimaru. (1961). Scattering by a periodically apertured conducting screen. *IEEE Transactions on Antennas and Propagation*, vol. **AP-3**, pp. 506-544.

[5] R. H. Ott., R. G. Kouyoumjian, and Peters. (1967). Scattering by a two dimensional periodic array of narrow plates, *Radio. Sci.*, **2**, pp. 1317-1349.

[6] C. C. Chen. (1970). Scattering by a two dimensional periodic array of conducting plates. *IEEE Transactions on Antennas and Propagation*, vol. **AP-18**, pp. 660-665.

[7] J. P. Montgomery. (1975). Scattering by an infinite periodic array of thin conductors on a dielectric sheet. *IEEE Transactions on Antennas and Propagation*, vol. **AP-23**, pp. 70-75.

[8] C. H. Taso, R. Mittra. (1982). A spectral-iteration approach for analyzing scattering from FSS's. *IEEE Transactions on Antennas and Propagation*, vol. **AP-30**, pp 303-308.

[9] J. C. Herper, A. Hessel, and B. Tomasic. (1985). Element pattern of an axial dipole in a cylindrical phased array- Theory and Experiment. *IEEE Transactions on Antennas and Propagation*, vol. **AP-33**, pp. 259-272.

[10] Tom Cwik. (1990). Coupling into and scattering from cylindrical structures covered periodically with metallic patches. *IEEE Transactions on Antennas and Propagation*, vol. **AP-38**, pp. 220-226.

[11] G. Loukos and J. C. Vardaxoglou. (1995). Propagation inside strip grating FSS waveguides with cylindrical cross-section, *Electronic Letters,* Vol. **31**, pp. 778-779.

[12] G. Loukos and J. C. Vardaxoglou, and R. Seager. (1997). Cylindrical frequency selective surfaces of transverse and longitudinal dipole elements.

Tenth International Conference on Antennas and Propagation, vol. **1**, pp. 1.170-1.173.

[13] M. Mokhtar. (1998). Analysis of cylindrical frequency selective surfaces. *Proceedings of the Fifteenth National Radio Science Conference*, Cat. No.98EX109, pp. B.8.1-B.8.8.

[14] J. M. Sajer, E. Michielssen, and R. Mittra. (1993). Electromagnetic scattering from periodic arrays on a multilayered cylindrical surface. *Antennas and Propagation Society International Symposium*, AP-S. Digest*.,* vol. **3**, pp. 1940-1943.

[15] A. Freni. (1996). Plane wave scattering from a cylinder loaded periodically with groups of metallic rings. *Electronic Letters,* Vol. **32**, pp. 874-875.

[16] Ahmed A. Kishk and Per-Simon Kildal. (1997). Asymptotic boundary conditions for strip-loaded scatterers applied to circular dielectric cylinders under oblique incidence. *IEEE Transactions on Antennas and Propagation*, Vol. **45**, pp. 51-56.

[17] Ali Uzer. (1998). A cylindrical frequency selective surface comprising of metal strips. *M.Sc. thesis*, University of Gaziantep.

[18] Ali Uzer and Tuncay Ege. (2003). An improved convergence acceleration method for the strip grating cylindrical surface problem. *Electrical Engineering*, vol **86**, pp. 55-60.

[19] Ali Uzer and Tuncay Ege. (2004). Radiation from a current filament located inside a cylindrical frequency selective surface. *ETRI Journal*, vol. **26**, pp. 481-485.

[20] Ali Uzer and Tuncay Ege. (2004). Scattering from periodically spaced longitudinal slots on a conducting cylinder. *Electrical Engineering*, (Accepted for publication).

[21] Ali Uzer and Tuncay Ege. (2005). On the convergence acceleration of slowly convergent infinite sums involving oscillating terms. *Computing*, (Accepted for publication).

[22] Roger F. Harrington. (1961). *Time Harmonic Electromagnetic Fields*. New York, McGraw Hill Inc.

[23] C. A. Balanis. (1989). *Advanced Engineering Electromagnetics*. New York, Wiley.

[24] Milton Abramowitz, and Irena A. Stegun. (1965). *Handbook of Mathematical Functions*. New York, Dover.

[25] Roger F. Harrington. (1968). *Field Computation by Moment Methods*. New York, Macmillian.

[26] P. Flajolet and I. Vardi. (1996). Zeta Function Expansions of Classical Constants. *Unpublished memo, available online http://pauillac.inria.fr/algo/flajolet/Publications*.

[27] R.E. Collin. (1991), *Field Theory of Guided Waves*. IEEE Press, New York, IEEE Press.

[28] H.H.H. Homeier. (2000). Scalar Levin-Type Sequence Transformations. *Journal of Computational and Applied Mathematics*. **122**, pp. 81-147.

VITA

Ali Uzer was born in İslahiye, Turkey in 1973. He received B.S. and M.Sc. degrees in Electrical and Electronics Engineering from University of Gaziantep in 1995 and 1998, respectively. His research area includes numerical analysis of the frequency selective surfaces and the scattering from cylindrical structures.